

Abstract

Superinductance

Vladimir Eduardovich Manucharyan

2012

We harness the phenomenon of kinetic inductance of a superconductor for the purposes of quantum information processing with superconducting circuits. In this work, the kinetic inductance of an array of Josephson tunnel junctions with carefully chosen parameters exceeds its geometric (magnetic) inductance by four orders of magnitude. Such an inductance can be used to construct electrical circuits in which quantum electrodynamics of charges and fluxes is governed by an effective fine structure constant over a unity. We refer to such fundamentally special quantum circuit element as superinductance.

To test the Josephson array superinductance, it is made a key element of a novel superconducting artificial atom, dubbed fluxonium. Fluxonium consists of the array in question shunting a small-capacitance Josephson tunnel junction. The atom is tuned by a magnetic flux piercing the junction loop and is addressed by coupling the small junction capacitively to an on-chip microwave cavity. With an adequate choice of junction parameters, the low energy spectrum of fluxonium is quite unique: it almost corresponds to the inductive energy of the array charged with an integer number of flux quanta. Analysis of frequency-domain spectroscopy experiment, involving several lowest fluxonium transitions, establishes that the junction array indeed behaves as a linear inductance of quoted magnitude for a range of frequencies exceeding 10 GHz. Time-domain experiment yields the energy relaxation quality factor exceeding 10^5 . Frequency dependence of this quality factor suggests that it is likely limited by the losses in other circuit components. Finally, flux-dependence of the dephasing time of fluxonium transitions is inconsistent with either flux or critical current noise, but matches, without adjustable parameters, to our theory of the effect of coherent quantum phase-slip across the array, under the assumption of fluctuating parity of array islands. We conclude, that the phase-slip across the array limits the lower operating frequency of our superinductance to a quantity less than 1 MHz; it can be further reduced by several orders of magnitude by a modest adjustment of junction parameters.

Superinductance

A Dissertation
presented to the Faculty of the Graduate School
of
Yale University
in Candidacy for the Degree
of
Doctor of Philosophy

by

Vladimir Eduardovich Manucharyan

Dissertation director: Professor Michel H. Devoret

May 2012

Contents

Acknowledgements	8
List of Figures	12
List of Tables	12
List of Symbols	12
1 Introduction	16
1.1 Linear quantum fluctuations in electrical circuits	18
1.1.1 Fundamental asymmetry between charge and flux	18
1.1.2 Kinetic inductance	22
1.1.3 Superinductance with Josephson junction array	24
1.2 Quantum phase-slip	27
1.2.1 “Microscopic” lagrangian and stationary states	30
1.2.2 Emergent quantum phase-slip hamiltonian	33
1.2.3 Offset charges and Aharonov-Casher interference	36
1.2.4 Coherence of the quantum phase-slip process	40
1.2.5 Energy dissipation	41
1.3 Testing superinductance with fluxonium	43
1.3.1 Overview of main results	49
2 Experimental techniques	54
2.1 Nanofabrication	54

2.2	Microwave readout by reflectometry	58
2.2.1	Reflection amplitude	58
2.2.2	Low temperature setup	61
2.2.3	Room temperature setup	62
2.3	Sample holder	65
3	Fluxonium: concepts	69
3.1	Spectrum	69
3.1.1	Fluxons and plasmons	69
3.1.2	Matrix elements	74
3.1.3	The fluxonium qubit regime	78
3.2	Readout	79
3.2.1	Dispersive shifts by an arbitrary atom	81
3.2.2	Common examples	84
3.2.3	Dispersive shifts by fluxonium circuit	87
3.2.4	Spurious resonances	92
3.3	Decoherence	94
3.3.1	Spontaneous emission	94
3.3.2	Emission into measurement apparatus	97
3.3.3	Intrinsic dissipation and the garland effect	98
3.3.4	Dephasing: common mechanisms	99
3.3.5	Dephasing: Aharonov-Casher broadening	103
4	Fluxonium: a case study	106
4.1	Control experiments	106
4.1.1	Ground state	106
4.1.2	Fluxon-photon vacuum Rabi resonance	107
4.1.3	AC-Stark effect	110
4.1.4	Power broadening	113
4.2	Spectroscopy	113
4.2.1	Single phase-slip splitting near $\varphi_{\text{ext}} = \pi$	114

4.2.2	Double phase-slip splitting and plasmon near $\varphi_{\text{ext}} = 0$	115
4.2.3	The $e \leftrightarrow f$ vacuum Rabi resonance and side-band transitions	116
4.2.4	Experiment vs. theory	118
4.2.5	High power spectroscopy and spurious modes	118
4.3	Time-domain decoherence measurement	123
4.3.1	Energy relaxation: fluxonium as a quantum spectrum analyzer	125
4.3.2	Energy relaxation sweet-spot	127
4.3.3	Dephasing	128
4.4	Bonus track	130
4.4.1	Optical pumping and population inversion	130
4.4.2	Raman excitation of forbidden fluxonium transition	131
4.4.3	Suppression of qubit life-time by the readout photons	133
5	Conclusions and perspectives	134
5.1	Availability of superinductance	134
5.2	Offset-charge free quantum Josephson networks?	135
5.3	Processing quantum information with fluxonium qubits	137
5.3.1	QND state monitoring	138
5.3.2	Controlled qubit-qubit interaction schemes	139
5.4	Bloch oscillations and quantum metrology of electrical current	142
5.4.1	“Orthodox” Bloch oscillations	144
5.4.2	Dispersive Bloch oscillations	148
	Bibliography	154

List of Figures

1-1	Quantum fluctuations in an LC-circuit	19
1-2	Low impedance resonant structures	21
1-3	Uniform disordered superconductor vs. Josephson tunnel junction array . .	24
1-4	Array of Josephson tunnel junctions	25
1-5	Linear modes of the Josephson array	26
1-6	Full circuit model of the Josephson junction array	29
1-7	Classically stationary states of phase-biased Josephson array	32
1-8	Quantum phase-slips spectrum	35
1-9	Example of two tunneling trajectories	37
1-10	Effective tunneling potential	39
1-11	Aharonov-Casher type interference of quantum phase-slip	40
1-12	Aharonov-Bohm type interference of Cooper pair tunneling	41
1-13	Coupling of CQPS to dissipation	42
1-14	Sketch of fluxonium qubit and its readout	44
1-15	Two models of fluxonium circuit	45
1-16	Simplest model of fluxonium spectrum	46
1-17	Inductively shunted junction model of fluxonium	48
1-18	Fluxonium circuit spectrum	50
1-19	Superinductance regime with fluxonium	51
1-20	Dephasing in fluxonium qubit as the evidence of CQPS in array inductance	53
2-1	Fluxonium optical images	55

2-2	Left: Tilted SEM image of a section of the Josephson array from a similar device. Right: SEM image of the black-sheep junction from a similar device.	57
2-3	Circuit QED	57
2-4	Phase and amplitude of the reflection coefficient	59
2-5	Dispersive phase shift	60
2-6	Cryogenic setup	63
2-7	Photographs of the chip holder	65
2-8	Coaxial-to-microstrip adapter	66
2-9	Microwave characterization of the sample holder	67
3-1	Fluxonium spectrum at a glance	72
3-2	Fluxonium matrix elements	76
3-3	Circuit model of the fluxonium-readout resonator interaction	80
3-4	Dispersive shifts of the cavity by an atom with an arbitrary spectrum	82
3-5	Dispersive shifts for several common types of spectra	84
3-6	Origin of dispersive shift by the fluxonium circuit, phase-slip regime	88
3-7	Numerically computed dispersive shifts, phase-slip regime	90
3-8	Origin of dispersive shift by the fluxonium circuit, fluxonium qubit regime	92
3-9	Numerically computed dispersive shifts, the fluxonium qubit regime	93
3-10	Two models of spontaneous emission	96
3-11	Fir-tree garland model of intrinsic dissipation in fluxonium array junctions	98
3-12	Sensitivity of fluxonium transitions to critical current noise	101
3-13	Sensitivity of fluxonium $g-e$ and $g-f$ transitions to fluctuating offset charges on the islands of the array	104
3-14	Translational properties of fluxonium wavefunctions	105
4-1	Modulation of the ground state by magnetic field	108
4-2	Vacuum Rabi resonance of fluxonium qubit	108
4-3	Power dependence of the vacuum Rabi resonance	110
4-4	Two-tone spectroscopy of the fluxonium	111
4-5	Photon number calibration	113

4-6	Power broadening of qubit transitions	114
4-7	Spectroscopy at half flux quantum	115
4-8	Spectroscopy at zero flux	116
4-9	Side-band transitions and the $e \leftrightarrow f$ vacuum Rabi resonance	117
4-10	Large-scale and high-power spectroscopy data	119
4-11	Spectroscopy data after thermal cycling to 77 K	122
4-12	Time-domain measurement of fluxonium decoherence	123
4-13	Time-stability of decoherence times	124
4-14	Time-stability of qubit frequency measured using Ramsey fringes	124
4-15	Energy relaxation data	126
4-16	The T_1 sweet-spot at $\varphi_{\text{ext}} = 0$ of the $f \rightarrow e$ transition	127
4-17	Summary of the fluxonium decoherence	128
4-18	Demonstration of population inversion of the fluxonium transition at $\varphi_{\text{ext}} \simeq \pi$	130
4-19	Raman spectroscopy of fluxonium transitions	131
4-20	Time-domain Raman experiment	132
4-21	Life-time of the qubit state measured as a function of the average cavity photon population n	133
5-1	Exotic Josephson networks	136
5-2	First three states and transitions of a fluxonium qubit with typical parameters.	138
5-3	Inductive coupling of fluxonium qubits by a common array junction	140
5-4	A cluster of fluxonium qubits is connected capacitively to a readout resonator	141
5-5	The quantum metrology triangle	143
5-6	Bloch-oscillating Josephson circuits	144
5-7	Dispersive Bloch oscillations	149

List of Tables

5.1	Specs of the in-stock Josephson array superinductance	134
5.2	Device parameters	153

Acknowledgements

I am delighted to begin this thesis with its most important chapter. In the course of my PhD studies I was fortunate to interact with a number of brilliant people, without whom this work would not have either started, completed, both started and completed, or simply taken its present form.

My deepest gratitude goes to my advisor Michel Devoret. It is non-trivial to find precise words to describe how much I enjoyed being his graduate student. Roughly speaking, discussing with Michel can be compared, perhaps, to exploring a classical masterpiece, be it a movie, a book, or a painting. You can do it over and over, yet you always discover something new on each pass. The scope of his topics apparently does not have a boundary; those we went through included a proper choice of solder and quantum radiation from black holes. I am particularly grateful to Michel for teaching me, with much patience, almost everything I know in modern physics, from basic experimental techniques to some culturological aspects. Every paragraph of this thesis, in one way or another, was written under Michel's influence.

I sincerely thank those great minds who not only directly contributed to this work, but also critically read this manuscript, some of them by candlelight, and served on the defense committee: Steve Girvin, Leonid Glazman, Dan Prober, and Rob Schoelkopf. Your proximity and availability was invaluable for this work's progress.

Much of my understanding of the subject of quantum phase-slip came from Leonid, without whom we would have never come up with fluxonium. I am grateful to Dan for his everyday encouragement, clever suggestions, organizing the Yale-APS receptions, and, of course, for sharing his 40GHz network analyzer. Steve, with his elegant way of com-

municating ideas from other disciplines, made me appreciate atomic physics, the subject I considered, for unknown reasons, dull in college. The (yet to be implemented) idea of laser cooling of Bloch oscillations, presented in the last chapter of this thesis, was born as a result of this appreciation. Each time I thought I thought through everything in my experiment or proposal, Rob would always point out something serious I simply missed. Learning his opinion and suggestions helped me to steer this work into a fruitful direction. It was the success of Rob's clever transmon qubit experiments, which convinced me to investigate the Josephson array superinductance by turning it into a qubit.

A special acknowledgement is due to Luigi Frunzio, who kept our nanofabrication facilities running and enthusiastically shared his tremendous expertise with me in the times of trouble. I note that Fig. 2-2 (left) of this manuscript was taken with him while we were investigating together just another sample issue. He then suggested that the image we took might end up in my future thesis. So it did, thank you Luigi.

On the theory side, this work benefited tremendously from Jens Koch, my powerful direct collaborator, who, among other things, developed a code to efficiently simulate fluxonium properties. Most of theoretical curves used in this work were produced using this code. Jens also taught me theoretical aspects of circuit QED; his encouragement made me choose the robust and convenient (then counterintuitive, now obvious) capacitive, not inductive, coupling scheme of fluxonium to the readout cavity. I am particularly grateful to Jens for his patience and persistence, with which he spread his absolute scientific rigor onto this work. I look forward to our future joint efforts.

On the experimental side, I am truly indebted to Etienne Boaknin, who allocated much of his cheerful energy to introduce me to almost every aspect of experimental physics, starting from microwave and cryogenic equipment, passing through the art of tiny soldering and coil-winding, and ending with preparing talks and writing papers. My experience while being Etienne's protégé during the first two years in the lab turned out crucial for the progress during the remaining years. Mike Metcalfe taught me nanofabrication and invented the Josephson array design used in this work. I admired Mike's efficiency in producing working devices. Later on, I always followed Mike's general advice not to mess with things and simply work quickly, to avoid the ever present $1/f$ noise affecting the

fabrication outcome. Most of the dilution refrigerator experiments I performed would not have been possible without the unlimited help of Marcus Brink. We spend many long nights replacing pumps, changing their oil, fixing the gas handling system, adjusting the mixture concentration, and discussing physics in the meantime. In addition, I thank Marcus for his Mathematica code for generating qubit pulses. Towards the end of this work I had the pleasure to work with talented Nick Masluk and Archana Kamal, who provided some of the decoherence measurements presented here. I especially thank Nick for frequently entertaining me with his vast knowledge of classical physics, and for turning me into a big fan of virtual machines (credit shared with Michel).

With a separate paragraph I thank Vijay, with whom we exchanged almost every day on apparently every theoretical and experimental subject of relevance. Once I had an idea, my first move was to share it with Vijay and learn his opinion. I thank him for always taking his time to listen and provide useful feedback. At some point he attempted to wear headphones to save some time, but I think it did not really work. Vijay's hand and encouragement helped me a great deal during my first independent experiments.

It was also a great pleasure to overlap with Irfan Siddiqi, who taught me one of the most important, in my opinion, experimental physics skill: online searching and keeping track of new exotic component for our experiments. My probably life-long passion for designing microwave sample holders (see Fig. 2-8) is also due to Irfan. I thank all members of Michel's lab, better known as Q(u)lab, with whom we worked jointly on some occasions. I particular enjoyed collaboration on cavity bifurcations with Simon Fissette, on parametric amplification with Nicholas Bergeal, and various discussions with Chad Rigetti.

Acknowledgements are also due to the Girvin/Schoelkopf team members, who maintained the unique culture of highest standards of doing physics research. I acknowledge fruitful discussions and a hand from Lefe Spietz, Hannes Majer, Andreas Wallraff, David Schuster, Lev Bishop, and Leo DiCarlo. I am particularly grateful to David for giving me lots of advice on practical aspects of circuit QED, and to Leo, most importantly for coloring our late night sessions in the lab. I have particularly benefited from the greatest attraction of the 15 Prospect street Becton 4th floor – the Monday Lunch Seminar, a weekly source of inspiration throughout the course of this work.

Outside Yale, I acknowledge fruitful discussions with Konrad Lehnert, Joe Aumentado, Lev Ioffe, and the members of the Saclay Qnantronics Group. I also thank Jens Koch and Lev Ioffe for reviewing this manuscript.

I thank Jo-Ann Bonnett, Sandy Tranquilli, Theresa Evangeliste, and, most of all Maria Gubitosi, for covering my back on the administrating issues, with a mandatory bonus in the form of a smile.

I thank all my friends who stopped me from doing physics outside the lab, especially those who ever attended one of the Yale YANIS gatherings.

Finally, I warmly thank Yulia, Dima Abanin, my brother Georgy, and my parents Irina and Eduard. Research progress somehow accelerated immensely right after our wedding with Yulia. Dima, my closest friend, not only convinced me to go to Yale, but also provided a tremendous amount of his confidence in the happy end of all my research endeavors. I am indebted to my parents Eduard and Irina for suggesting to me a career of a physicist - I was by far not into math&science neither at six nor at twelve - and tirelessly supporting me throughout its course. I dedicate this thesis to them.

List of Symbols

A	–	area
a	–	annihilation operator
α	–	fine structure constant; summation index
b	–	annihilation operator
β	–	summation index
β_L	–	ratio of L/L_J commonly used in RF-SQUID literature
CQPS	–	Coherent Quantum Phase-Slip
C	–	capacitance
C_J	–	capacitance of the Josephson junction
C_{J_j}	–	capacitance of the j -th Josephson junction in the array
C_s	–	stray capacitance
C_g	–	capacitance to ground
c	–	specific capacitance
d	–	distance
Δ	–	superconducting energy gap; qubit-cavity detuning
e	–	electron charge; excited state index
E	–	energy
E_J	–	Josephson energy
E_C	–	charging energy, defined as $E_C = e^2/2C$
E_L	–	inductive energy defined as $E_L = (\Phi_0/2\pi)^2/L$
E_{J_j}	–	Josephson energy of the j -th junction in the array
E_{C_j}	–	Josephson energy of the j -th junction in the array

E_L^Σ	-	inductive energy of the looped array, $E_\Sigma^{-1} = E_L^{-1} + E_J^{-1}$
E_S^Σ	-	combined phase-slip amplitude in the ring, $E_S^\Sigma = E_S + E_{SB}$
E_ϕ	-	inductive energy of the $g \leftrightarrow e$ transition $E_\phi = 4\pi^2 E_L^\Sigma \varphi_{\text{ext}}/2\pi - 1/2 $
E_S	-	phase-slip amplitude in the junction array
E_{S_j}	-	phase-slip amplitude in the j -th array junction
E_{SB}	-	phase-slip amplitude in the black-sheep junction
E_{SA}	-	average phase-slip amplitude in array junctions, $E_{SA} = \overline{E_{S_j}}$
ε_0	-	permeability of vacuum
ε	-	dielectric constant
f	-	third atomic state index
φ	-	phase of array islands; phase across the black-sheep
φ_{ext}	-	external phase bias of array loop
$\tilde{\varphi}$	-	gauge-invariant phase of array islands
Φ	-	generalized flux
Φ_0	-	superconducting flux quantum $\Phi_0 = h/2e$
g	-	atom ground state ; atom-cavity coupling constant
$\Gamma_{\alpha\beta}$	-	relaxation rate for transition $\alpha \rightarrow \beta$
Γ	-	reflection amplitude for microwaves
γ	-	summation index
h	-	Plank's constant
\hbar	-	$h/2\pi$
H	-	hamiltonian
I	-	current
I_0	-	critical current of a Josephson junction
i	-	$\sqrt{-1}$; summation index
j	-	summation index
k	-	wave-vector; summation index
k_B	-	Boltzman's constant
χ	-	dispersive shift
κ	-	resonator linewidth

\mathcal{L}	–	lagrangian
L	–	array inductance
L_J	–	Josephson junction inductance
L_j	–	inductance of the j -th array junction
l	–	specific inductance
l_{kin}	–	specific kinetic inductance
m	–	phase-slip number operator; electron mass
M	–	mutual inductance
μ_0	–	permittivity of vacuum
N	–	number of junctions in the array
n	–	reduced charge operator, $n = Q/2e$; number of photons in the resonator
$\nu (\omega/2\pi)$	–	frequency
$\nu_{\alpha\beta} (\omega_{\alpha\beta}/2\pi)$	–	transition frequency from state α to state β
$\nu_0 (\omega_0/2\pi)$	–	resonance frequency
$\nu_p (\omega_p/2\pi)$	–	plasma frequency of a Josephson junction
$\nu_{p,0}$	–	plasmon vibration frequency with no fluxons in fluxonium loop
$\nu_{p,1}$	–	plasmon vibration frequency with one fluxons in fluxonium loop
O	–	the big-O function
P	–	power
P_{in}	–	input power level before entering the dilution refrigerator
Ψ_α	–	wavefunction of the α -th eigenstate of fluxonium
π	–	area of a unit circle
Q	–	charge; quality factor
q_j	–	offset charge induced at the j -th island
Q_j	–	Aharonov-Casher charge of the j -th phase-slip tunneling trajectory
Q_{ext}	–	quality factor due to dissipation outside the resonator
Q_{int}	–	quality factor due to dissipation inside the resonator
R	–	resistance
R_Q	–	resistance quantum for Cooper pairs, $R_Q = h/(2e)^2$
r	–	radius

ρ	–	electron density
ρ_s	–	superconducting density
S	–	action
S_{euclid}	–	imaginary time (Euclidian) action
S_{U_R}	–	spectral density of voltage quantum noise by a resistor R
S_{I_Y}	–	spectral density of current quantum noise by an admittance Y
T	–	temperature
$T_{\phi}^{\varphi_{\text{ext}}}$	–	dephasing time due to flux noise
T_{ϕ}^L	–	dephasing time due to noise in the value of L
$T_{\phi}^{E_J}$	–	dephasing time due to noise in the value of E_J of black-sheep junction
T_{ϕ}^{CQPS}	–	dephasing time due to coherent quantum phase-slip
T_1	–	energy relaxation time
$T_2(T_{2\text{ECHO}})$	–	decoherence time, in a π -pulse echo experiment
$T_2^*(T_{2\text{RAMSEY}})$	–	length of the Ramsey fringe
t	–	time
τ	–	imaginary time
θ	–	phase across the Josephson junction; phase of the reflected microwave signal
U	–	voltage
V	–	perturbation to the hamiltonian
V_B	–	Ground-state voltage across the junction during Bloch oscillations
V_{BA}	–	Back-action voltage across the junction during Bloch oscillations
ω	–	frequency (in radians)
ω_0	–	resonance frequency
$\Omega_{\alpha\beta}$	–	vacuum Rabi frequency for the transition $\alpha \longleftrightarrow \beta$
Y	–	admittance
Y_{Purcell}	–	admittance of the readout circuit seen by the black-sheep junction
Z_0	–	characteristic impedance of an LC -oscillator
Z_{vac}	–	impedance of vacuum, $Z_{\text{vac}} = \sqrt{\mu_0/\epsilon_0}$
Z_{∞}	–	wave impedance of a transmission line
Z_J	–	characteristic impedance of a Josephson tunnel junction

Chapter 1

Introduction

This thesis work seeks to contribute to the field of quantum electrical circuits [1] by endowing it with a new circuit element – the “superinductance”¹. Superinductance is defined by its two key properties. First, it must superconduct direct current (DC). Second, it must present to an alternating current (AC) the impedance of a frequency-independent inductance L with sufficiently small stray capacitance C_s , such that $\sqrt{L/C_s} > R_Q$, where $R_Q = h/(2e)^2 \simeq 6.5 \text{ k}\Omega$ is the superconducting impedance quantum. The amount of dissipation to the alternating current determines the quality of the superinductance, the weaker the dissipation the better the quality. On the technical side, since quantum circuits operate in the microwave frequency range, the maximum operating frequency of the superinductance, which is for instance limited by the self resonance frequency $1/\sqrt{LC_s}$, should exceed at least $2\pi \times 10 \text{ GHz}$. This latter condition translates into the following numerical estimate for the required magnitude of an inductance operating in the microwave range: $L > 6.5 \text{ k}\Omega/2\pi \times 10 \text{ GHz} \simeq 100 \text{ nH}$.

Remarkably, the practical implementation of such circuit element goes far beyond the scope of radio-engineering. For instance, attempting to wind a regular wire, or even a bulk superconducting wire, into a conventional coil will result in a failure, which, as we shall explain below, can be traced back to the small value of the fine structure constant. Alternatively, attempting to increase the specific inductance of a thin superconducting wire or

¹Term introduced in an unpublished work by A. Kitaev

a thin superconducting film brings about the well-known problem of the superconductor-to-insulator transition [2]. Furthermore, in order to fully test our superinductance against various failure modes, we had to design a novel superconducting artificial atom, nicknamed “fluxonium” [3], and infer the properties of the inductance from the properties of the transition spectrum and the decoherence of this artificial atom. Hence, this work fuses ideas from a variety of fields, including those of quantum condensed matter, quantum optics, quantum information, and, of course, microwave engineering.

The question of implementing a superinductance stands on its own as a basic problem in macroscopic quantum physics of electrical circuits. However, it might also find applications in establishing the quantum standard of electrical current [4, 5, 6, 7] or even in some exotic schemes of quantum information processing [8]. In this thesis we do not discuss the applications of the superinductance, but instead focus on its implementation and testing. The promising readout and coherence properties of fluxonium qubit, to some extent, illustrate the usefulness of such a circuit element. In the two following sections of this introduction we explain the meaning of the superinductance and review in detail the fundamental obstacles to its implementation. We also introduce and motivate our solution using a series array of Josephson junctions with properly chosen parameters. The main novelty of our work with Josephson junction arrays is measurement in the regime of ultra-low dissipation, while the previous experiments [9] were inherently dissipative.

This work is built on a foundation set by a series of key results in the field of quantum electrical circuits. The field itself was probably initiated by A. J. Leggett, who suggested a possibility of observing in an electrical experiment the quantum mechanical behavior of a superconducting circuit [10, 11]. Formalism to treat the effect of dissipation on the circuit degrees of freedom was subsequently developed [12, 13]. On the experimental front, macroscopic quantum tunneling and the quantized energy levels in a superconducting circuit were reported for the first time in 1985 [14, 15]. Quantum coherence in a Cooper-pair box circuit was demonstrated [16, 17], a coherence quality factor of almost 50,000 was reached with the qantronium circuit [18] and the strong coupling of a quantum circuit to a microwave resonator was demonstrated [19], a technique of choice in the present work. It has become clear that electromagnetic vibrations in a superconducting circuit could be,

and perhaps, should be treated in the same way as the motion of an electron in a hydrogen atom.

Quantum-mechanical treatment of quantum circuits is well described in the past thesis works of [20, 21, 22]. Dispersive measurements techniques are developed in the works of [23, 24, 25].

1.1 Linear quantum fluctuations in electrical circuits

1.1.1 Fundamental asymmetry between charge and flux

Let us examine quantum fluctuations in a dissipationless LC circuit described by the generalized flux Φ inside the inductor coil and the displacement charge Q at the capacitor plates (Fig. 1-1). A fluctuation of charge δQ contributes to the total energy of the circuit with capacitive contribution $\delta Q^2/2C$, while the fluctuations of flux $\delta\Phi$ contribute the inductive energy $\delta\Phi^2/2L$. The two energies are equal by virtue of the virial theorem and also equal to the half a photon of zero-point motion energy $\frac{1}{2}\hbar\omega_0$. Therefore, we get $\delta Q^2 = \frac{1}{2}\hbar/Z_0$ and $\delta\Phi^2 = \frac{1}{2}\hbar Z_0$, where we introduced characteristic impedance of the resonator $Z_0 = \sqrt{L/C}$ and the resonant frequency $\omega_0 = 1/\sqrt{LC}$. Thus, irrespective of the resonance frequency, high impedance oscillators have large flux fluctuations and small charge fluctuations and vice versa for low impedance oscillators, verifying at all times Heisenberg's uncertainty relation. Let us introduce the superconducting flux quantum $\Phi_0 = h/2e \simeq 2.0 \times 10^{-15}$ Wb, the superconducting resistance quantum $R_Q = h/(2e)^2 \simeq 6.5$ k Ω , and express flux and charge fluctuations in terms of the charge and flux quanta, namely

$$\begin{aligned} \delta Q/2e &= \sqrt{\frac{1}{4\pi} R_Q/Z_0} \\ \delta\Phi/\Phi_0 &= \sqrt{\frac{1}{4\pi} Z_0/R_Q} \end{aligned} \tag{1.1}$$

In other words, 6.5 k Ω is a characteristic impedance scale for Z_0 which decides whether charge or flux fluctuate by an amount less or more than their respective fundamental units. We will therefore refer to impedances $Z_0 < R_Q$ as low and $Z_0 > R_Q$ as high. Low impedance

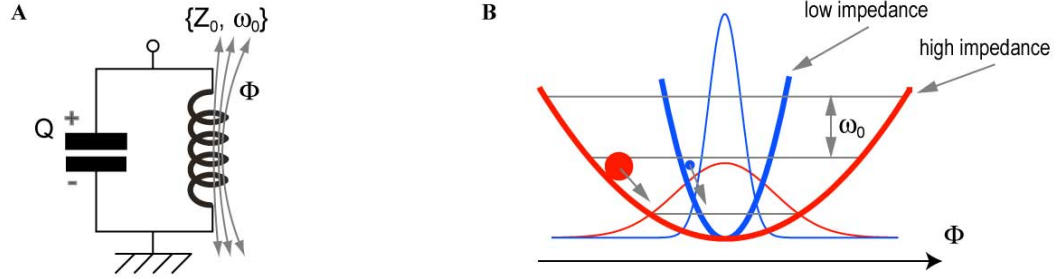


Figure 1-1: Quantum fluctuations in an LC-circuit. (A) Capacitance C in parallel with an inductance L . Alternatively such circuit may be described by the frequency $\omega_0 = 1/\sqrt{LC}$ and impedance $Z_0 = \sqrt{L/C}$. The flux in the inductance is Φ and the displacement charge on the capacitance is Q . (B) Flux representation of two LC oscillators with the same frequency but different impedance. Thick lines (blue - lower impedance, red - high impedance) represent parabolic inductive energies. Thin lines (same color scheme) represent ground-state wavefunctions. The higher the impedance, the larger the quantum fluctuations of flux, irrespective of frequency.

oscillators keep flux in the inductance localized on the scale of flux quantum while high impedance oscillators localize charge on the capacitance plates below the single Cooper pair level. Now it is clear that the sub-Cooper pair fluctuations of charge are only possible with the superinductance.

In typical radio-frequency electrical circuits, inductances and capacitances come, respectively, from magnetic and electric fields stored in the vacuum space between the circuit parts. It turns out that electromagnetic parameters of vacuum, namely the vacuum permeability ϵ_0 and the vacuum permittivity μ_0 in that case restrict the impedance Z_0 of such circuits to “low” values. Let us illustrate this point with two readily calculable physical implementations of an LC -circuit (Fig. 1-2). As a first example, consider two cylindrical parallel wires of radius r separated by a distance d small compared to the wavelength, shorted-circuited at one end and left open at the other end (Fig. 1-2-A). The resulting transmission line can be modelled as a chain of inductance-capacitance cells where the specific inductance of the wires is calculated to be $l = \mu_0 \log(d/r)/\pi$ and the specific capacitance between the wires is $c = \epsilon_0 \pi / \log(d/r)$ [26]. The frequency-dependent input impedance of the transmission line

can be derived from the telegrapher's equation [26]:

$$Z(\omega) = Z_\infty \frac{e^{i\pi\omega/\omega_0} - 1}{e^{i\pi\omega/\omega_0} + 1} \quad (1.2)$$

where we have introduced the wave impedance $Z_\infty = \sqrt{l/c}$ and the quarter-wavelength resonance frequency $\omega_0 = \frac{\pi}{2}/(\sqrt{lc} \times \text{“length”})$. At low frequencies, the impedance $Z(\omega \rightarrow 0) \rightarrow i\frac{\pi}{2} \frac{Z_\infty}{\omega_0} \omega$ behaves inductively with the effective inductance value of $\frac{\pi}{2} Z_\infty / \omega_0$. Close to the resonance $\omega \rightarrow \omega_0$, the input impedance $Z(\omega)$ coincides with that of a parallel LC oscillator with the resonance frequency ω_0 and characteristic impedance $Z_0 = \frac{4}{\pi} Z_\infty$. Note that the transverse dimensions of our two-wire transmission line contribute very little² to its wave impedance. Namely, the wave impedance is given by $Z_\infty = Z_{\text{vac}} \log(d/r)/\pi$, where we introduce vacuum impedance Z_{vac} , given by $Z_{\text{vac}} = \sqrt{\mu_0/\epsilon_0} = 377.0 \Omega \ll R_Q$, resulting in $Z_0 \ll R_Q$. Essentially, as one increases the inductance by increasing the length of the wire, its self-capacitance increases proportionally, thus resulting in the characteristic impedance of order Z_{vac} .

As a second example, let us attempt to reduce the self-capacitance of an inductor by spreading the two wires from the previous example as far apart from each other as possible (Fig. 1-2-B). Here the catch is that as soon as the separation between the wires reaches the wavelength, the circuit starts to lose energy by radiating into the free space. The effect of radiation boils down to shunting the two terminals of the circuit with an effective radiation resistance $R_{\text{rad}} = \text{Re}[Z(\omega)]$ given by the standard theory of electric dipole radiation [27],

$$R_{\text{rad}} \approx Z_{\text{vac}} (\omega_0/\omega)^4 \quad (1.3)$$

While the radiation effect is drastically suppressed at low frequencies, at frequencies $\omega \rightarrow \omega_0$ the radiation matches to the free space and the wire is effectively shunted by the vacuum again, even though its total zero-frequency self-capacitance is somewhat reduced. A wide loop behaves just as an infinitely long transmission line with $Z_\infty = Z_{\text{vac}}$, a situation analogous to the previous example.

²The phase velocity of the electromagnetic waves in this structure does not depend at all on the transverse dimensions and coincides with the speed of light in vacuum.

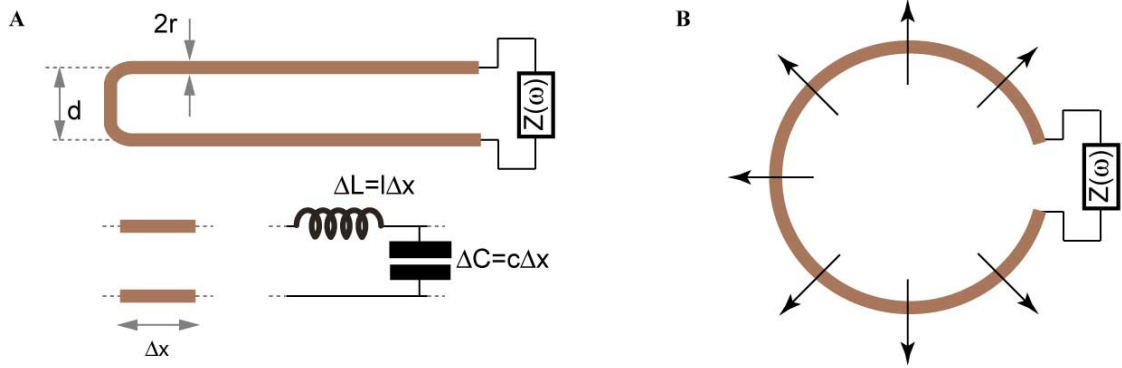


Figure 1-2: Low impedance resonant structures. (A) Parallel-wires transmission line, wire radius is a and the separation is d . The wires are short-circuited at the left end, the impedance measured at the right end is $Z(\omega)$. Inset below shows the electrical ladder model of a section of this transmission line of length Δx . (B). A loop with the circumference identical to the length of the transmission line from (A). Arrows indicate radiation into free space, once the size of the loop approaches the wavelength.

Although the intelligently chosen geometry of commercially available miniature on-chip inductors does reduce, to some extent, the effects of radiation and stray capacitance, low impedance parasitic resonances are unavoidable³. The situation is further worsened by the fact that microwave circuits have to be fabricated on substrates with the dielectric constant of about 5 – 10 (corundum, silicon, etc.) which further reduces the wave impedance of the medium. In fact, electrical engineers chose the design wave impedance to be 50Ω and not 377Ω for this reason.

We therefore conclude this section with a statement that Nature favors small quantum fluctuations of flux and large quantum fluctuations of charge when compared to their quantum units. Or, equivalently, Nature hates superinductors. To emphasize the fundamentality of this asymmetry between charge and flux, we note the following relation:

$$\frac{\delta\Phi/\Phi_0}{\delta Q/2e} \lesssim \frac{Z_{\text{vac}}}{R_Q} = 8\alpha \quad (1.4)$$

where $\alpha \simeq 1/137.0$ is the fine structure constant

³It might appear that the inductance of a transmission line at frequencies $\omega = \omega_0 - \delta\omega$ effectively (Eq. 1.2) diverges at small $\delta\omega$ with a value of $-i \frac{dZ}{d\omega} \approx Z_\infty/\delta\omega$. Nevertheless, such resonant increase of inductance does not play any role in quantum fluctuations. What counts is the strength of the pole in the impedance function, which is our vacuum-limited characteristic impedance Z_0 .

1.1.2 Kinetic inductance

Clearly, to beat the vacuum impedance and to offset the asymmetry between charge and flux one must abandon geometric inductances. One well-known non-geometric contribution to the inductance originates from the inertia of the charge carriers, the so-called kinetic inductance. Inertia of charge carriers in a normal metal becomes noticeable at frequencies ω exceeding the inverse momentum relaxation time τ . For $\omega\tau \gg 1$, a wire of cross-sectional area A , with electron mass m , and electron density ρ has total kinetic inductance per unit length l_{kin} given by [28]

$$l_{\text{kin}} = m/Ae^2\rho \tag{1.5}$$

In the case of a 100 nm wide and 10 nm thick strip of copper, specific kinetic inductance at room temperature would be comparable to μ_0 . However, in radio-frequency circuits effects of kinetic inductance are always masked by the dissipation, because the dissipative Drude resistance, given by $m/Ae^2\rho\tau$, dominates the impedance $l_{\text{kin}}\omega$ due to kinetic inductance up to the frequencies of order $1/\tau$, which easily extends to the THz range.

In superconducting wires, kinetic inductance manifests itself much more strongly because densities of normal and superconducting electrons can be made vastly different⁴. In fact, as the superconductor approaches its transition temperature, the superconducting density reduces and causes diverging kinetic inductance [29]. Unfortunately, the decrease of the Cooper pair density close to the transition point is always accompanied by the increase of normal electron density which results in more unwanted dissipation (at finite frequency). At low temperatures, the effect of breaking of Cooper pairs by external radiation on the kinetic inductance of thin films is successfully used for the design of sensitive detectors for a broad frequency range with important applications in radioastronomy [30] or general purpose single-photon detectors [31].

A non-dissipative enhancement of kinetic inductance in a superconductor may be pos-

⁴Let us provide here an interpretation of kinetic inductance in terms of the Meissner effect. Namely, an electrical current in a superconducting wire generates the twist of a superconducting phase across the wire. This twist in phase, or the gradient $\nabla\varphi$, costs energy $\int dV\rho_s(\nabla\varphi)^2$, where ρ_s is the density of the superconducting condensate. Increasing kinetic inductance is thus equivalent to reducing the stiffness of the superconducting state.

sible by keeping the temperature close to zero but introducing strong disorder. Now, the Cooper pair density can be suppressed without generating normal conduction electrons because of partial localization of charge carriers. However, increasing l indefinitely requires $\rho \rightarrow 0$, which cannot be great for the superconducting state. For instance, reduced density eventually increases the Coulomb interaction and therefore destroys the superconducting pairing [32]. Unfortunately, both theory and controlled fabrication of disordered superconductors are challenging. On the contrary, a clean and comfortably thick superconducting wire interrupted by a large number of Josephson tunnel junctions represents one particular case of a “disordered” wire which is excellently suited for both transparent theoretical analysis and controlled experiments (Fig. 1-3). In a tunnel junction, the Cooper pair density is only suppressed inside a nm-thick insulating oxide. This bottleneck dominates the total kinetic inductance. The current I and superconducting phase difference θ across the junction obey to the Josephson relation $I = I_0 \sin \theta$, where I_0 the maximum possible supercurrent of the junction⁵. For small currents, Josephson relation implies that the junction is just a linear inductance with magnitude $L_J = \frac{1}{2\pi} \Phi_0 / I_0$. Due to the Ambegaokar-Baratoff relation [29], the Josephson inductance L_J is linked to the junction normal resistance R_N and superconducting energy gap Δ as $L_J = \frac{\pi}{4} R_N / \Delta$ [Hz]. Therefore, the stronger the tunneling barrier, the larger the inductance. A similar relation between inductance per square and resistance per square holds for highly disordered but structurally continuous films. Clearly, the value of kinetic inductance L_J has nothing to do with vacuum permeability μ_0 and may well beat its value with proper choice of junction parameters. For instance a choice of $Al/AlOx/Al$ tunnel junction with a comfortably achievable combination of size of $1 \mu\text{m}$ and critical current of $1 \mu\text{A}$ possesses specific inductance as large as $300\mu_0$, corresponding to the geometric inductance of a wire approximately $300 \mu\text{m}$ long.

⁵The phase θ is defined by $\theta(t) = \frac{2e}{\hbar} \int_{-\infty}^t dt' V(t')$, where $V(t)$ is the voltage between the junction electrodes defined as $V(t) = \int d\vec{l} \cdot \vec{E}$, where E is the electric field and the integration path goes through the junction oxide.

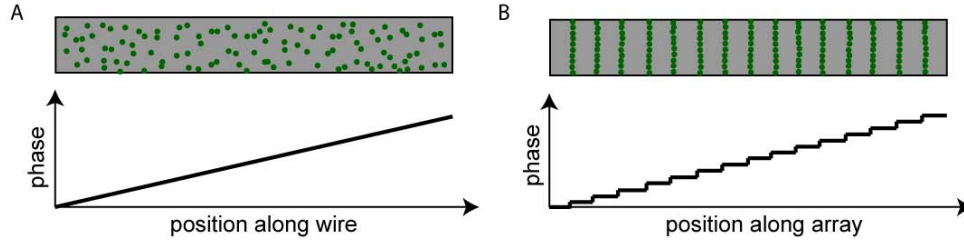


Figure 1-3: Uniform disordered superconductor vs. Josephson tunnel junction array. (A) Usual disordered wire with randomly distributed scatterers. Superconducting phase is a continuous function of the coordinate across the wire. (B) A particular implementation of disordered wire, in which all the scatterers are combined into a set of discrete tunneling barriers, tunneling junctions, between clean superconducting islands. In this case the superconducting phase is fixed within an given island and changes step-like across the junctions.

1.1.3 Superinductance with Josephson junction array

For frequencies approaching zero, the inductance of the array is obviously given by $L = N \times L_J$. However, for the inductance to operate at a finite frequency, the physical length of the array, or equivalently the number of junction N , also has to be finite. This is a familiar effect that both inductance and its stray capacitance of a piece of metallic wire grow with its size [33] and therefore the longer the wire, the lower its parasitic resonance. In fact, simple analysis of Eq. (1.2) show that above the self-resonance frequency, an inductance turns into a capacitance. Therefore, let us begin by figuring out the optimum length of the junction array which maximizes both its total inductance and operating frequency.

Junctions are fabricated on an insulating silicon substrate as a series of overlapping films separated by the layer of aluminum oxide (Fig. 1-4). Each superconducting island is thus connected to its neighbor island by a parallel-plate type capacitance C_J and Josephson inductance L_J . The frequency $\omega_p = 1/\sqrt{L_J C_J}$ is called junction plasma frequency. Given that $C_J \sim A$, with A being junction area, and $L_J \sim R_N \sim 1/A$, the plasma frequency does not depend on the junction dimensions and is mainly determined by the transparency of the barrier or equivalently by the critical current density. For Al/AlOx/Al junctions $\omega_p \approx 10-40$ GHz, which is a few times lower than the Cooper pair breaking frequency $2\Delta \approx 80$ GHz. Every island also possesses a certain capacitance “to ground” C_g . Even when the chip carrying the circuit is mounted far away from metallic objects, some capacitance C_g still

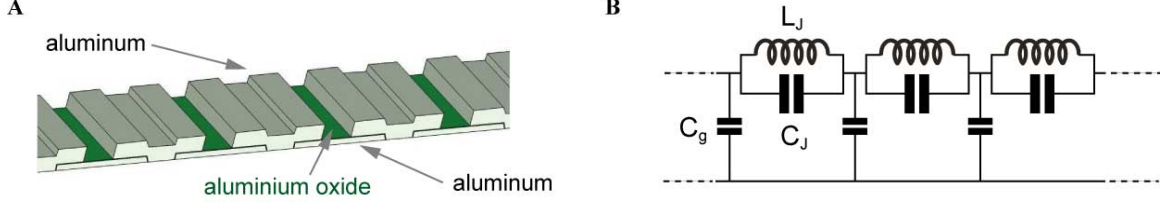


Figure 1-4: Array of Josephson tunnel junctions. (A) Sketch of the physical implementation. Gray regions indicate superconducting islands (aluminium), green layer indicates the tunneling barriers oxide (aluminium oxide). (B) Linear electrical circuit model. L_J stands for Josephson inductance, C_J for the oxide capacitance and C_g is the capacitance of the islands to the nearest metallic object, inevitably present in any experimental realization.

comes from capacitive coupling of the islands to the neighboring on-chip metallic structure. Roughly, this non-parallel plate type capacitance scales linearly with island dimensions (note the analogy with the transmission line specific capacitance) and is essentially impossible to get rid of. A fair evaluation would be to $C_g \approx \varepsilon_0 \varepsilon \sqrt{A} \approx 10 - 100 \text{ aF}/\mu\text{m}$.

The propagation of the electromagnetic waves in the Josephson array can be modelled by a dispersive transmission line (Fig. 1-4) with the following relation between the wave-vector k and the frequency ω [34]:

$$k(\omega) = \omega \frac{\sqrt{L_J C_g}}{\Delta x} \frac{1}{\sqrt{1 - \omega^2/\omega_p^2}} \quad (1.6)$$

where Δx is the physical length of the unit cell. For frequencies $\omega \lesssim \omega_p/2$ the dispersion relation is nearly linear, which can be interpreted as neglecting the AC current path via the capacitances C_J . Boundary conditions determine the frequencies of the standing wave modes. Figure 1-5 shows an example solution for the open-short boundary condition, which translates into $N\Delta x = \frac{\pi}{k(\omega_n)}(n + 1/2)$, where n takes integer values starting from zero. Qualitatively, other boundary conditions are equivalent for our purpose. For frequencies below the first standing wave resonance, $\omega < \omega_{n=0}$, the response of the array is purely inductive, with inductance $L = L_J N$. Clearly, the highest operation frequency for this inductance will be achieved if we push $\omega_{n=0}$ all the way towards the plasma frequency ω_p . Note that all other modes of the array bunch up slightly below the plasma frequency of the junctions. By setting $\omega_{n=0} = \omega_p$ we get the following estimate for the maximum number of junctions:

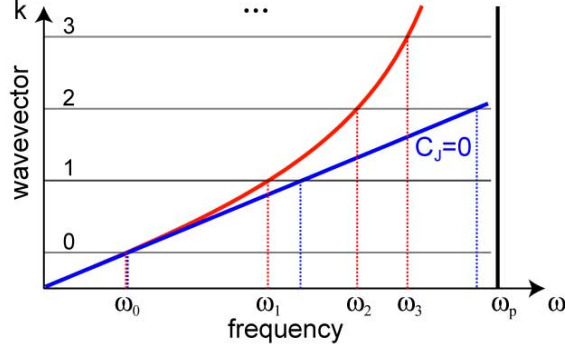


Figure 1-5: Linear modes of the Josephson array. Blue line – nondispersive linear $k(\omega)$ relation for $\omega_p = 1/\sqrt{L_J C_J} \rightarrow \infty$. Red line – dispersive $k(\omega)$ for finite ω_p . The indexed set of horizontal lines correspond to the condition of having quantized number of quarter wavelength matching the length of the transmission line. Corresponding solutions are found geometrically and marked on the x-axes with ω_n , $n = 0, 1, 2, \dots$

$$N \lesssim \sqrt{C_J/C_g} \quad (1.7)$$

Equation (1.7) in practice severely limits the number of junctions N . Even if the stray capacitance C_g is factor of 10^3 smaller than C_J , the number of junction N is limited to a number of about only 30! The larger the inductance gets, the less stray capacitance it needs to undesirably resonate at a given frequency; vacuum shunts kinetic inductances as well as the geometric ones.

With N severely limited, the next question is in order: how large can we make the inductance per junction L_J , before something unwanted happens? In other words, how strongly can we make the “disorder” in a superconductor without destroying the superconducting behavior? Given that $N < \sqrt{C_J/C_g}$ and $\omega < \omega_p$, we can continue our analysis ignoring C_g . Then, the quantum fluctuations of the Josephson phase will be determined again by formulas (1.1). As we increase L_J , say by reducing the junction area A , the junction effective impedance $Z_J = \sqrt{L_J/C_J} \sim A$ also grows proportionally and causes the phase to fluctuate by an amount $\delta\theta = \sqrt{\pi Z_J/R_Q} \sim \sqrt{A}$. Clearly when the impedance Z_J approaches R_Q , the phase fluctuation $\delta\theta$ approaches π and the junction can no longer be treated as a linear circuit. Since the phase fluctuations cause current fluctuations, the condition $\delta\theta \sim \pi$ is

equivalent to the condition $\delta I \sim I_0$, which clearly marks the end to a simple linear kinetic inductance behavior of a Josephson tunnel junction. Another way to put this is that a Josephson junction behaves as an inductance only if it is shunted by a sufficiently large capacitance. We can now explicitly write down the absolute upper limit estimate for the kinetic inductance L of a Josephson array:

$$\omega L|_{\max} \lesssim R_Q \sqrt{C_J/C_g} \quad (1.8)$$

Thus, according to purely linear analysis, superinductance appears possible for frequencies below ω_p provided one minimizes the ground capacitance C_g by tightly packing $N = \sqrt{C_J/C_g}$ Josephson tunnel junctions with impedance of order R_Q .

In view of the discussion above, the following question arises: can one reach a superinductance regime with a single junction? Indeed this would only require junctions with impedance $Z_J > R_Q$. We have already indicated that the junctions with $Z_J > R_Q$ cannot be treated linearly, because of large quantum fluctuations of Josephson phase. This question brings us to the topic of quantum phase-slip, developed in the next section.

1.2 Quantum phase-slip

The linear considerations of the previous section completely ignore the fact that the thermodynamics of superconductors actually forbids making superinductors out of superconductors in equilibrium. Indeed, the amount of flux fluctuations in a superinductance is similar or even greater than the flux quantum, see Eq. (1.1). Equivalently, the phase difference between the two ends of the superinductance wire approaches or exceeds the value of 2π . This behavior is clearly inconsistent with the thermodynamics of a superconductor, as its free energy must be a 2π periodic function of the phase difference. Thus, the equilibrium current reaches a maximum at a phase difference of π and then oscillates with a further increase of phase difference.

In a narrow wire (thinner than the coherence length), the adjustment of the supercurrent to the equilibrium value is achieved by the transient processes of 2π phase-slips (PS) of the macroscopic wave function [2]. As the wire becomes thinner, the phase-slips occur more

frequently. Furthermore, at low temperature and for sufficiently small wire diameters, quantum phase-slips (QPS) take over the thermally activated ones, leading to an activationless relaxation of supercurrent .

It is important to notice that the conditions of the continuity and single-valuedness of the macroscopic wave function allow a $2\pi m_i$ discontinuity of its phase at any point x_i along the wire (here m_i are integers). At fixed phase difference between the ends of the wire, an observable quantity, such as supercurrent, depends on $m = \sum_i m_i$, but is independent of the specific locations x_i . This is why m can be used to label different quantum states of the condensate. A 2π -phase slip, occurring at some point along the wire, changes the value of m by π . Because the state of the wire is characterized by the sum $m = \sum_i m_i$ rather than by each m_i separately, any of these 2π -QPS results in the transition $m \leftrightarrow m \pm 1$. The QPS processes a priori do not have to be dissipative [35]. In the absence of dissipation, QPS happening at different points along the wire interfere with each other [36, 37]. The resulting superpositions of QPS depend on the distribution of the electric charge along the wire due to a circuit analog of Aharonov-Casher effect [38]. We refer to these spatially interfering quantum phase-slips as coherent quantum phase-slip (CQPS).

The thinner the wire, the larger the amplitude E_S of CQPS and quantum uncertainty of m are. The amplitude E_S has units of energy, and the magnitude of $|E_S|/h$ has the meaning of frequency associated with the CQPS process. In the case of a long Josephson junction array, the magnitude of E_S is controlled by the dimensionless junction impedance Z_J/R_Q . Proliferation of CQPS was predicted to destroy superconductivity in ultra-thin long wires in the following sense: the equilibrium maximum supercurrent (prescribed by the periodic phase dependence of the free energy) decreases exponentially with the increasing length of the wire [37], rather than being inversely proportional to it.

In this work, we are interested in the phenomenon of CQPS in view of the following question: how do the quantum properties of an electrical circuit change, if the superconducting wires, which form the inductances of this circuit, undergo CQPS? Thinking practically, to what value should one suppress the CQPS amplitude in the superinductance, to safely forget about their existence. In this section we describe quantitatively the effect of CQPS in the case of a Josephson tunnel junction array. Apart from the quantitative estimate of

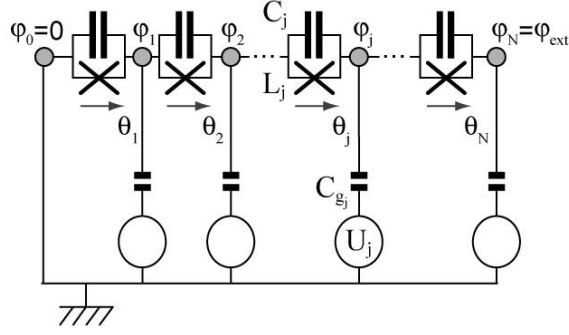


Figure 1-6: Full circuit model of the Josephson junction array. Superconducting islands are labeled with circles, the phase difference across the junction indexed j is given by θ_j . Josephson inductance of this junction is L_j and capacitance is C_j . The island phase is the sum of the junction phases preceding the island, starting from the ground. The phase of the last island is set externally to φ_{ext} . Capacitances to ground are introduced only to model the offset charges using voltage sources.

the value of E_S via the tunnel junction parameters, the considerations of this section apply equally well to the case of continuous superconducting wires

Before immersing into the quantum phase-slip physics, let us briefly summarize our answer to the question raised in the previous paragraph. At zero temperature, quantum phase-slips indeed destroy superconducting order in a sufficiently narrow and infinitely long wire. However, in a finite-length wire, CQPS would manifest themselves simply as shifts of energy levels in the excitations spectrum of an electrical circuit incorporating this wire. The shifts are proportional to the CQPS amplitude $|E_S|$, and depend on the details of the circuit, but never exceed $|E_S|$. Phase-slips occurring at different locations along the wire (or at different junctions in the array) interfere with each other. Due to the Aharonov-Casher effect, the resulting full amplitude of a phase-slip depends on the offset charges surrounding the wire. Slow temporal fluctuations of the offset charges make the phase-slips amplitudes random functions of time, and therefore turn energy levels shifts into linewidths. Thus, the phenomenon of CQPS limits the operating frequency of a superinductance from below by a frequency given by approximately $|E_S|/h$.

1.2.1 “Microscopic” lagrangian and stationary states

Consider an array of N junctions (Fig. 1-6), where the j -th junction is described by the superconducting phase difference θ_j , the Josephson energy E_{J_j} , and the charging energy $E_{C_j} = e^2/2C_j$. Junctions connect N superconducting islands, labeled accordingly with phases $\varphi_j = \sum_{i=1}^{i=j} \theta_i$. There is actually one more boundary island corresponding to $j = 0$, but we choose to ground it and assign it a zero phase ($\varphi_0 = 0$). The phase of the last island is set externally with respect to the ground as $\varphi_N = \varphi_{\text{ext}}$. In the following we count j from 1 to N . Capacitances of the island to ground $C_{g_j} \rightarrow 0$ are considered infinitesimal and only employed, in conjunctions with diverging voltages $U_j \rightarrow \infty$, to model finite offset charges on the islands, $q_j = C_{g_j}U_j$. It is convenient to introduce the total linear inductance of the array $L = \sum L_j$, where $L_j = (\Phi_0/2\pi)^2/E_{J_j}$ is the Josephson inductance of individual junctions. By expressing the Josephson and charging energies of the circuit elements via the generalized coordinates θ_j and velocities $\dot{\theta}_j$ we arrive at the following lagrangian with a constraint ⁶:

$$\mathcal{L} = \sum E_{J_j} \cos \theta_j + \frac{1}{2}(\Phi_0/2\pi)^2 \sum C_j \dot{\theta}_j^2 + (\Phi_0/2\pi) \sum \dot{\theta}_j \sum_{i=j}^N q_i \quad (1.9)$$

$$\sum \theta_j = \varphi_{\text{ext}} \quad (1.10)$$

In the limit of large junction capacitances $C_j \rightarrow \infty$, it is energetically favorable to have $\dot{\theta} \rightarrow 0$. Therefore, let us first find the stationary ($\dot{\theta}_j = 0$) distributions of phases θ_j which minimize the total inductive energy of a phase-biased array (Fig. 1-7). The simplest solution is given by $\theta_j^{\{0\}} = \varphi_{\text{ext}}L_j/L$ or $\varphi_j^{\{0\}} = j \times \theta_j$, $E_{\text{ind}}^{\{0\}}(\varphi_{\text{ext}}) \simeq \frac{1}{2}(\Phi_0/2\pi)^2 \varphi_{\text{ext}}^2/L$. In the case of a homogeneous array we get $\theta_j^{\{0\}} = \varphi_{\text{ext}}/N$, $\varphi_j^{\{0\}} = j\varphi_{\text{ext}}/N$ (Fig. 1-7-A, top). The solution $\varphi_j^{\{0\}}$ simply corresponds to a phase distribution along a linear inductive wire under phase bias φ_{ext} . Interestingly, the 2π -periodicity of the Josephson energy brings about another type of stationary phase distribution, namely $\theta_j^{\{\pm 1\}} = (\varphi_{\text{ext}} \mp 2\pi)L_j/L \pm 2\pi\delta_{jk}$, and $E_{\text{ind}}^{\{\pm 1\}} = \frac{1}{2}(\Phi_0/2\pi)^2(\varphi_{\text{ext}} \mp 2\pi)^2/L$ (Fig. 1-7-top). Here, an integer $k \in [1, N]$ indicates a particular junction which has “slipped” – undergone a large phase change approaching

⁶It might appear that this lagrangian describes a system of completely decoupled junctions. Actually, the coupling is hidden in the constraint (1.10).

$\pm 2\pi$, in sharp contrast to the phases of other junctions being of order $O(1/N)$. Generalizing, we write down stationary solutions corresponding to a total of m “slipped” junctions (one junction can contribute multiple slips) as (Fig. 1-7-A, bottom):

$$\begin{aligned}\theta_j^{\{m\}} &= (\varphi_{\text{ext}} - 2\pi m)L_j/L + 2\pi m_i \delta_{jk_i}, \quad m = \sum m_i \\ \varphi_j^{\{m\}} &= \sum \theta_j \\ E_{\text{ind}}^{\{m\}} &= \frac{1}{2}(\Phi_0/2\pi)^2(\varphi_{\text{ext}} - 2\pi m)^2/L\end{aligned}\tag{1.11}$$

where $k_i \in [1, N]$ indicates those junctions which have slipped m_i times⁷.

To understand the nature of the stationary states and especially the physical meaning of the integer m , we introduce the gauge-invariant phase $\tilde{\varphi}_j = \varphi_j - \varphi_{\text{ext}} \sum_{i=0}^j L_i/L$ and visualize it at every island by an angle between an arrow and the vertical line for the cases of $m = -1, 0$ and 1 (Fig. 1-7-B). This way, two important properties of solutions (1.11) become apparent. First, all the locations in the θ -space, which are labeled with the same m but different k , actually coincide in the real space, i.e. are all physically indistinguishable. By looking at a twisted phase-distribution (Fig. 1-7-B, red or green), it is impossible to tell which particular junction has slipped. Therefore, the stationary states of the array are entirely classified by a single integer m . Second, the fact that m is an integer can be given a topological interpretation. Indeed, m counts the number of full 2π turns (or twists) that the phase $\tilde{\varphi}_j$ accumulates on its way from the left end of the array to the right end. In the limit of $N \rightarrow \infty$, no continuous transformation exists to change $\tilde{\varphi}_j^{\{m\}} \rightarrow \tilde{\varphi}_j^{\{m\pm 1\}}$, hence the states with different m are distinct in the topological sense. For large N , we can establish a correspondence with the vorticity of a continuous superconducting wire:

$$m = \frac{1}{2\pi} \sum_{j=1}^N (\tilde{\varphi}_j - \tilde{\varphi}_{j-1}) \rightarrow \frac{1}{2\pi} \int \nabla \tilde{\varphi}(l) dl = 0, \quad \pm 1, \quad \pm 2, \quad \dots\tag{1.12}$$

Turning to the physical interpretation of the stationary states of the array, let us recall

⁷For a given N , index m cannot span to infinity and is approximately limited by a relation $m^2 \Phi_0^2/L < \min E_{J_j}$

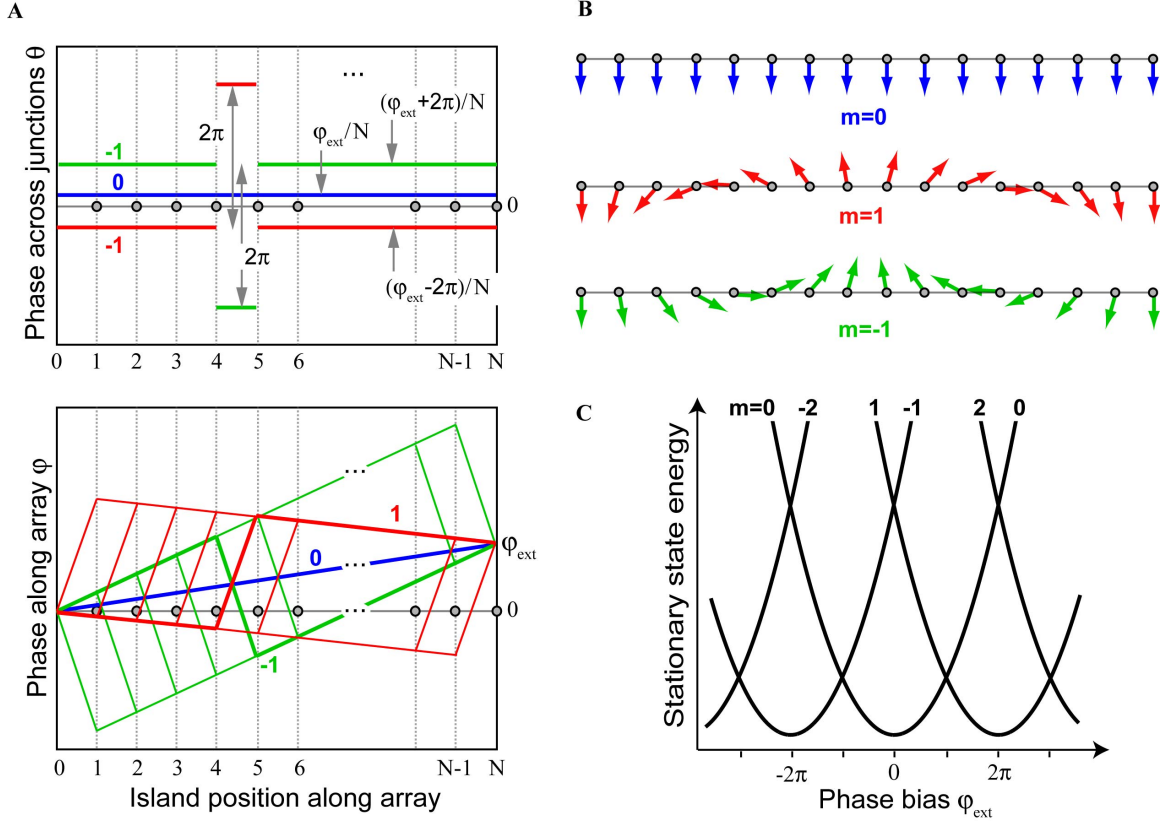


Figure 1-7: Classically stationary states of phase-biased Josephson array. (A)-top. Three solutions for θ_j corresponding to $m = 0, 1,$ and -1 (blue, red, and green, respectively) 2π -phase twists along the array, for the case of $k = 5$ (fifth junction only slips). (A)-bottom. Solution for φ_j , the labeling scheme identical to the top graph. Thick lines highlight the case of $k = 5$, while the thin lines show all possible cases. (B). Gauge-invariant island phases are shown as angles between the arrows and the vertical. (C). Inductive energy of the stationary states. Each parabolic branch corresponds to a different number of 2π phase-twists along the array.

that a finite phase θ across a junction with the Josephson energy E_J generates a supercurrent $I = 2\pi(E_J/\Phi_0)\sin\theta$. For $m = 0$ the supercurrent through the array is generated entirely by the external phase bias φ_{ext} , and the array responds just like a linear inductance L . On the contrary, for every state with $m \neq 0$, there is supercurrent exactly the same as a linear inductance L would generate under phase bias of $2\pi m$. This supercurrent is associated with the inductive energy of m quanta of superconducting flux. Therefore, the energy of the stationary states $E_{\text{ind}}^{\{m\}}(\varphi_{\text{ext}})$ as a function of phase bias is given by a set of 2π -shifted parabolas, where each parabola corresponds to a topologically different phase distribution along the array. In other words, every m -th stationary state of the Josephson array is equivalent to that of a linear inductance L precharged with m flux quanta(Fig. 1-7-C).

1.2.2 Emergent quantum phase-slip hamiltonian

Dynamics in the array originates from the finite charging energy in which the junction capacitances introduce inertia to the θ degrees of freedom. The simplest type of motion then consists of small-amplitude vibrations around the stationary states in the θ -space at frequencies of order junction plasma frequency. Such motion is essentially classical and has been considered in the previous section. Hence, the total phase-twist along the array is conserved, and the number m still remains an integral of motion. Since we are anyway concerned with the properties of the array for frequencies $\omega < \omega_p$, it is safe to assume that the array remains in its vibrational ground state. However, even in the absence of excited vibrations, none of the states with fixed number of 2π -phase twists is the true quantum ground state. In addition to vibrations, the finite inertia of the θ degrees of freedom also generates tunneling between the different locations of the local energy minima in the θ -space. In contrast with the simple small-amplitude vibrations, tunneling gives rise to transitions between the states of the array differing by the number of 2π phase-twists along its length, thus turning m into a quantum-mechanical variable.

Consider the tunneling process between the states with $m = 0$ and $m = 1$ phase-twists (Fig. 1-7-B, C). At $\varphi_{\text{ext}} = \pi$ the two states are degenerate with the energy $\frac{1}{8}\Phi_0^2/L$, but any intermediate phase distribution would correspond to a larger energy. Indeed, since the two states are topologically distinct, the phase across one of the junctions must “slip” to

produce or undo the 2π phase-twist along the array. During the slip, the junction phase goes continuously through the value of $\theta_j = \pi$, and raises the total energy of the array by approximately $2E_j \gg \Phi_0^2/L$, a quantity much larger than the inductive energy scale in the limit of large number of junctions. However, the transition $m \leftrightarrow m + 1$ may occur by quantum-mechanical tunneling, a fully reversible process in the absence of dissipation in the system. Such tunneling can be described phenomenologically with a hamiltonian $H_{\text{tunnel}} = \frac{1}{2} (E_S |m = 0\rangle \langle m = 1| + E_S^* |m = 1\rangle \langle m = 0|)$, where the parameter E_S sets the phenomenological tunneling amplitude. The tunneling coherently mixes the classical states $|m = 0\rangle$ and $|m = 1\rangle$ into their symmetric (ground state) $|g\rangle = (|m = 0\rangle + |m = 1\rangle)/\sqrt{2}$ and antisymmetric (first excited state) $|e\rangle = (|m = 0\rangle - |m = 1\rangle)/\sqrt{2}$ combinations. The energy splitting between $|g\rangle$ and $|e\rangle$ is given by $|E_S|$. We prefer to call $|E_S|$ as the quantum phase-slip energy, or equivalently, the quantity $|E_S|/\hbar$ as the quantum phase-slip frequency, although having in mind that the tunneling is temporally-coherent. In principle, we can add tunneling terms, which mix the next nearest neighbor states $|m\rangle$ and $|m \pm 2\rangle$, and so on, but, for weak tunneling such direct processes are exponentially suppressed.

Extension of the phenomenological picture of tunneling to the case of arbitrary φ_{ext} consists of adding the inductive energy to the H_{tunnel} and summing over all possible m states:

$$H_{\text{array}} = \frac{1}{2} \sum (E_L(2\pi m - \varphi_{\text{ext}})^2 |m\rangle \langle m| + E_S |m\rangle \langle m + 1| + E_S^* |m + 1\rangle \langle m|) \quad (1.13)$$

Here we have introduced $E_L = (\Phi_0/2\pi)^2/L$, the inductive energy of the array. The hamiltonian (1.13) describes how the phase along the array inductance undergoes a reversible twist of phase by 2π , a process usually referred to as coherent quantum phase-slip (CQPS)⁸. From now on, we will refer to the operator m as the quantum phase-slip number operator. The central effect of the CQPS is the non-zero φ_{ext} -dependent matrix element of $\langle \alpha | m | \beta \rangle$ between the eigenstates $|\alpha\rangle$ and $|\beta\rangle$ of the hamiltonian (1.13). The quantum

⁸There is some ambiguity in the literature on whether one should use the singular *phase-slip* or the plural *phase-slips*. We find the singular version, quantum phase-slip, more appropriate, especially in view of using singular term *tunneling* in the analogous phenomenon of the *Cooper pair tunneling*.

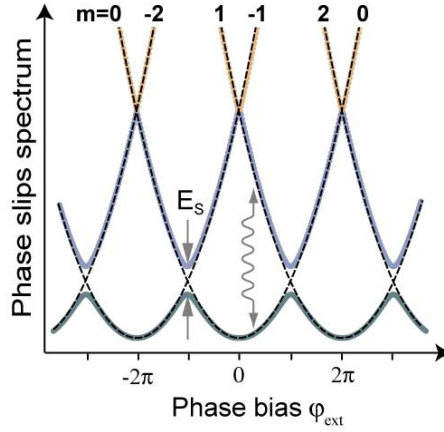


Figure 1-8: Quantum phase-slips spectrum. Colored lines indicate ground $|g\rangle$, first excited $|e\rangle$, and second excited $|f\rangle$ states. Dashed lines indicated the spectrum for $E_S = 0$. The splitting between nearest neighbor parabolas at $\varphi_{\text{ext}} = \pi$ is given by $|E_S|$, the splitting between the next nearest neighbor parabolas at $\varphi_{\text{ext}} = 0$ is given by $\pi^2|E_S|^2/2E_L \ll |E_S|$.

phase-slip hamiltonian is analogous to the hamiltonian of the Cooper pair box, if we replace m with the Cooper pair number operator; $\varphi_{\text{ext}}/2\pi$ with the dimensionless offset charge; $2\pi^2E_L$ with the single electron charging energy; and, finally, E_S with the Josephson energy of the Cooper pair box junction [35]. Therefore, the quantitative consequences of this hamiltonian are readily available from the corresponding works on the Cooper pair box device.

Assuming the case of weak quantum phase-slip, $|E_S| \ll E_L$, the quantum dynamics of the array could be summarized by the way it behaves in three kinds of experimental situations. In the first, under an adiabatic sweep of φ_{ext} the array remains in the ground state $|g\rangle$ by experiencing the m -th 2π phase-twist each time φ_{ext} passes through the value $(2m-1)\pi$ corresponding to the minimum energy gap $|E_S|$. The process, is fully reversible as one inverts the sweep direction. This is the ‘‘Silly Putty’’ effect, the array inductance remains in its true quantum ground state at the expense of completely losing its superconducting phase-rigidity at $\varphi_{\text{ext}} = \pi$. In the second experiment, under non-adiabatic variation of φ_{ext} , due to Landau-Zener tunneling [39], the system starting in the ground state at $\varphi_{\text{ext}} = 0$ undergoes a transition to the first excited state when $\varphi_{\text{ext}} \simeq \pi$, thus effectively preventing the array from undergoing phase-twists. The characteristic rate of sweep, at

which the Landau-Zener tunneling turns on is given by $|\dot{\varphi}_{\text{ext}}| \sim \frac{1}{\hbar}|E_S|^2/E_L$. In the third experiment, we irradiate the array with a harmonic electromagnetic signal of the form $\varphi_{\text{ext}}(t) = \varphi_{\text{ext}} + \delta\varphi_{\text{ext}} \cos \omega t$, with $\delta\varphi_{\text{ext}} \ll \pi$. When the frequency of the irradiation $\omega/2\pi$ matches the transition from ground to the first excited state $\nu_{ge}(\varphi_{\text{ext}})$, the quantum phase-slip number m undergoes Rabi oscillations. The most intense oscillations occur between classically degenerate states, because there the matrix element of m takes the largest values (see also discussion in the matrix element discussion in chapter 3). For instance, $\langle e | m | g \rangle = 1/2$ between ground $|g\rangle$ and first $|e\rangle$ at $\varphi_{\text{ext}} = \pi$ and $\nu_{ge} = \frac{1}{\hbar}|E_S|$, or $\langle g | m | f \rangle = 1$ between $|g\rangle$ and the second excited state $|f\rangle$ at $\varphi_{\text{ext}} = 0$ and $\nu_{ef} = \frac{1}{\hbar}\pi^2|E_S|^2/2E_L$, where $\langle g | m | f \rangle = 1$. Coherent oscillations are poorly coupled to the radiation for flux biases between the degeneracy points, $0 < \varphi_{\text{ext}} < \pi$, because the quantum phase-slip number m is nearly conserved. It is worth noting that during one Rabi oscillation the array exchanges the number of flux quanta with the number of microwave photons in the drive, one flux quantum per photon for the $g \leftrightarrow e$ transition and two flux quanta per photon for the $g \leftrightarrow f$ transition.

Quite remarkably, the seemingly complicated physics of strongly coupled non-linear Josephson oscillators reduces at low energies to that of an inductance with a single internal degree of freedom m . The collective nature of this “many-body” system of junctions hides in the properties of the amplitude E_S . To gain further insight into the phase-slip phenomenon, we next turn to the “microscopic” analysis of E_S .

1.2.3 Offset charges and Aharonov-Casher interference

Evaluating E_S presents to us the problem of finding the tunneling splitting between a pair of classically degenerate states of a multi-coordinate system. In the semiclassical approximation, where the charging energy is sufficiently small, we can evaluate E_S using the instanton technique, a generalization of the WKB approximation [40]. In this technique, we need to consider classical motion of our system in the θ -space and imaginary time $t = i\tau$. Specifically, the energy splitting is given by the following path integral [41]:

$$E_S \propto \int_{x(\tau): m \rightarrow m+1} \mathcal{D}[\vec{\theta}(\tau)] \exp(-S[\vec{\theta}(\tau)]/\hbar) \quad (1.14)$$

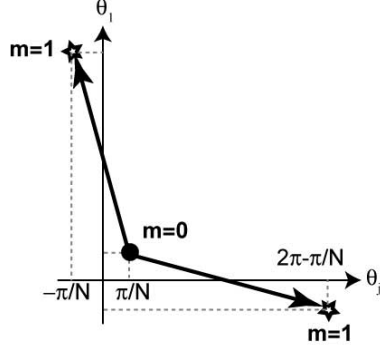


Figure 1-9: Example of two tunneling trajectories. Crosssection of the θ -space defined by a hyperplane $\theta_{i \neq 0}, j = 0$. The initial state is indicated with a solid circle, the final state has two physically equivalent locations in the θ -space, marked with the stars.

where the vector $\vec{\theta}(\tau) = \{\theta_1(\tau), \theta_2(\tau), \dots, \theta_N(\tau)\}$ spans all the possible trajectories in the θ -space which begin at the state $m = 0$ and end at the state $m = 1$ with zero speed (Fig. 1-9); imaginary time action of every trajectory is given by the corresponding integration of the lagrangian $S[\vec{\theta}(\tau)] = \int_{-\infty}^{+\infty} d\tau \mathcal{L}[\vec{\theta}(\tau)]$. The path integral (1.14) should be normalized in such way as to produce units of energy. Fortunately, we will be able to avoid figuring out the proper normalization of the path integral and instead extract E_S using simple physical considerations.

Let us make three observations about the structure of the path integral, which considerably simplify our analysis. First, only extremal trajectories contribute to the integral. Interestingly, imaginary time extremal trajectories for the action $S[\vec{\theta}(\tau)]$ coincide with the real-time extremal trajectories for a different, the so-called euclidean action $S_{\text{euclid}}[\vec{\theta}(t)]$, which corresponds to the motion in an inverted Josephson potential [40]. Such trajectories are dubbed instantons. Second, since the state $m = 1$ corresponds to N distinct locations in the θ -space, there are N extremal trajectories which contribute to the 2π phase-twist. Namely, a phase-slip across the j -th junction corresponds to a trajectory (the j -th trajectory) which starts at the point $\vec{\theta}^{\{j;m=0\}} = \pi\{\frac{L_1}{L}, \frac{L_2}{L}, \dots, \frac{L_j}{L}, \dots, \frac{L_N}{L}\}$ at $\tau = -\infty$ and ends at $\vec{\theta}^{\{j;m=1\}} = -\pi\{\frac{L_1}{L}, \frac{L_2}{L}, \dots, -2 + \frac{L_j}{L}, \dots, \frac{L_N}{L}\}$ when $\tau = +\infty$ and yields the action S_j (Fig. 1-9). Therefore, the complicated path integral (1.14) reduces to the sum

$$\begin{aligned}
E_S &= \sum E_{S_j} \\
E_{S_j} &\propto \exp(-S_j)
\end{aligned}
\tag{1.15}$$

The third observation is that along each trajectory only one junction undergoes a large (approximately 2π) phase change, the rest of the junctions experience only $O(1/N)$ phase change. Therefore, for evaluating the action S_j along the j -th trajectory we can linearize all “cos” terms except for the j -th junction (still verifying the boundary condition). In doing so, we notice that the resulting lagrangian \mathcal{L}_j describes a simple circuit where a loop with inductance $L - L_j$ is pierced with the flux $\frac{1}{2}\Phi_0$ and is interrupted with the j -th Josephson junction. Now its evident that $|E_{S_j}|$ is nothing else than the ground state splitting in the double-well potential $U(\theta_j) = E_{J_j} \cos(\theta_j) + \frac{1}{2}\Phi_0^2/(L - L_j)$ (Fig. 1-10). Computing the splitting in such one-dimensional problem can be done numerically. In the situation, where $L_j \ll L$, and $E_{S_j} \ll E_L$, the quadratic term does not contribute much to the action, and the tunneling through the “cos” potential can be calculated exactly⁹:

$$|E_{S_j}| = \sqrt{2/\pi}^4 \sqrt{\frac{8E_{J_j}}{E_{C_j}}} \sqrt{8E_{J_j}E_{C_j}} \exp - \sqrt{\frac{8E_{J_j}}{E_{C_j}}}
\tag{1.16}$$

To connect this expression to the language of junction impedance $Z_{J_j} = \sqrt{L_{J_j}/C_{J_j}}$ and the plasma frequency $\omega_p = 1/\sqrt{L_{J_j}C_{J_j}}$, we can rewrite this expression as

$$|E_{S_j}| = \hbar\omega_p \times \frac{4}{\sqrt{\pi}} \sqrt{\frac{R_Q/2\pi}{Z_J}} \exp - \left(8 \frac{R_Q/2\pi}{Z_J} \right)
\tag{1.17}$$

Our calculation is valid as long as the number of junctions N is sufficiently large to insure the linearization and as long as the effective double-well tunneling problem is the WKB limit.

What about the phase of E_{S_j} ? Although the third term in the lagrangian (1.9) indeed

⁹Note that the expression above uncoincidentally matches exactly with the so-called charge dispersion amplitude of a transmon qubit

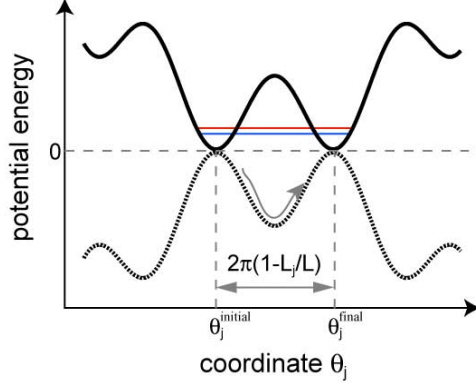


Figure 1-10: Effective tunneling potential. Solid line indicates the effective potential felt by the θ_j -th junction, if the other junction acted as linear inductances, $\varphi_{\text{ext}} = \pi$. Colored lines indicate the energy-splitting classical ground state. The tunneling splitting is given by the action for the inverted potential (dotted curve), with the corresponding instanton trajectory which starts at $\theta_j^{\text{initial}}$ with zero velocity and stops at θ_j^{final} also at zero velocity.

does not contribute to the classical trajectories, it does add a purely imaginary geometric phase contribution to the imaginary time action, given by (along the j -th trajectory)

$$\delta S_j^{\text{geometric}} = (\Phi_0/2\pi) \int d\tau \sum_{k=1}^N d\theta_k^{\{j\}}/di\tau \times \sum_{i=k}^N q_i = -i(\Phi_0/2\pi) \sum_{k=1}^N (\theta_k^{\{j;m=0\}} - \theta_k^{\{j;m=1\}}) \times \sum_{i=k}^N q_i.$$

Given that $\theta_k^{\{j;m=0\}} - \theta_k^{\{j;m=1\}} = (2\pi\delta_{kj} - 2\pi L_k/L)$, we arrive at a simple result

$$\delta S_j^{\text{geometric}} = -i\Phi_0 \sum_{i=j}^N q_i + \text{const.} \quad (1.18)$$

where the constant does not depend on the phase-slip trajectory index j . Thus, taking into account the offset charges we arrive at the final expression for the phase-slip amplitude

$$E_S = \sum E_{S_j} \exp\left(i\frac{Q_j}{2e}2\pi\right) \quad (1.19)$$

where, the $Q_j = q_1 + q_2 + \dots + q_{j-1}$ is the total offset charge located between the first and the j -th junctions (up to an overall phase factor).

Expression (1.19) for the total CQPS amplitude E_S may be illustrated with the following physical picture of the quantum phase-slip process (Fig. 1-11). One can view each quantum phase-slip event as tunneling of a fictitious particle carrying flux Φ_0 from the inside of the loop to the outside (and vice-versa). Tunneling occurs via a superposition of multiple paths

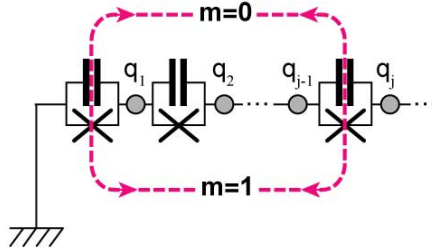


Figure 1-11: Aharonov-Casher type interference of quantum phase-slip. A section of the array with first j junction is shown. Dashed line indicate two interfering trajectories involving a phase-slip across the 1-st and the j -th junctions. Interference of quantum phase-slip amplitudes across those two junctions is controlled by the enclosed offset charge of the first $j - 1$ islands.

crossing different junctions and therefore encircle island charges. Tunneling through each individual junction j then contributes to the total CQPS amplitude with the corresponding Aharonov-Casher [38, 42] geometric phase $2\pi Q_j/2e$.

1.2.4 Coherence of the quantum phase-slip process

The expression (1.19) also shows that the analogy between the coherent quantum phase-slip and the Cooper pair tunneling extends beyond the hamiltonian (1.13). The former phenomenon transfers flux across the array, the latter one transfers charge through the oxide of the junction. The Josephson energy in the presence of external flux is given by the expression very similar to Eq. (1.19). Namely, $E_J = \sum_j E_{J_j} \exp(2\pi\Phi_j/\Phi_0)$, where E_{J_j} is the Josephson energy of the j -th microscopic weak spot in the oxide, Φ_j is the Aharonov-Bohm flux enclosed by the first and the $j + 1$ trajectories, $\Phi_j = \phi_0 + \phi_1 + \dots + \phi_j$ (Fig. 1-12).

Despite this obvious analogy between CQPS and Cooper pair tunneling, we emphasize here that, contrary to the essentially microscopic Cooper pair tunneling, the CQPS phenomenon involves simultaneously three types of coherence. The first type (i) is the usual BCS coherence of electrons forming the Cooper pair condensate and eventually responsible for the formation of the circuit degrees of freedom θ_j ; in experiment it manifests itself as superconducting order inside the islands. The second type (ii) is the temporal quantum coherence of the circuit degrees of freedom associated with the reversibility of the tunneling in the θ -space; this effect we see for instance as the energy splitting in the spectrum of the

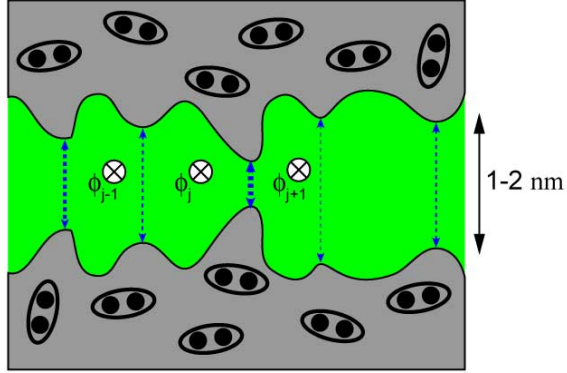


Figure 1-12: Aharonov-Bohm type interference of Cooper pair tunneling. Gray regions represent superconducting electrodes of a Josephson tunnel junction, green region represent the oxide. Due to the roughness of the interface, the tunneling takes place via discrete weak links (blue dashed lines). Josephson tunneling amplitudes for the Cooper pair trajectories interfere in real space, with the interference phase controlled by the total external magnetic flux which those two trajectories enclose.

array at $\varphi_{\text{ext}} = \pi$. Finally, the third type (iii) is the spatial coherence between the junctions located physically apart from each other and manifested in the Aharonov-Casher type sensitivity of the CQPS amplitude on the charges residing between the junctions. This type of coherence is certainly absent in a Cooper-pair box device. Here we deal with the coherence among a large number of circuits elements – objects, which are already macroscopic.

1.2.5 Energy dissipation

It is often suggested that the quantum phase-slip process results in a finite resistance of a superconducting wire at a vanishing temperature (see Ref. [2] for a review and Ref. [43]). Here, we would like to explain how dissipation enters our description of the CQPS process in the Josephson junction array. Indeed, whenever the quantum phase-slip number operator m couples to a dissipative bath, the quantum phase-slip event is accompanied by energy dissipation. This results in a finite lifetime of the excited state of the hamiltonian (1.13). Here we consider the simplest possible scenario of dissipation provided by coupling an external circuit (Fig. 1-13). In this model, a superconducting loop with inductance L , which also undergoes CQPS with amplitude E_S , is coupled via a mutual inductance M to another, lossy loop. The lossy loop is modelled as an inductance in series with a resistance

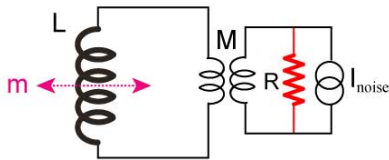


Figure 1-13: Coupling of CQPS to dissipation. An inductance L , which is subject to CQPS, is coupled inductively via a mutual inductance M to a dissipative loop. Dissipation in that loop comes from resistance R . It generates quantum noise represented by a current source I_{noise} .

R . In actual experiment the lossy loop model applies to the external flux bias circuitry, or to the normal-metal walls of the sample holder.

Note that, classically, a DC current in our superconducting loop experiences no dissipation. Indeed, DC current generates no voltage across the second loop inductance and therefore does not dissipate energy in the resistance R . Quantum mechanically, however, there is never a truly DC current in the loop in a stationary state. Quantum phase-slip processes mix the true persistent current states which correspond to the fixed quantum phase-slip number m . To reestablish the classical intuition, one can think that the quantum phase-slip across the array results in a voltage pulse across the coupling inductance. The time integral of this pulse would be the fraction of the flux quantum, $(M/L)\Phi_0$. The time-dependent voltage drives the resistor in the lossy loop and hence the power is dissipated.

To obtain the expression for the dissipation rate, we need to replace φ_{ext} in the hamiltonian (1.13) with $\varphi_{\text{ext}} + \varphi_{\text{noise}}$, where φ_{noise} is the operator of quantum noise in phase across the coupling inductance. Given that $\varphi_{\text{noise}} = 2\pi(I_{\text{noise}}M)/\Phi_0$, and assuming that $M/L \ll 1$ we can treat the effect of dissipation perturbatively, using the following perturbation operator V :

$$V = E_L(m \times \varphi_{\text{noise}}) = \frac{M \Phi_0}{L} \frac{1}{2\pi} (m \times I_{\text{noise}}) \quad (1.20)$$

Fermi's golden rule¹⁰ then results in the following expression for the transition rate $\Gamma_{\alpha\beta}$

¹⁰In general, when an atomic operator A is coupled to a reservoir operator B , the transition rate between higher energy state α and lower energy state β is given by the expression $\Gamma_{\alpha\beta} = \frac{1}{\hbar^2} |\langle \alpha | A | \beta \rangle|^2 S_B(\omega_{\alpha\beta})$.

between the states α and β of the hamiltonian (1.13):

$$\Gamma_{\alpha\beta} = 2 \left(\frac{M}{L} \right)^2 \frac{R_Q}{R} |\langle \alpha | m | \beta \rangle|^2 \omega_{\alpha\beta} \quad (1.21)$$

This expression emphasizes the central role of the matrix element of m in the finite lifetime of the eigenstates of the quantum phase-slip hamiltonian. The relaxation of the first excited state is most pronounced at $\varphi_{\text{ext}} = \pi$, where the states with $m = 0$ and $m = 1$ are maximally mixed and the matrix element $\langle g | m | e \rangle$ takes its maximum value of unity.

Here we abandon the question of internal dissipation in the junctions of the array. The general problem of intrinsic dissipation in the junctions of the array makes the problem of finding the relaxation rate somewhat trickier. This is because the intrinsic dissipation in the j -th junction couples to its phase θ_j rather than to the collective variable m as in the case considered above. Fortunately, for the case of the fluxonium circuit, considered below, we will be able to take into account internal dissipation without cumbersome microscopic calculations.

1.3 Testing superinductance with fluxonium

How can one test if a given circuit element is a superinductance? How can we measure if it indeed undergoes quantum phase-slip? How can we evaluate experimentally the internal dissipation in the superinductance? Our key idea is to test a large-value inductance by making it a part of a specially designed superconducting qubit, fluxonium [3, 45]. The transition spectrum of this qubit is linked strongly to the broadband value of the inductance. Somewhat less intuitively, the dephasing time of the qubit transitions carries information on the quantum phase-slip frequency.

Circuit with a “slippery” inductance

The fluxonium artificial atom is presented in Fig. 1-14. On the one hand, it is an array of $N + 1$ junctions, where the dominant contribution to the quantum phase-slip amplitude is

Here $\omega_{\alpha\beta}$ is the positive-valued frequency of the $\alpha \leftrightarrow \beta$ transition, $S_B(\omega_{\alpha\beta})$ is the spectral density of the quantum noise of the quantity B , defined as $\int dt e^{i\omega_{\alpha\beta}t} \langle B(t)B(0) \rangle$, where the averaging is taken over the ground state of the reservoir. See Ref. ([44])

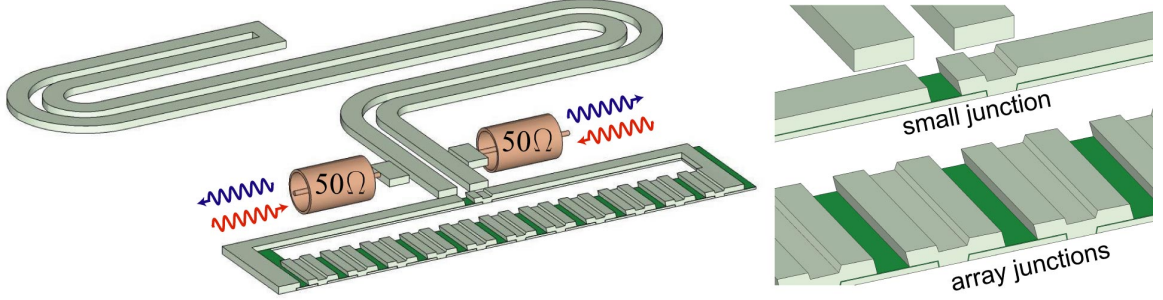


Figure 1-14: Sketch of fluxonium qubit and its readout. Josephson array is turned into a loop by shunting the small area “black-sheep” junction. Gray indicates superconducting aluminum electrodes, green indicates tunneling oxide. Black-sheep junction electrodes are coupled capacitively to the coplanar strips transmission line resonator with a short-circuit termination at the far end. The device is connected to the readout and control electronics by a pair of transmission lines (indicated with brown colored coaxials).

provided by a single “black-sheep” junction (Fig. 1-15). The black-sheep junction has the Josephson energy E_J and charging energy E_C . The qubit state is monitored dispersively, in a circuit QED fashion [46], by coupling capacitively the charge of the black-sheep junction to the electric field of a nearby coplanar resonator (Fig. 1-14). This “array-with-a-black-sheep” view point is best suited for the qualitative understanding of the device. The total CQPS amplitude is now given by $E_S^\Sigma = E_{SB} + E_S$, where E_{SB} is the quantum phase-slip amplitude in the black-sheep junction, while E_S is that in the array. The inductive energy E_L is slightly renormalized to the value $E_L^\Sigma = (E_L^{-1} + E_J^{-1})^{-1} \simeq E_L$. Essentially, we have separated the roles of the array junctions and the black-sheep junction. The array junctions stores the energy associated with the phase-slip in the fluxonium loop, while the black-sheep provides the quantum-mechanical amplitude for this event. Let us discuss below some of the key properties of fluxonium which follow immediately from this model.

On the other hand, fluxonium may be viewed as a Cooper-pair box type junction in the charge regime which is shunted by a superconducting wire comprised of N junctions in the phase regime. This wire is a circuit element, which is characterized not only by its N -junction linear inductance L , but also by the CQPS energy amplitude E_S , where both quantities L and E_S are independent on the details of the embedding circuit, which is fair in the limit of large N . The hamiltonian of such circuit element under a phase-bias is given by Eq. (1.13); for convenience we nickname such circuit element “slippery” inductance

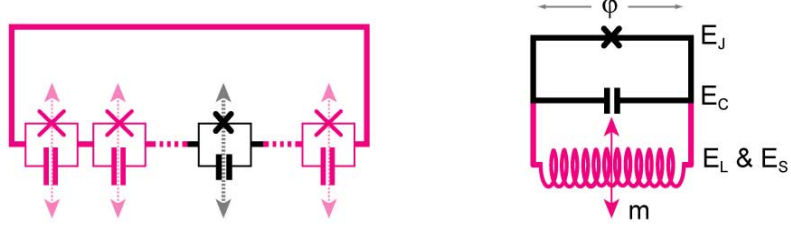


Figure 1-15: Two models of fluxonium circuit. (A). Array of $N + 1$ junction, in which one of them, the black-sheep, is weaker than other. This model contains only one degree of freedom, the total number of phase-slips in the fluxonium loop (B). Junction shunted by a “slippery” inductance of the array of N junctions. This model contains two variables, phase φ across the black-sheep junction and m , the total number of phase-slips in the array.

and indicate it on circuit diagrams with a conventional inductance pictogram but with an additional crossing arrow (Fig. 1-15).

Broadband inductance measurement.

The lowest energy transitions of fluxonium are given by the familiar hamiltonian (1.13). Away from the half flux quantum bias point, the ground to first-excited transition frequency ν_{ge} is given by the expression $\nu_{ge}(\varphi_{\text{ext}}) = \frac{1}{h}(2\pi)^2 E_L^\Sigma |1/2 - (\varphi_{\text{ext}} \bmod 2\pi)/2\pi|$. The function $\nu_{ge}(\varphi_{\text{ext}})$ takes the shape of a zigzag (Fig. 1-16). This zigzag shaped transition frequency is a characteristic feature of the fluxonium spectrum¹¹. Its low-frequency corners are rounded by the quantum phase-slip via the main, black-sheep junction, rendering the minimum transition frequency to be $|E_{SB}|$. Therefore, measuring the excitation spectrum of the fluxonium loop tells us the value of the inductance L in the range of frequencies starting as low as $|E_{SB}|/h$ and reaching as high as $2\pi^2 E_L^\Sigma/h$. Note that since we are aiming at the inductance value $L \gtrsim R_Q/\omega_p$, and given that $\omega_p \simeq 10 - 20$ GHz, the zigzag amplitude $2\pi^2 E_L^\Sigma/h$ is also of order 10 GHz. Thus, fluxonium spectrum spans the entire microwave frequency range of interest to the superinductance operation.

¹¹A zigzag spectrum is also expected from a Cooper-pair box device for $E_J/E_C \ll 1$. However, the transition frequency value at zero offset charge, given by $4E_C$, takes a value too large to measure. Indeed, the plasma frequency of typical Al-based junction is typically constrained to be $\sqrt{8E_J E_C} > 10 \text{ GHz} \times h$. Hence, $4E_C \gg 15 \text{ GHz}$, which lies not only above the measurable frequency range, but also may simply exceed 2Δ of Al. In addition, close to zero offset charge, the dispersive shift due to this transition becomes extremely weak (see Eqs. 3.7, 3.9, and 3.17), which is not a limitation for fluxonium.

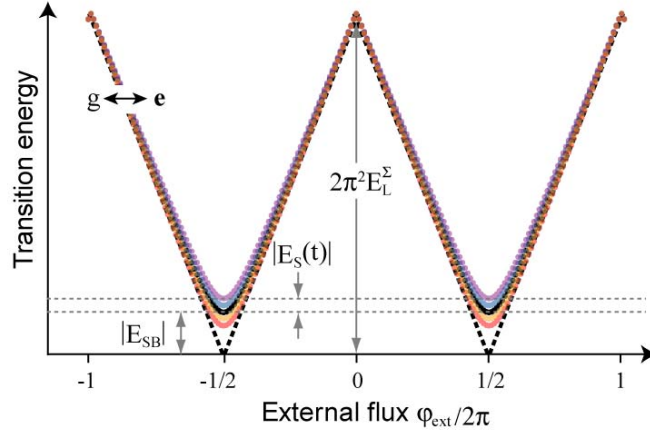


Figure 1-16: Simplest model of fluxonium spectrum. Black line indicates the transition spectrum when $E_S = 0$. Finite E_S interferes constructively or destructively with the main CQPS amplitude E_{SB} depending on the exact configuration of charges (colored lines). Fluctuating offset charges thus broaden the fluxonium ground to first excited state transition, when measured sufficiently slowly.

Sensitivity to low-energy CQPS in the array.

Aharonov-Casher interference causes E_S to depend on the offset charges on the array islands. These charges tend to experience e -jumps due to parity fluctuations [47]. This makes E_S fluctuate in time, causing the broadening of the $e \leftrightarrow g$ transition in a slow experiment. The maximum broadening takes place at the half flux quantum (flux) sweet-spots, i.e. $\varphi_{\text{ext}} = \pm\pi$, etc. Therefore, the effect of CQPS can be resolved in a slow measurement of dephasing of the fluxonium transitions, provided that the intrinsic linewidth is smaller than $|E_S|/h$. Let us note that increasing E_S might not be a great strategy here at all: large $|E_S|$ means large fluctuations of the qubit transition frequency at $\varphi_{\text{ext}} = \pi$, which will make frequency measurement difficult. It is much easier experimentally to monitor small fluctuations around a well defined mean frequency.

Low intrinsic decoherence.

As far as energy relaxation is concerned, one can think that every junction in the fluxonium is coupled to a dissipative bath, presumably related to the imperfections in the junction materials, or really, any other reason. Since the quantum phase-slip predominantly takes

place via the black-sheep junction, the AC voltage across an array junction, associated with an excited state to ground state transition, is a factor $1/N$ smaller than that across the black-sheep junction. Therefore, assuming that the black-sheep junction is not too different in dimensions from the array junctions, the dissipation via the black-sheep junction dominates the life-time of the fluxonium excited state. Thus, the large number of junctions involved in storing the qubit transition energy should not scale up the intrinsic relaxation rate (see also discussion around Eq. (3.37)).

Furthermore, decoherence due to flux noise is suppressed even away from the flux sweet-spots by the unusually large loop inductance L (see discussion around Eq. (3.39)). For instance, since the ground to first excited state of fluxonium is roughly given by $\nu_{ge}(\varphi_{\text{ext}}) = \frac{1}{\hbar}(2\pi)^2 E_L^\Sigma |1/2 - (\varphi_{\text{ext}} \bmod 2\pi)/2\pi|$, it is clear that the larger L , the smaller the flux sensitivity. For instance our inductance is larger than that used in flux or phase qubits by a factor of order 100. Thus, armed with fluxonium circuit, we are in a position to study the flux-dependence of the CQPS + offset charge noise induced dephasing, without having to worry (to some extent) about the $1/f$ flux noise [48].

Quantitative model of fluxonium

The “inductively shunted Cooper pair box” viewpoint of the fluxonium qubit is convenient to treat the problem quantitatively. In this model we deal with a circuit with two degrees of freedom: the phase φ across the black-sheep junction and the number m of quantum phase-slip in the slippery inductance. Introducing the black-sheep junction capacitance charge operator¹² $n = -i\partial/\partial\varphi$, the hamiltonian is defined by the two black-sheep junction parameters E_J , the Josephson energy and E_C , the charging energy, as well as two inductance parameters E_L , the inductive energy and E_S , the quantum phase-slip energy:

$$H = -4E_C n^2 - E_J \cos(\varphi) + \frac{1}{2} E_L (\varphi - \varphi_{\text{ext}} - 2\pi m)^2 + \sum_m (E_S |m\rangle \langle m+1| + E_S^* |m+1\rangle \langle m|) \quad (1.22)$$

¹²Here, as discussed around Eq. (1.22), the commutation relation between n and φ is the same as between momentum and position of a harmonic oscillator: $[n, \varphi] = i$.

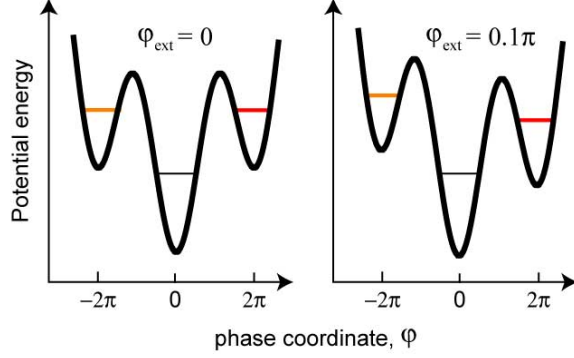


Figure 1-17: Inductively shunted junction model of fluxonium. The effective quantum particle with coordinate φ has on average one quantum level per Josephson well in the RF-SQUID type potential.

The effect of CQPS in the array inductance can clearly be treated perturbatively, provided that $|E_S|$ is sufficiently small. In fact, the true condition would be that $|E_S|$ must be smaller than the smallest frequency in the problem, which is the $g \leftrightarrow e$ transition at $\varphi_{\text{ext}} = \pi$, given by approximately $\hbar\omega_p \exp(-\sqrt{8E_J/E_C})$. This condition is automatically satisfied as precisely the condition for “black-sheepness” of the small junction. Furthermore, since we know that $E_S = E_S(t)$ fluctuates randomly in time, the coupling to CQPS again results in the broadening of the fluxonium qubit transitions. We therefore can first neglect the CQPS effect in the array, solve numerically for all transitions of the fluxonium circuit, fully taking into account the large quantum fluctuations of phase in the black-sheep junction, and then include CQPS perturbatively. Moreover, the hamiltonian (1.22) is well suited for treating the coupling to the readout resonator by adding the term

$$H_{\text{readout}} = \hbar\omega_0 a^\dagger a + g(a + a^\dagger)n \quad (1.23)$$

The coupling (1.23) of the qubit to the cavity readout is somewhat unconventional: usually loop-based qubits are coupled to resonators inductively. In our scheme, on the contrary, the black sheep junction charge operator $2en$ is coupled capacitively to the cavity voltage operator $\frac{g}{2e}(a + a^\dagger)$. The magic of this coupling scheme in the case of fluxonium will be explained in detail in chapter 3 of this thesis.

Fluxonium vs flux qubit

The hamiltonian (1.22) in the limit of $E_S = 0$ represents motion of a quantum particle in a potential, with parameters $\beta_L = L/L_J \gg 1$ and $E_J/E_C \sim 1 - 10$. Note that even though there can be as much as Φ_0 of flux in the loop inductance of fluxonium, the magnetic fraction of this flux is always only a tiny fraction of Φ_0 , approximately equal to $L_{\text{geometric}}/L$, where $L_{\text{geometric}}$ is the geometric (not kinetic) inductance of the loop. Although fluxonium circuit reminds that of a flux qubit, its typical parameters make it considerably different. Indeed, the three junction flux qubit [49], corresponds to parameter regime $\beta_L \gtrsim 1$ and $E_J/E_C \gtrsim 10$. Qualitatively, the fluxonium qubit regime may be defined approximately as such that the particle has only one (may be two at most) bound state per Josephson well. We call such bound states “fluxons”, because in each state the loop is charged with approximately an integer times the flux quantum Φ_0 , provided that $\beta_L \gg 1$. Hence the choice of name for our qubit – “fluxon-ium”. On the contrary, typical flux qubit parameters are such that the bound states exist only for φ_{ext} very close to π . Perhaps it is fair to say that from the point of view of a theorist, flux qubit and fluxonium close to $\varphi_{\text{ext}} = \pi$ are essentially indistinguishable. However, the number of important practical differences, for instance the rich spectrum around $\varphi_{\text{ext}} = 0$ (see Fig. 1-18), certainly call for a separate name.

Finally, let us note that although the hamiltonian (1.22) involves a junction with small parameter $E_J/E_C \sim 1$, unlike the Cooper pair box device, it is completely insensitive to the external DC electric field, provided that $E_S = 0$. The large inductance of the array, provided that it is indeed a linear inductance, completely shunts the offset charges of the black-sheep junction, without killing the charging effects physics.

1.3.1 Overview of main results

Measurement of the spectrum of excitation of the fluxonium circuits as well as the time-domain coherence of fluxonium states adds a new superconducting qubit to the line of previously established ones: Cooper-pair box [17], quantronium [18], flux qubit [49], phase qubit [50], and transmon qubit [51]. In chapter two we describe the details of our experiment: device fabrication, instrumentation and measurement. The spectrum (Fig. 1-18) is measured

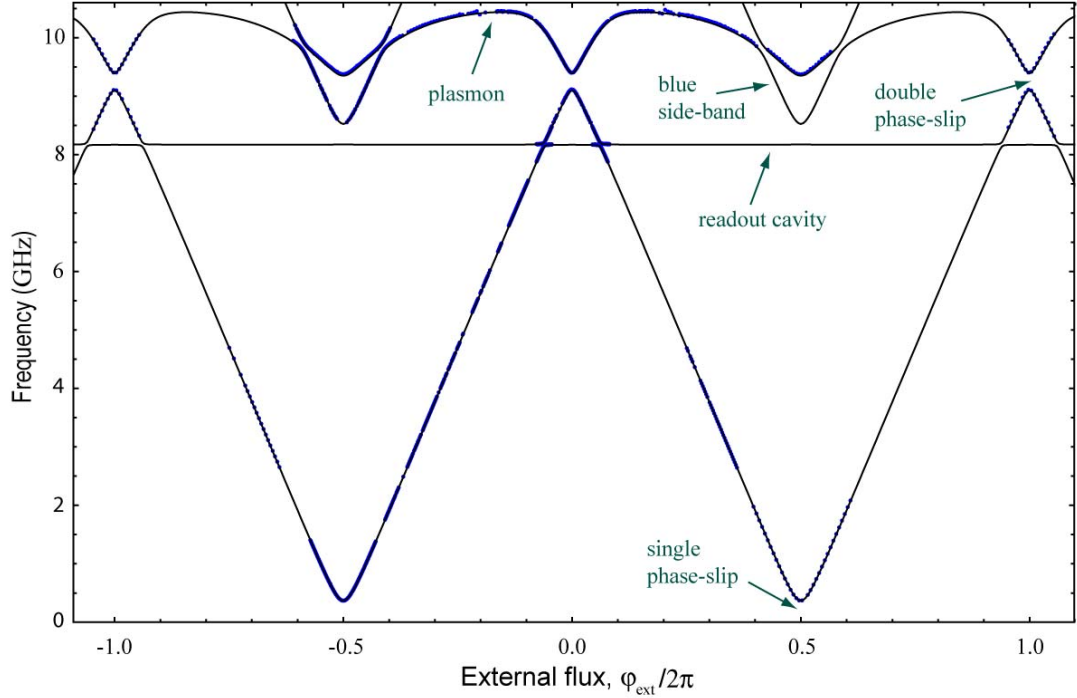


Figure 1-18: Fluxonium circuit spectrum. Blue dots: experimentally measured spectroscopic resonances location as a function of applied external flux. Black-lines: theory. The “double” phase-slip splitting corresponds to the between next nearest neighbor fluxon wells (see Fig. 1-19).

for the entire range of possible flux bias and in the frequency range from 300 MHz to over 12 GHz. The transition spectrum (1-18) reveals all expected feature of fluxonium: the zigzag $g \rightarrow e$ transition, the splitting of 370 MHz due to single phase-slip in the black-sheep ($\varphi_{\text{ext}} = \pi$) and even double phase-slip ($\varphi_{\text{ext}} = 0$), the black-sheep junction plasma mode at around 10 GHz, as well as strong coupling of fluxonium transitions to the readout resonator frequency [19]. Quantitatively, transitions are in perfect agreement with the theory based on the hamiltonian (1.22) with the inclusion of the interaction with the readout resonator (1.23) and some minor effects, discussed in Chapter 3.

Based on the agreement between theory and experiment, we have extracted the inductive energy of the circuit $E_L = (0.52 \pm 0.01)$ GHz which translates into the total inductance of the array $L = 310$ nH, as well as other parameters of the circuit. Numerically calculated wavefunctions of the eigenstates of the hamiltonian (1.22) are calculated for the case of

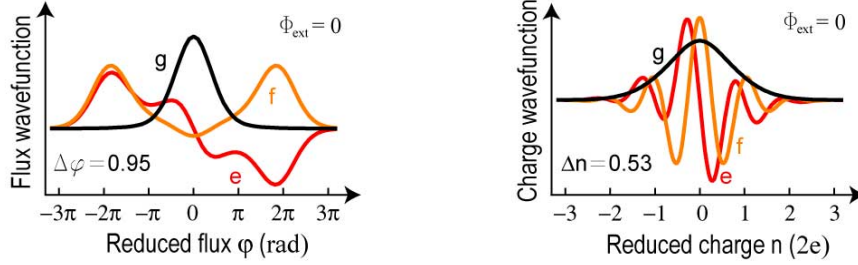


Figure 1-19: Superinductance regime with fluxonium. Numerically calculated wavefunctions of the fluxonium device for the ground (black), first excited (red), and second-excited (yellow) states at zero external flux. The ground state wave-function is approximately that of a harmonic oscillator with impedance exceeding impedance quantum.

$\varphi_{\text{ext}} = 0$ and plotted in Fig. 1-19. The ground state corresponds to a vibrating mode in the Josephson potential of the black-sheep junction and is essentially indistinguishable from the gaussian wave-function of the ground state of the harmonic oscillator, like that in Fig. 1-1. The calculated ground state excursion of the phase $\delta\varphi$ is found to be $\delta\varphi = 0.95$ rad and the excursion of the conjugate charge is $\delta n = 0.53$. These numbers prove that fluxonium is the first circuit which reached the sub-Cooper-pair level of charge fluctuations without being sensitive to external electric fields, at least at the level of $1 - 0.1\%$ precision of the spectroscopic measurement.

We have fabricated and measured a single fluxonium device with properly chosen parameters, all summarized in the Table 1. More devices were tested after the completion of this work and proved to be fully consistent with our conclusions (data for the new devices will not be discussed here).

As a main result, we have measured the excitation spectrum of the fluxonium device and compared the dependence of the transition frequency on the external flux with the theoretical predictions based on the $E_S = 0$ version of the hamiltonian (1.22). After taking into account the interaction of the fluxonium atom with the readout resonator we have established that the spectrum is in perfect agreement with theory.

Taking into account the small effect of CQPS in the inductance using first order perturbation theory, we found that the correction to the transition between states α and β is given by the following expression:

$$\delta E_{\alpha\beta} = \text{Re}[E_S] \left| \int d\varphi \Psi_\beta(\varphi) \Psi_\beta(\varphi - 2\pi) - \int d\varphi \Psi_\alpha(\varphi) \Psi_\alpha(\varphi - 2\pi) \right| \quad (1.24)$$

The overlap integrals depend very strongly on fluxonium parameters and on the external flux. Therefore the effect of CQPS on the transition spectrum is flux-dependent. The flux dependence for the first, $g \rightarrow e$ transition can be qualitatively seen from the Fig. (1-16): the correction $\delta E_{\alpha\beta}$ is maximum at $\varphi_{\text{ext}} = \pi$ and vanishes towards $\varphi_{\text{ext}} = 0$. For fluctuating $E_S = E_S(t)$, the shift $\delta E_{\alpha\beta}$ turns into linewidth, or, equivalently into the flux-dependent dephasing. This flux dependence allows to distinguish the effect of CQPS from conventional dephasing mechanisms due to $1/f$ noise in every parameter of the hamiltonian (1-16). We found very good agreement between the dephasing measured in a Ramsey experiment and expression (1.24), with only one adjustable parameter - the value of the theoretical dephasing time at $\varphi_{\text{ext}} = 0$. Quite remarkably, the dephasing time starts at about 250 ns at $\varphi_{\text{ext}} = 0$ and increases by an order of magnitude for $\varphi_{\text{ext}} \simeq \pi/2$. Further increase was suppressed due to increased energy relaxation time towards higher transition frequencies. Assuming that E_S fluctuates by an amount comparable to its maximum value, we have extracted that the CQPS amplitude in the array is about $|E_S| \approx 250$ kHz. This is the lower bound on the operation frequency of our superinductance. So far, the effects of quantum phase-slip were only seen in short arrays of weak Josephson junctions as the suppression of the chain's critical current [8, 52]. In continuous superconducting nanowires, the origin of low-temperature resistance was also attributed to the effect of quantum phase-slip [53, 54].

To summarize the key results, we have implemented a superinductance out of a 20 μm array of 43 Josephson tunnel junctions. The inductance value exceeds $L = 300$ nH its operation frequency extends to at least 10 GHz at the higher end, with the product $L\omega > 20$ k $\Omega \simeq 3R_Q$. The operation frequency is also limited from below by the frequency of order a fraction of a MHz due to the residual effect of quantum phase-slip. The energy relaxation quality factor of the fluxonium qubit transition reaches $Q = 150,000$ and is likely to be not limited by the losses in the array. The fluxonium artificial atom appears promising for implementing various experiments in the field of quantum information processing and also for debugging the origins of decoherence in superconducting circuits.

Chapter 2 of this thesis summarizes the key experimental tricks of this work. Chapter

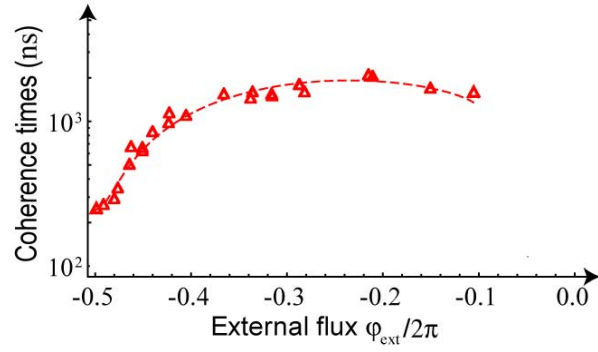


Figure 1-20: Dephasing in fluxonium qubit as the evidence of CQPS in array inductance. Coherence time of $g \leftrightarrow e$ transition measured as the length of the Ramsey fringes, for different values of external flux (markers). Dashed line is theory.

3 theoretically describes the basic concepts of fluxonium circuit. Chapter 4 presents the data and compares it with theory. Chapter 5 concludes the work and discusses future novel experiments with quantum circuits which may be possible with the development of the superinductance.

Chapter 2

Experimental techniques

On the fabrication side, we adopted well established techniques for fabricating small area $Al/AlOx/Al$ junctions [25]. On the measurement side, we have designed our measurement setup based on the past experience with microwaves from the experiments on circuit quantum electrodynamics (cQED) [23] and Josephson bifurcation amplifier (JBA) [55], [24]. Our major innovation here consists of replacing the commonly used coplanar waveguide transmission line resonator (CPW) [56] with the coplanar strips (CPS) [57]. The small areas of metalization in the CPS allowed us to fabricate this structure using e-beam process compatible with the junction fabrication, and therefore to eliminate the optical lithography from the process (see also [58]). We also developed a new type of cryogenic microwave sample holder for launching into CPS resonators at frequencies up to 20 GHz. Below we present some details on the fabrication and measurement, with the emphasis on the differences from past work.

2.1 Nanofabrication

Given the large number N of junctions in the array circuits, naive statistical arguments would predict zero yield in fabrication. Therefore, in our fabrication solutions we reduced the number of fabrication layers to its minimum, namely unity. The optical image of the actual fluxonium device (Fig. 2-1) illustrates our key ideas. The qubit and the readout circuits are fabricated on a Si chip, using Al double-angle evaporation through a suspended

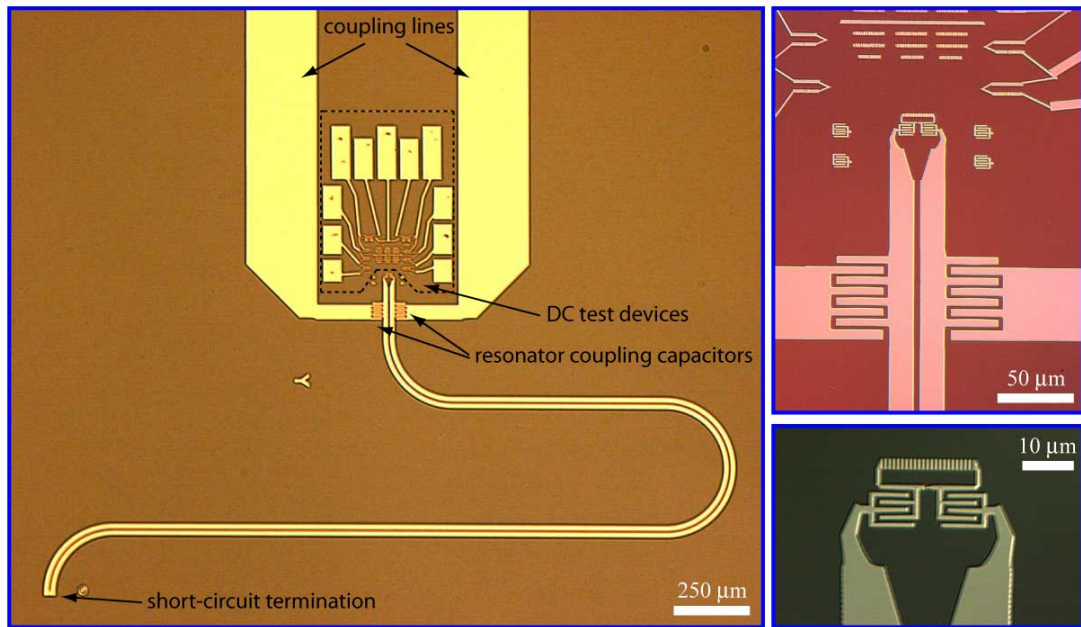


Figure 2-1: Fluxonium optical images. Left: Optical image of the sample (color filters applied for better contrast), bright indicates Al, dark indicates Si substrate. Sample contains the CPS resonator, the qubit, measurement leads and test structures. Top-right: zoom in on the voltage antinode region of the resonator. Bottom-right: further zoom on the fluxonium qubit loop.

electron beam resist mask [59], [25]. The areas of the small junction and array junctions are designed to be $0.2 \times 0.3 \mu\text{m}^2$ and $0.25 \times 2 \mu\text{m}^2$, respectively, thus the areas of small and large junctions are only different by a factor of about 5 (Fig. 2-2). All 43 array junctions are equally spaced at less than 200 nm so that total length of the array is only 20 μm . The loop area of the array-small junction ring is $3 \times 20 \mu\text{m}^2$. The readout part consists of a resonator, implemented with a $\lambda/4$ coplanar-strips (CPS) transmission line, about 2.5 mm in length. The two strips forming the “parallel-wire” type transmission line are short-circuited at one end and at the other end are connected to 50 Ω measurement leads (microstrips) using a pair of interdigitated capacitors. The two leads of the “black-sheep” junction are connected to the resonator strips with another pair of smaller interdigitated capacitors. A number of resistance and dose test structures are fabricated in close proximity to the actual device, in the approximately 500 μm wide space between the resonator coupling lines. Since the fluxonium circuit is disconnected at DC, these test structures were crucial in selecting a device for cooldown.

The Si substrate is 300 μm thick for easy cleaving and with over 9 $\text{k}\Omega \times \text{cm}$ room temperature resistivity for low microwave losses. The Al evaporation and oxidation is conducted in an e-gun evaporator at pressures less than 10^{-5} Pa. The AlOx grown in an environment of 680 Pa of 15% oxygen-in-argon mixture for a period of 10 minutes. We found that the large number of junctions in the array did not affect the fabrication convergence – either all junctions in the array appeared to be good under the SEM imaging and resistance test, or most of them suffered from errors in the lithography. Typical critical current density was on the low side, 100 – 200 $\text{nA}/\mu\text{m}^2$. We also encountered a significant amount of aging in our junctions, with the room-temperature resistance changing by as much as 30% over the course of several days. Devices were therefore aged at ambient conditions for at least one week before cooldown. Details of the e-beam patterning for the fluxonium sample are shown below, the pattern fits into the field of view of 2 mm \times 2 mm at magnification of about 60 and 100 $\mu\text{m} \times 100 \mu\text{m}$ for magnification of about 900. The total e-beam writing time was less than 10 min.

We emphasize that the entire fluxonium device – including the Josephson array, the black-sheep junction, the resonator, and the test structures – is fabricated in a single step

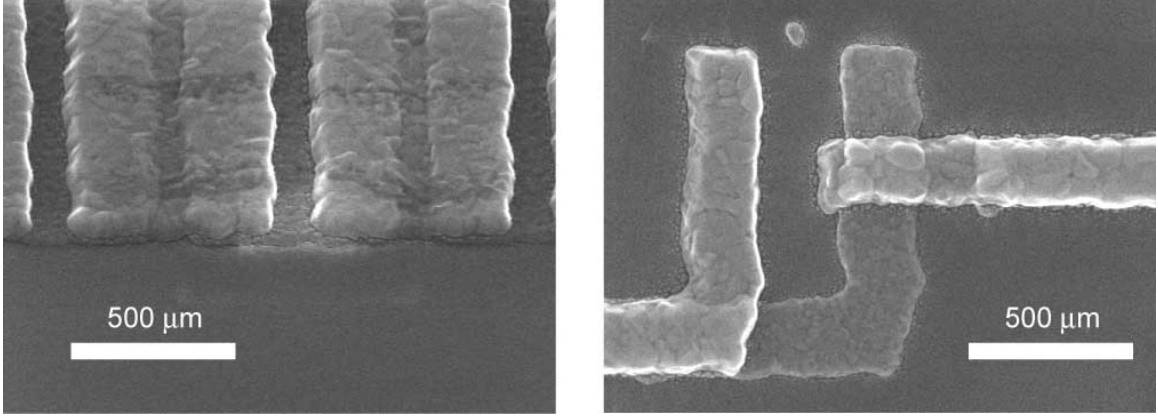


Figure 2-2: Left: Tilted SEM image of a section of the Josephson array from a similar device. Right: SEM image of the black-sheep junction from a similar device.

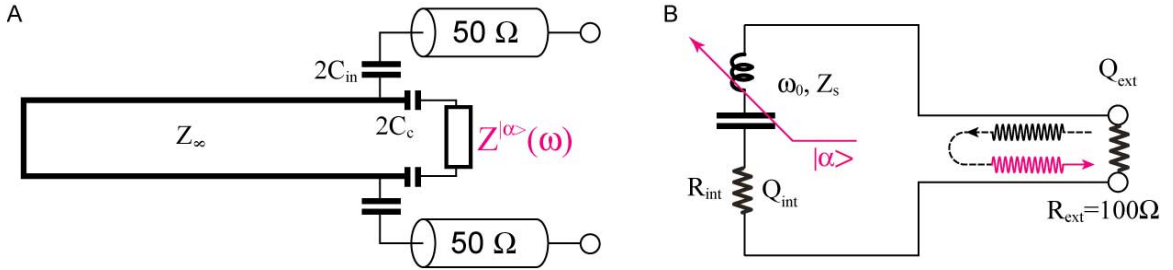


Figure 2-3: Circuit QED. Left: electrical model of a qubit interacting dispersively with the CPS transmission line resonator. Thick solid line represents the distributed transmission line. Right: simplified circuit model of the resonator, from the point of view of an incoming signal.

of e-beam lithography and double-angle evaporation. Such simplification in the fabrication of a superconducting qubit has been made possible because: i) the dimensions of both the black-sheep junction and the array junctions are chosen to be sufficiently close for patterning both types of junction in a single resist mask ii) the strips of the CPS resonator are sufficiently narrow so that the e-beam and lift off process used for the small junction fabrication can be readily applied to the resonator as well; in addition, space remains to accommodate useful test junctions and arrays fabricated simultaneously with the rest of the circuit.

2.2 Microwave readout by reflectometry

In a dispersive measurement scheme, monitoring of the qubit state reduces to monitoring the resonance frequency of the readout resonator. We use the lowest differential mode of our resonator, which corresponds to the frequency ω_0 at which the physical length of the CPS transmission line matches a quarter of the wavelength. The next order resonance lies at $3\omega_0$, and therefore is disregarded. The qubit can be viewed as a high impedance termination $Z^{|\alpha\rangle}(\omega)$ placed at the open end of the transmission line (Fig. 2-3), and depends both on the frequency ω and the qubit state α . It provides a small contribution $\chi^{|\alpha\rangle}$ - termed the dispersive shift - to the resonance frequency ω_0 , when the qubit is in state $|\alpha\rangle$. The shift in the resonance frequency is detected by monitoring the complex-valued reflection amplitude for the scattering of a microwave signal off the resonator.

2.2.1 Reflection amplitude

The input impedance of our readout resonator, near its resonant frequency ω_0 , and viewed by the driving coaxes¹, is well approximated by a series *LCR* circuit [26]. This, after some algebra, directly follows from the general formula for the reflection coefficient [26] and Eq. (1.2) in the introduction for the transmission line input impedance. The reflection amplitude then takes the form:

$$\Gamma(\omega, \omega_0) = \frac{2i\left(\frac{\omega - \omega_0}{\omega_0}\right) - Q_{\text{ext}}^{-1} + Q_{\text{int}}^{-1}}{2i\left(\frac{\omega - \omega_0}{\omega_0}\right) + Q_{\text{ext}}^{-1} + Q_{\text{int}}^{-1}} \quad (2.1)$$

where Q_{ext} is the quality factor due to the energy loss in the matched measurement apparatus while Q_{int} is the quality factor due to the energy loss inside the resonator (electrically represented by a resistor in series with the *LC*-circuit). For the circuit under consideration, $Q_{\text{int}} = R_{\text{int}}/Z_s$ while $Q_{\text{ext}} = R_{\text{ext}}/Z_s$, where $Z_s = \sqrt{L_s/C_s}$ is the effective impedance of the resonating mode. All the internal dissipation, be it dielectric loss, resistive loss, or radiation, is lumped into a single parameter R_{int} while the energy dissipation outside the resonator is

¹On the contrary, viewed by the qubit from the “inside” of the resonator, the impedance is that of a parallel *LC*, with impedance $Z_0 = \frac{\pi}{4}Z_\infty$. Quantum fluctuation of voltage across this resonator determine the coupling of the qubit to the field, as discussed in the next chapter.

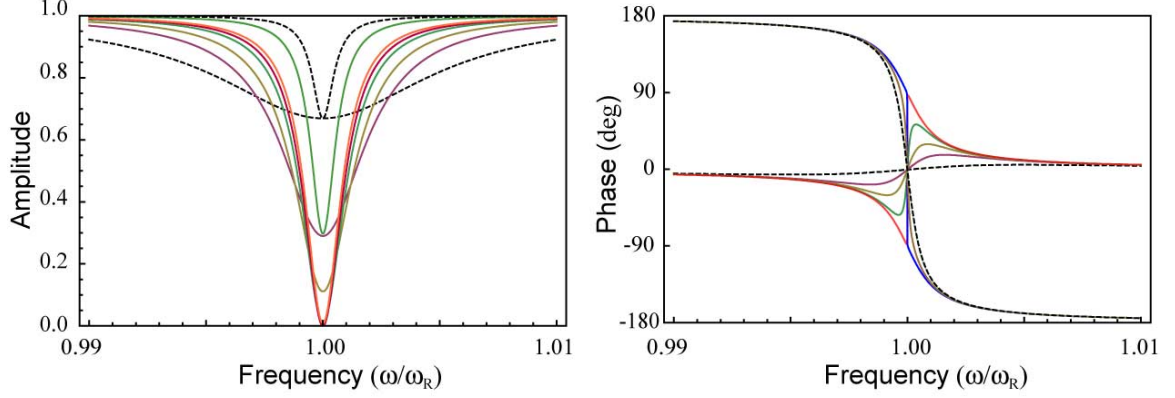


Figure 2-4: Amplitude and phase of the reflection amplitude as a function of frequency, near resonance of a quarterwave resonator, for a set of value $Q_{\text{ext}} = 1000$ and sets of $Q_{\text{int}} = \{100, 300, 500, 800, 999\}$, and $Q_{\text{int}} = \{1001, 1200, 3400, 10000\}$. The two limiting cases of $Q_{\text{int}} = 100 = Q_{\text{ext}}/10$ and $Q_{\text{int}} = 10000 = 10Q_{\text{ext}}$ are indicates with dashed lines.

lumped into R_{ext} . Conversion from the distributed resonator to the lumped element model is given by the following relations: $Z_s = 1/(\omega_0^2 C_{\text{in}}^2 \frac{\pi}{4} Z_{\infty})$, $R_{\text{ext}} = 100 \Omega$ (because of the differential excitation with two coaxes), both the value of Z_{∞} and ω_0^2 are obtained from the dimensions of the transmission line using either “txline”, a free software package from Applied Wave Research, or analytic expressions [57].

In general, both the amplitude and the phase of Γ contain information on the scatterer. It is instructive to plot $|\Gamma(\omega, \omega_0)|$ and $\text{Arg}[\Gamma(\omega, \omega_0)]$ for a given Q_{ext}^{-1} and a set of Q_{int}^{-1} going from $Q_{\text{ext}}^{-1} > Q_{\text{int}}^{-1}$ to $Q_{\text{ext}}^{-1} < Q_{\text{int}}^{-1}$ (Fig. 2-4). When the external dissipation dominates, $Q_{\text{ext}}^{-1} \gg Q_{\text{int}}^{-1}$ (overcoupled regime), almost all the energy sent onto the resonator returns back, so $|\Gamma(\omega, \omega_0)| = 1$. Only the phase of the nearly 360 degree phase change over the frequency range of order $\omega_0 Q_{\text{ext}}^{-1}$ in the $\text{Arg}[\Gamma(\omega, \omega_0)]$ tells us that the signal actually scattered off a resonator, and not off an open termination. Interestingly, in the opposite case of $Q_{\text{ext}}^{-1} \ll Q_{\text{int}}^{-1}$ (undercoupled regime), the amplitude of the reflected signal also reaches values near unity, but this time because of the mismatch between R_{ext} and R_{int} ($R_{\text{ext}} \gg R_{\text{int}}$). Therefore, there is no phase response in this case, the undercoupled regime is essentially

²Actually, the presence of the finite C_{in} coupling capacitance shifts the resonance frequency down by $\frac{\pi}{8} Z_{\infty} \omega_0^2 C_{\text{in}}$. Since we only deal with resonator impedance and frequency, rather than inductances and capacitances, we shall assume that this frequency shift is already incorporated into what we call the resonance frequency.

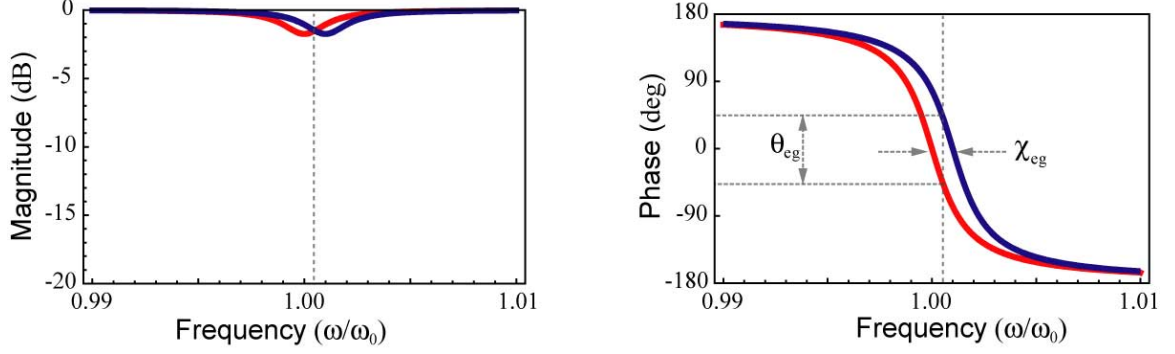


Figure 2-5: Dispersive phase shift. Modulus and phase of the reflection amplitude for the parameters of our setup and for two values of the resonator frequencies, differing by χ_{eg} . In relative terms, phase sensitivity dominates over the absolute value sensitivity and therefore used as a primary measured quantity.

equivalent to scattering off an open circuit. Finally, in the special situation when $Q_{\text{ext}}^{-1} = Q_{\text{int}}^{-1}$ (critically coupled), equivalent to $R_{\text{int}} = R_{\text{ext}}$, and for ω close to ω_0 , all the power sent onto the resonator is absorbed inside the resistor R_{int} , and no power comes back, so $|\Gamma(\omega, \omega_0)|$ is nearly zero. In this regime, quite amusingly, the phase response for $Q_{\text{ext}}^{-1} \rightarrow Q_{\text{int}}^{-1}$ becomes infinitely sharp and might create an impression that the resonator has no internal losses but a very large Q_{ext} . However, the dip in the amplitude response immediately testifies to the presence of internal dissipation.

In our CPS resonator $Q_{\text{ext}} \simeq 400 \ll Q_{\text{int}} \approx 4000$ causing $|\Gamma(\omega, \omega_0)|$ to be very close to unity³. This situation of collecting all the energy leaving the resonator, and carrying information on the qubit state, is best as it maximizes signal-to-noise ratio (Fig. 2-5). The phase $\theta = \text{Arg}(\Gamma)$ of the reflected signal is a rapid function of frequency: $\theta = 2 \arctan 2Q_{\text{ext}} \frac{\omega - \omega_0}{\omega_0}$. Finally, the phase change $\theta_{eg} = \theta_e - \theta_g$ between the qubit excited state e and the ground state g is given by

$$\theta_{eg} = 2 \arctan \left(2Q_{\text{ext}} \frac{\chi_g}{\nu_0} \right) - 2 \arctan \left(2Q_{\text{ext}} \frac{\chi_e}{\nu_0} \right) \quad (2.2)$$

³The reason for such relatively low internal quality factor remains unknown to us. We have tested resonators (without fluxonium qubits inside) of various transverse dimensions and film thickness, with no noticeable difference in internal dissipation. Fortunately, experiments on fluxonium did not require a high Q cavity, so the important question of fabricating high quality resonators with e-beam remains to be solved by a future work

where $\nu_0 = \omega_0/2\pi$ is the resonator frequency in Hz. Note that since θ_{eg} saturates quickly once $2Q_{\text{ext}} \frac{\chi_e - \chi_g}{\nu_0} > 1$, increasing Q_{ext} above the value $\left(\frac{\chi_e - \chi_g}{\nu_0}\right)^{-1}$ will not improve the sensitivity. In our experiment $\chi_{e,f} - \chi_g$ lies between 1 MHz and 10 MHz, while $\nu_0 = 8.175$ GHz, so $Q_{\text{ext}} = 400$ is a convenient choice with a measurement bandwidth of 20 MHz.

2.2.2 Low temperature setup

Our experiments were performed in a dilution refrigerator with base temperature 10–20 mK (Fig. 2-6-left). The task is to connect the device at mK temperatures to the room temperature test equipment, without exposing the cold sample to thermal noise, or dissipating more heat than the refrigerator can handle. Moreover, the readout signal returning from the sample must be minimally attenuated until it reaches the first amplification stage. These considerations lead to the following low-temperature setup. Both resonator and the qubit are differentially excited via the Δ -port of a 180° hybrid (Krytar, 2 – 18 GHz), whose two outputs are connected to the two ports of the sample holder. Incoming and outgoing signals are separated with a directional coupler (Krytar, 2 – 20 GHz). The incoming signal line is attenuated using 10 and 20 dB microwave attenuators (XMA) at all temperature stages (excluding the 800 mK stage) of the refrigerator, to remove non-equilibrium noise. The output line is amplified at the 4 K stage with a low-noise HEMT amplifier (Caltech, 1 – 12 GHz, 30 dB gain, ~ 5 K noise temperature). Two cryogenic isolators (Pamtech, 4 – 12 GHz, 15 dB) are placed between the amplifier and the sample, at the 800 mK stage and at the base stage, again to remove non-equilibrium noise, especially that coming from the amplifier. A low pass filter with tested rejection band 10 – 40 GHz was introduced for additional shielding from frequencies above the circulator bandwidth. Stainless steel SMA cables are used to connect between the different temperature stages. All components are thermally anchored to the proper refrigerator stages. A ~ 1 cm diameter custom made superconducting coil is glued to the sample holder, a few mm away from the chip, to provide perpendicular magnetic flux bias. Connection to the coil between 300 K and 4 K is made using 30 Ω resistive twisted pair. The sample holder together with the coil is placed into a Cryoperm cylinder to shield it from stray quasistatic magnetic fields.

2.2.3 Room temperature setup

Outside the refrigerator, the experimental setup is organized as follows (Fig. 2-6-right). The readout signal is provided by an Agilent E8257D generator (RF), the qubit pulses are generated using an Agilent E8267D vector signal generator (IQ) combined with a Tektronix 520 arbitrary waveform generator (AWG). Both readout and qubit signals are combined at room temperature and sent into the IN line of the refrigerator. The reflected ~ 8 GHz readout signal from the refrigerator OUT line is amplified at room temperature with a Miteq amplifier (1 – 12 GHz, 30 dB gain), mixed down with a local oscillator signal (LO), provided by a cheap old HP 8672A, to a 1 – 50 MHz IF signal, then filtered and amplified with the IF amplifier (SRS SR445A), and finally digitized using one channel of the 1 GS/s Agilent Acqiris digitizer. We used low heterodyne frequencies for slow measurements, like ground-state field modulation or continuous-wave spectroscopy, while a 50 MHz, frequency, exceeding twice the maximum measurement bandwidth of $\nu_0/Q \simeq 20$ MHz, was used in pulsed measurements for maximum time resolution. A reference IF signal is created by mixing a copy of the RF and LO and digitized using another channel of the Acqiris. A software procedure then subtracts the phases of the two IF signals, resulting in good long-term stability of the phase measurement. Short-term stability is implemented by phase locking every instrument to a Rb 10 MHz reference (SRS FS725). The marker signals of the AWG serve triggers to the other instruments. The magnetic coil is biased with a Yokogawa 7751 voltage source in series with a 1 : 10 voltage divider and a 1 k Ω resistor at room temperature. We found no need for further filtering of the bias coil in order to reach the sub- $\mu\Phi_0/\sqrt{\text{Hz}}@1$ Hz. Probably the coil itself, consisting of about 500 tightly packed turns, acts as a low-pass filter, in addition, the sample holder efficiently rejects the high frequency fields due to high conductivity and thick walls of the copper sample holder.

We opted for an heterodyne demodulation scheme, to avoid DC whatsoever in our setup and also to avoid the imperfections of the IQ mixers [60], [23] usually employed with the homodyne demodulation schemes. The reference IF signal (acquired in channel one) proved very useful in fighting drifts in the relative phase between RF and LO. Denoting the digitized signals on channel one and channel two as $S_1(t)$ and $S_2(t)$, respectively, we can express them as $S_j(t) = A_j(t) \cos(\omega_{IF}t + \varphi_j(t))$, $j = 1, 2$, where $A_j(t)$ and $\varphi_j(t)$ are

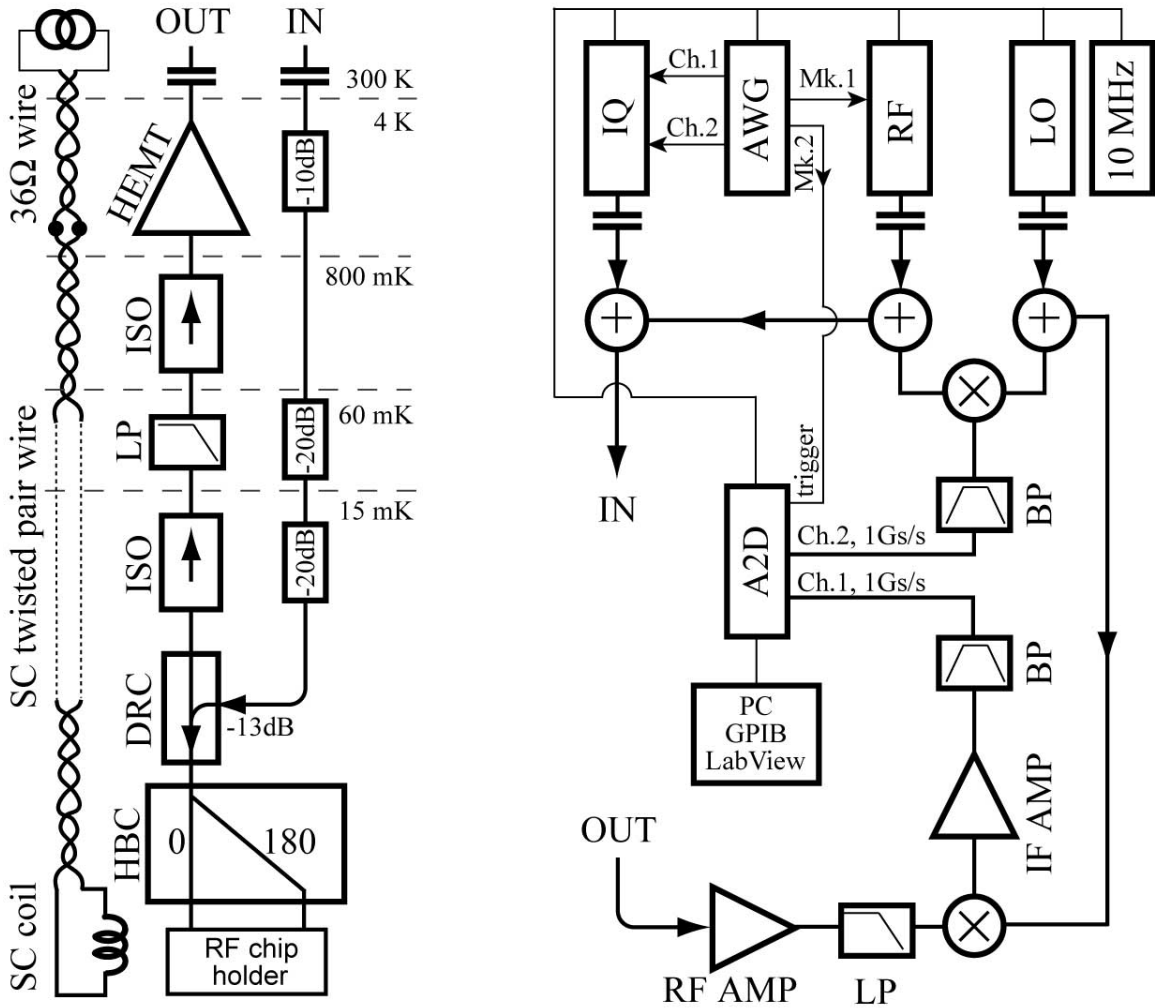


Figure 2-6: Cryogenic setup. Left: dilution refrigerator part of the microwave reflectometry setup. HEMT - high electron mobility cryogenic amplifier, ISO - cryogenic broadband isolator, LP - low pass filter, DRC - directional coupler, HBC - 180 degree hybrid coupler, see text for more details. Right: room-temperature signal generation and demodulation setup. LO - continuous microwave source, RF - pulsed (Mk.1 controlled) wave source, IQ is a vector signal generator for driving the qubit transitions, AWG - arbitrary waveform generator, A2D- two-channel fast digitizer, “+” - matched signal combiner/splitter, “×” - microwave mixer, BP- and pass filter, “10 MHz” - Rb reference, RF AMP - a room temperature microwave amplifier.

the phase and amplitudes of the signal varying slowly on the time scale of the heterodyne period $T_{IF} = 2\pi/\omega_{IF}$. The phase of the first signal $\varphi_1(t)$ contains two components: (i) the phase difference between the LO and RF generators, $\varphi_{LO-RF}(t)$, which is the major cause of the phase drift on the time scale of minutes (ii) the phase $\varphi_{\text{cables1}}(t)$, due to possible electrical length fluctuations, $\varphi_1(t) = \varphi_{LO-RF}(t) + \varphi_{\text{cables1}}(t)$. The phase $\varphi_2(t)$ contains three components: same $\varphi_{LO-RF}(t)$, different $\varphi_{\text{cables1}}(t)$, and of course the resonator phase θ . Therefore, by monitoring the phase difference $\varphi_2 - \varphi_1$, instead of just φ_2 , we get rid of the problem of phase-locking of the two generators on the time scale exceeding the sequence digitization time.

The computer processing of the acquired channels is done according to the following scheme, similar to that described in reference [23]. First, we compute signal quadratures by the Fourier transform:

$$\begin{aligned} I_j(\tau) &= \int_{\tau}^{\tau+T_{IF}} dt' S_j(t') \cos \omega_{IF} t \simeq \frac{1}{2} A_j(\tau) \cos \varphi_j(\tau) \\ Q_j(\tau) &= \int_{\tau}^{\tau+T_{IF}} dt' S_j(t') \sin \omega_{IF} t \simeq \frac{1}{2} A_j(\tau) \sin \varphi_j(\tau) \end{aligned} \quad (2.3)$$

where the time τ is now discrete with the step T_{IF} . Essentially, we have ignored the variations of $A_j(t)$ and $\varphi_j(t)$ during the heterodyne period. Applying trigonometric identities we can easily extract the phase:

$$\theta + \varphi_{\text{cables1}} - \varphi_{\text{cables2}} = \arctan((I_1 Q_2 - I_2 Q_1)/(I_1 I_2 + Q_1 Q_2)) \quad (2.4)$$

The phase shifts due to the cables are quite stable, and can be subtracted out. The only drift in them was found to be due to the variations of the electrical length with temperature because of the helium level fluctuations.

Typically, spectroscopic/time-domain measurements on fluxonium were performed by populating the cavity with 1–2 photons. This means that the readout signal coming out of the cavity corresponds to a power of $P_{\text{out}} = h\nu_0 \times \nu_0/Q_{\text{ext}} \approx 0.1$ fW. Therefore, the Caltech preamplifier with its noise temperature of approximately 5 K and gain of about 35 dB was the key to our setup. The total noise temperature of the system was significantly degraded

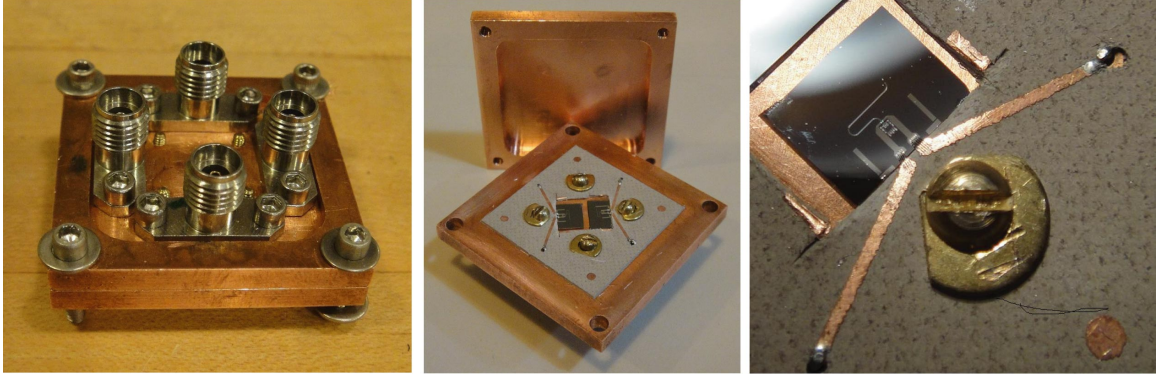


Figure 2-7: Photographs of the chip holder carrying the actual fluxonium device. Anritsu K connectors guide microwaves from coaxial cables to Cu microstrip lines ($300\ \mu\text{m}$ wide) on the printed circuit board. The center conductor of the K connector is soldered to the beginning of the microstrip. Microstrip lines continue to the chip by means of 5-6 short wirebonds.

by the losses between the amplifier and sample. Those include losses in the circulator (about 0.5 dB each) and losses in the fairly long stainless cables interconnecting the readout line (at least 3 – 4 dB). Hence the noise temperature of our measurement system is likely to be at best 20 K [26].

2.3 Sample holder

Although at least one solution for a sample holder already existed [60], [23], [24], we decided to develop a new and somewhat more versatile sample holder which a) does not require professional machining, b) does not require a complex printed circuit board, for instance manufacturing of vias, c) robust to cryogenic environment, d) completely encloses the sample, and most importantly, d) operates in the frequency band up to 20 GHz. Fig. 2-7 presents photographs of our holder with two test chips mounted. Each chip is glued using GE varnish to the copper base of the holder, and with the closed lead is fully shielded from both residual RF, infrared and optical photons. The holder provides two well-matched transitions from the SMA-compatible Anritsu K-connectors on the outside of the holder to the two microstrip lines made on a PCB inside the holder. The resonator's on-chip launching pads are then wirebonded to the ends of the two microstrip lines. This holder is capable of guiding microwaves from commercial coaxial cables onto a chip with less than 14 dB of

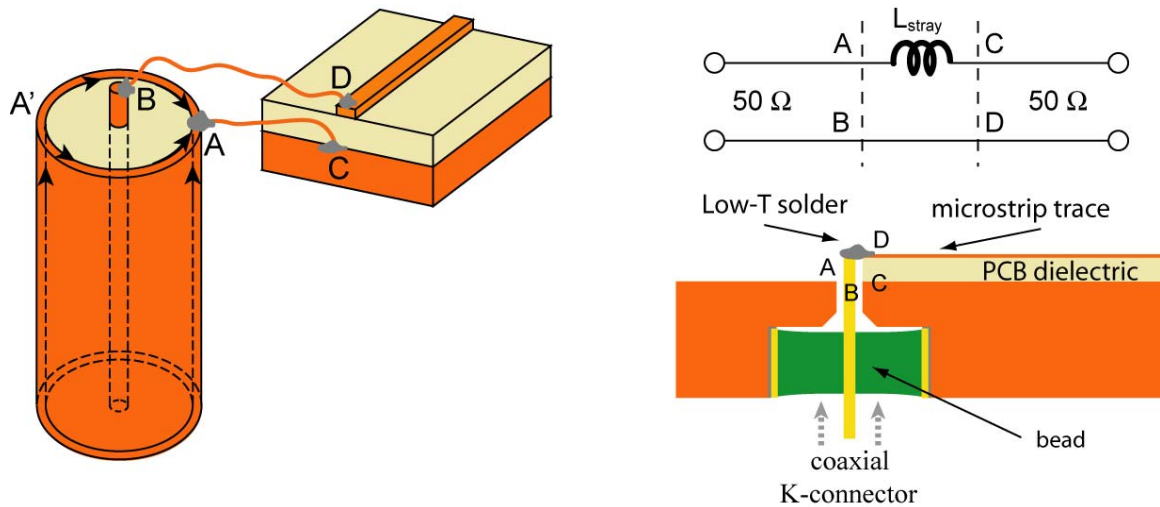


Figure 2-8: Left: a sketch of the coaxial to microstrip adapter. Ground currents traveling from point A' needs to first reach point A in order enter the ground plane of the microstrip (point B), while center conductors of both structures could be connected with a very short link (points B and C). Top-right: circuit representation of the reflection mechanism at the interface of the coax and the microstrip. Bottom-right: Schematic of the right angle coaxial to microstrip transition on which our sample holder design is based. Large diameter commercial coax is reduced using the coaxial bid to the transverse dimensions of the microstrip.

return loss at frequencies over 20 GHz, and less than 20 dB up to 14 GHz. Below we present some details.

In order to transmit microwaves from one type of transmission line to another, it is required, but by far not sufficient, to match their wave impedances. Even in the matched case, reflections still take place at the interface between a coaxial transmission line and a microstrip for the following reason (see Fig. 2-8 for illustrations). The center conductor of the coax can be connected to the microstrip trace, at least in theory, using an infinitely short connection, thus not contributing any spurious impedance. Unfortunately, this is not the case with the outer conductors, the cylindrical inner surface of the coax shield and the ground plane of the microstrip, respectively. As illustrated in Fig. (2-8), a fraction of the the ground current flowing in the coax shield has to travel a path length of order coax radius plus coax shield thickness, in order to reach the ground plane of the microstrip. Such profound imperfection could be modelled as an additional inductance L_{stray} to the ground currents, and, for coaxes with a few mm in diameter could easily reach values of order

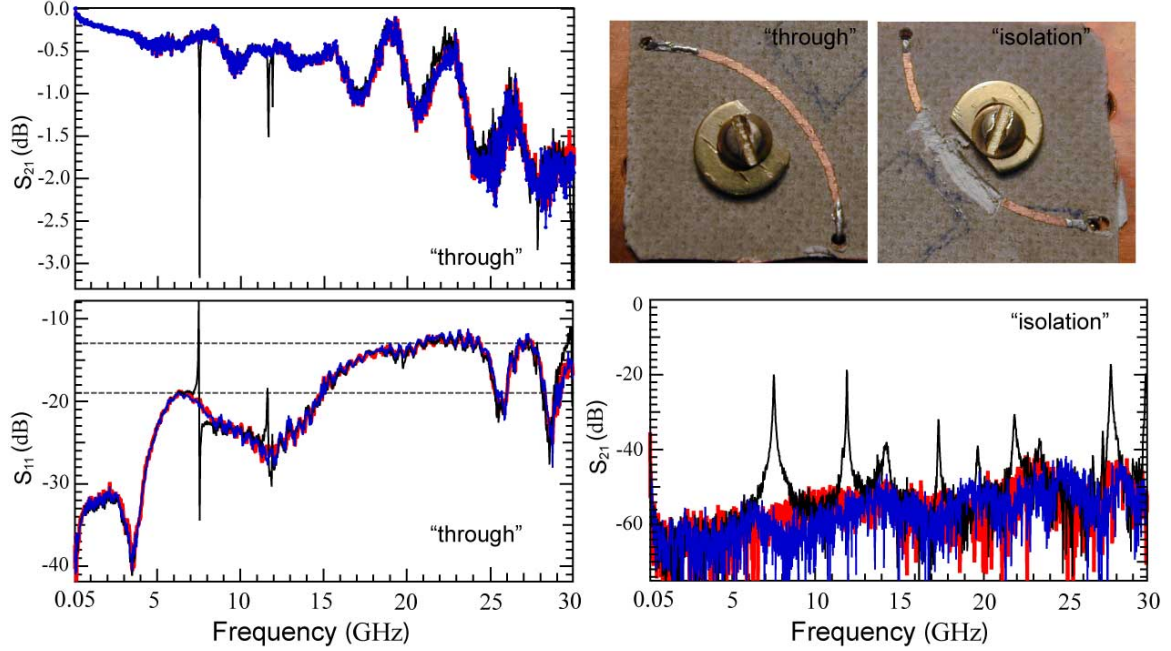


Figure 2-9: Transmission, return loss and isolation data on our sample holder using test microstrip lines. Blue, black and red traces indicate data taken, respectively, without the lead, with the lead, and with a piece of microwave absorbant attached to the inner face of the lead.

$\mu_0 \times 1 \text{ mm} \simeq 1 \text{ nH}$. At frequencies of order 10 GHz, this becomes comparable to the 50Ω impedance of the guiding structures, so reflections at these frequencies are inevitable. We note, that we described the absolute best case scenario, in reality the situation is worse due to similar types of imperfections.

Inspired by the work [61], we have also chose the right angle transition between the coax and the microstrip. The simplest approach to reduce the strays associated with the mismatched geometries of the two transmission lines, would be to reduce the transverse dimensions of both (Fig. 2-8–bottom-right). On the microstrip side, we have achieved this by using dielectric material with $\epsilon \approx 10$ and width of $370 \mu\text{m}$ and microstrip trace width of $300 \mu\text{m}$, yielding a 50Ω wave impedance. On the coax side, we used the parts of the Anritsu flange-mount K connector. The active part of our sample holder consists of a copper plate with a set of concentric holes centered at the desired locations of the transition. The Anritsu designed bead (a coaxial section with small dimensions) is soldered inside the hole using a soldering paste and a heat gun or hot plate. The depth of the holes are chosen such

that the bead fits tightly into the hole and is level with copper surface at the connector side, and also such that the pin of the bead is level with the microstrip trace. The microstrip trace is connected to the bead by means of low temperature solder (bismuth based, with melting temperature below 100C). It is crucial here that the bottom metalization of the PCB is removed and the role of the ground plane is played by the copper base of the sample holder. This way the path length of the coax ground current to the microstrip ground plane is minimized.

To test the sample holder, we have used two test circuit boards, one providing 50 Ω on-chip connection between the two coaxial inputs (“through test”), and the other one with a broken microstrip (“isolation test”) (Fig. 2-9). Transmission and reflection in the “through test” reveal excellent, according to microwave component standards, matching properties in the range up to 20 GHz. Box resonances in both reflection and transmission appear when the lead of the sample holder is tightly closed. The resonances are further pronounced in the isolation test. We have checked that the resonances persist even when both the PCB structure and the screws are removed from the box (data not shown), so the resonances must be the geometric box resonances. A cheap, but not necessarily the best, way to suppress these resonances is to add a thin layer of absorptive material (Ecsorb, any type) at the inner side of the closing lead. This immediately suppressed all the resonances, as the absorptive lead efficiently imitates free space. In order to push the resonances outside the frequency range of interest without introducing dissipation to the box, one must design the shape of the lead properly. Although we did not find any indication of the box resonances in our (fairly sensitive to them) T_1 -spectroscopy experiments, such box resonances can be pushed to higher frequencies in future designs by modeling the shape of the lead. The soldering contact survived more than 20 thermal cycles and the circuit board survived several chip rebondings, indicating mechanical and electrical robustness of our design. The sample holder can be manufactured in a student machine shop, by a student, within one day.

Chapter 3

Fluxonium: concepts

The fluxonium artificial atom is defined by its hamiltonian (1.22), for the parameter regime $E_L \ll E_J$, $E_J/E_C \gtrsim 1$, and $E_S \ll \sqrt{8E_J E_C} \exp(-\sqrt{8E_J/E_C})$. In this chapter, we describe theoretically the basic fluxonium properties, namely its spectrum and sensitivity to various decoherence sources. Particular attention is given to the novel aspects of its dispersive readout, the so-called cQED readout, originally implemented with Cooper pair boxes and transmons [19, 23, 51]. Although the coupling of fluxonium to its readout also obeys the conventional linear coupling hamiltonian (1.23), here the magnitude of the dispersive shift is essentially independent of the rate of spontaneous emission of the qubit into the readout cavity (Purcell-induced qubit relaxation rate) for many octaves of the qubit frequency, unlike in previous experiments [62, 63].

3.1 Spectrum

3.1.1 Fluxons and plasmons

Here we shall stick to the model of fluxonium as the “Cooper pair box junction shunted by a slippery inductance” (Fig. 1-15-right). Moreover, since the effect of CQPS in the inductance is perturbative, we shall assume $E_S = 0$ until we reach the question of CQPS-induced dephasing. Without CQPS, the fluxonium circuit hamiltonian reduces to a “particle-in-a-box” problem and therefore is amenable to a full quantitative treatment. We will occasionally refer back to the model of “array with a black-sheep” (Fig. 1-15-left) to train our intuition

on this device.

Without phase-slip in the array, the hamiltonian of the device is written as:

$$H_{\text{fluxonium}} = 4E_C n^2 - E_J \cos \varphi + \frac{1}{2} E_L (\varphi - \varphi_{\text{ext}})^2 \quad (3.1)$$

We remind the reader that $n = -i \frac{d}{d\varphi}$ is the conjugate momentum to the generalized coordinate φ with the resulting commutation relation $[n, \varphi] = i$. This way the first term in the hamiltonian (3.1) is analogous to mechanical kinetic energy, so that the larger E_C the lighter the equivalent mechanical particle is. The last two terms of (3.1) then depend only on the generalized coordinate φ and therefore play the role of the mechanical potential energy¹. Note that in vast contrast to the Cooper pair box, here the number operator n has a continuous spectrum, while the phase φ is defined on the entire real axis, rather than being 2π -cyclic [45]. The latter fact is particularly obvious, given that $H_{\text{fluxonium}}(\varphi + 2\pi) \neq H_{\text{fluxonium}}(\varphi)$. The continuity of n follows directly from the extended nature of φ as a property of the Fourier transform, and also carries a simple physical interpretation: the charge at the electrodes of the black-sheep junction originates from the displacement of the Cooper-pair condensate with respect to the ions of the crystal lattice of the superconductor; since this displacement can be arbitrarily small, n does not have to be quantized. After all, by shunting the Cooper pair box junction with a piece of superconductor, the circuit loses its islands, therefore forgetting about the discreteness of charge and associated offset-charge sensitivity. Of course, here we neglect the effect of CQPS in the inductance, which will bring back some charge sensitivity.

The most straightforward way to understand the spectrum of the hamiltonian (3.1) is numerics. Below we shall look at the numerically obtained spectra and comment on their physical meaning. The numerics is most efficient in the basis of harmonic oscillator functions, corresponding to the case $E_J = 0$. This is because both systems have bound states with exponentially decaying tails. It is further convenient to make a variable change $\varphi \rightarrow \varphi - \varphi_{\text{ext}}$, which does not affect the conjugate momentum n , but rewrites the potential

¹The hamiltonian (3.1) is formally identical to the hamiltonian for the RF-SQUID [64, 65]. However, there is a vast difference in parameter regime. The RF-SQUID always operates in the regime of $E_L \sim E_J$ and $E_J/E_C \gg 1$. Fluxonium, on the contrary, operates in the regime $E_L \ll E_J$ and $E_J \sim E_C$.

energy term $-E_J \cos \varphi + \frac{1}{2}E_L(\varphi - \varphi_{\text{ext}})^2 \rightarrow -E_J \cos(\varphi + \varphi_{\text{ext}}) + \frac{1}{2}E_L\varphi^2$. Then the matrix form of the modified hamiltonian can be written in terms of the matrix elements of the translation operator, $T = \exp(-i\varphi)$, between the Fock states $|k\rangle$ of the harmonic oscillator defined by E_C and E_L : $H_{kk'} = \sqrt{8E_C E_L}(k+1/2)\delta_{kk'} + \frac{1}{2}T_{kk'} \exp(i\varphi_{\text{ext}}) + \frac{1}{2}T_{kk'}^\dagger \exp(-i\varphi_{\text{ext}})$. Since the $|k\rangle$ states are either symmetric or antisymmetric, $T_{kk'} = (-1)^{k+k'} T_{kk'}^\dagger$. Therefore, one can write the hamiltonian (3.1) in the matrix form as:

$$H_{kk'} = \sqrt{8E_C E_L}(k+1/2)\delta_{kk'} + \frac{1}{2}T_{kk'} \left(\exp(i\varphi_{\text{ext}}) + (-1)^{k+k'} \exp(-i\varphi_{\text{ext}}) \right) \quad (3.2)$$

Restricting to as few as 50 Fock states we were able to evaluate in a reasonable time and with excellent precision the spectrum and other properties of this hamiltonian ([45]).

To develop the fluxonium intuition, we plot the transition spectrum obtained numerically for several sets of circuit parameters. Let us fix the value of inductive energy at $E_L = h \times 0.5$ GHz, (a value very close to the actually implemented array inductance) and vary E_J , E_C and, and φ_{ext} . Results of numerical diagonalizations are summarized on the Fig. (3-1).

The first pair of parameters is $E_J = 100$ and $E_C = 4$, or, equivalently, $E_J/E_C = 25$ and the plasma frequency $\omega_p = \sqrt{8E_J E_C} = 2\pi \times 56$ GHz. Although this example corresponds to an unlikely high plasma frequency for an aluminum junction, it is a useful example, as it justifies numerically the quantum phase-slip language. The spectrum (Fig. 3-1-A) is essentially indistinguishable from the phase-slip spectrum (Fig. 1-8-A, B) of the hamiltonian (1.13), if we replace E_L with $E_L^\Sigma = (E_L^{-1} + E_J^{-1})^{-1}$. The quantum phase-slip amplitude here calculates to $E_{SB} \ll 1$ MHz and therefore cannot be resolved in the plots. Further insight comes from superimposing the energy levels with the potential energy of the hamiltonian (3.1) at $\varphi_{\text{ext}} = 0$ (Fig. 3-1-C). It is clear that the first 5 energy levels correspond to a zero-point motion of a particle in the 5 Josephson wells – the fluxon states. Such states are very weakly coupled by tunneling, which is extremely weak for the choice of parameters. Each of the 5 fluxon states could be excited into a vibrational motion within one Josephson well at the frequency of approximately the plasma frequency ω_p (Fig. 3-1-C).

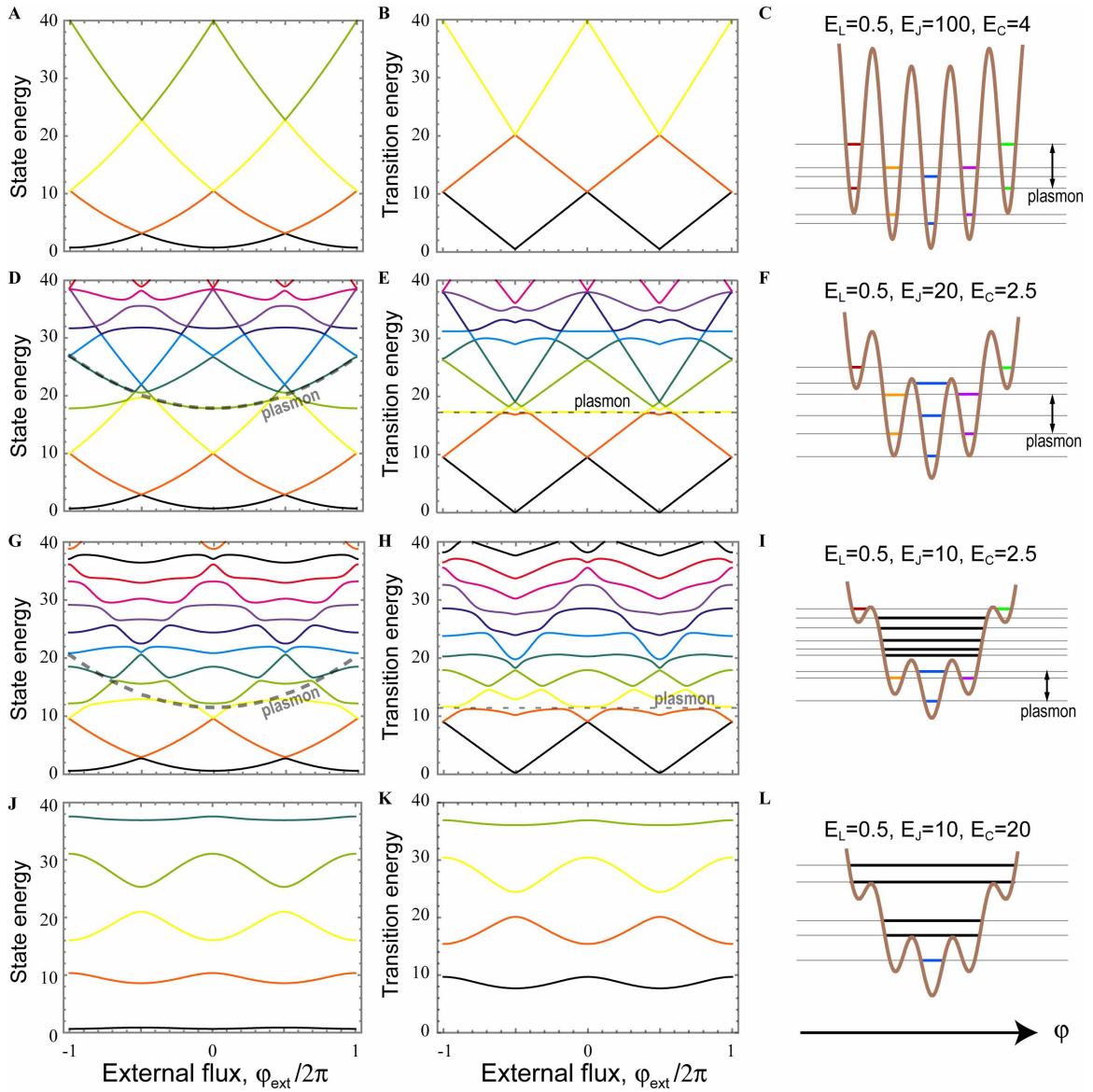


Figure 3-1: Fluxonium spectrum at a glance. Numerically computed spectrum (A, D, G, J), transitions from ground state (B, E, H, K) and the particle-in-a-box interpretation of the energy spectrum (C, F, I, L) for a set of parameters indicated on the figure. All energy units are in $h \times \text{GHz}$.

The approximation of low energies, employed to develop the quantum phase-slip language precisely means that such vibrational states take place at sufficiently high frequencies.

Next, let us couple the fluxon states a bit more strongly by choosing $E_J = 20$ and $E_C = 2.5$, so that $E_J/E_C = 8$ and $\omega_p = 2\pi \times 20$ GHz. Now both the quantum phase-slip exponent and the plasma frequencies are substantially lowered, so that $E_{SB} \sim 10$ MHz and some mixing between fluxons and plasmons takes place (3-1-D, E, F). The plasma state indeed shows up at around 18 GHz, slightly smaller than our estimate due to finite value of $\beta_L = E_J/E_L = 40$. Although the splitting between fluxon states is still too small to be resolved on this figure, the splitting between vibrationally-excited fluxon states is clearly visible. This is expected, because the tunneling between vibrationally-excited fluxon states effectively undergoes a smaller potential barrier.

Pushing further toward coupled fluxon states, we turn to parameters $E_J = 10$ and $E_C = 2.5$, or $E_J/E_C = 4$ and $\omega_p = 2\pi \times 14$ GHz, (Fig. 3-1-G, H, I) we observe a rather strong splitting between the fluxon transition (ground-to-second excited) and the plasma state at about 10 – 11 GHz. The phase-slip type spectrum is now almost completely destroyed with the exception of the lowest transition, which retained the correct zigzag shape. At higher energies the spectrum is dominated by a strongly coupled fluxon-plasmon motion. Turning to (Fig. 3-1-I), now only the lowest, central fluxon well contains both fluxon and plasmon levels. The other 4 lowest wells contain only a single semi-localized level each. In addition, a large number of vibrational states are present, which cannot be associated with a particular fluxon state.

Finally, let us fully destroy the phase-slip spectrum by further decreasing the inertia of the coordinate φ , by choosing $E_J = 10$, $E_C = 20$, so that $E_J/E_C = 1/2$ and $\omega_p = 40$ GHz (again somewhat at the higher end for aluminum devices). The resulting spectrum consists of transitions with much weaker flux dependence (Fig. 3-1-J,K,L). Not a single level could be interpreted as either a fluxon state or a plasmon state. On the contrary, now the spectrum could be interpreted as vibrational modes of the LC oscillator defined by the inductance L and the black-sheep junction capacitance C , with a small perturbation due to Josephson potential. Indeed, the average spacing between the levels is not given by ω_p but by a much smaller quantity, $\sqrt{8E_LE_C} \approx h \times 10$ GHz. In fact, at sufficiently high number

of quanta, the non-linearity due to the black-sheep junction weakens and every fluxonium circuit responds as an LC oscillator.

3.1.2 Matrix elements

To understand the dynamics of an artificial atom one has to know the matrix elements of its generalized position and momentum. In our case, matrix elements of the reduced charge n and phase φ determine the coupling of fluxonium to both external signals, circuits, and internal degrees of freedom. The results of the numerics performed for the parameters from Fig. (3-1) are presented on Fig. 3-2, for the external flux range $\{-0.5, 0\}$. Most of the features can be explained with simple analytical analysis, involving the picture of weakly coupled fluxon and plasmon states. In the regime of parameters where the quantum phase-slip language is appropriate, we can estimate the phase matrix element φ_{ge} between the ground $|g\rangle$ and the first excited $|e\rangle$ fluxon states using the two-level approximation. Clearly, in the vicinity of $\varphi_{\text{ext}} = \pi$, the states $|e\rangle$ and $|g\rangle$ could be very well approximated by linear combinations of states $|0\rangle$ and $|1\rangle$, which correspond to zero and one fluxon in the loop, respectively (or zero and one phase-slip through the black-sheep junction). The effective two-level hamiltonian reads

$$H_{ge} = \frac{1}{2}E_{\varphi}(\varphi_{\text{ext}})(|0\rangle\langle 0| - |1\rangle\langle 1|) + \frac{1}{2}E_{SB}(|0\rangle\langle 1| + |0\rangle\langle 1|) \quad (3.3)$$

where we have introduced the zigzag-shaped fluxon inductive energy $E_{\varphi} = 4\pi^2 E_L^{\Sigma} |\varphi_{\text{ext}}/2\pi - 1/2|$. Because of the finite E_{SB} we obtain the expected rounding of the $g \leftrightarrow e$ zigzag at $\varphi_{\text{ext}} = \pi$, which is given by the hyperbolic expression for the eigenenergies $E_{g,e} = \pm \frac{1}{2} \sqrt{E_{\varphi}^2 + E_{SB}^2}$. The transition energy is given by

$$E_{ge} = \sqrt{E_{\varphi}^2 + E_{SB}^2} \quad (3.4)$$

The eigenvectors at $\varphi_{\text{ext}} \simeq \pi$ ($E_{\varphi} \ll E_{SB}$) are given by symmetric and antisymmetric combinations of $|0\rangle$ and $|1\rangle$:

$$\begin{aligned}
|g\rangle_{E_\varphi \ll E_{SB}} &= \frac{1}{\sqrt{2}} |0\rangle + \frac{1}{\sqrt{2}} |1\rangle \\
|e\rangle_{E_\varphi \ll E_{SB}} &= \frac{1}{\sqrt{2}} |0\rangle - \frac{1}{\sqrt{2}} |1\rangle
\end{aligned} \tag{3.5}$$

and away from that spot, ($E_\varphi \gg E_{SB}$) by the weak mixing combinations of $|0\rangle$ and $|1\rangle$ (normalization is correct to first order in E_{SB}/E_φ):

$$\begin{aligned}
|g\rangle_{E_\varphi \gg E_{SB}} &= \frac{E_{SB}}{2E_\varphi} |0\rangle + |1\rangle \\
|e\rangle_{E_\varphi \gg E_{SB}} &= |0\rangle - \frac{E_{SB}}{2E_\varphi} |1\rangle
\end{aligned} \tag{3.6}$$

Now we are ready to evaluate the matrix element φ_{eg} by recalling (see Fig. (3-1-C,F)) that in the φ -coordinate representation, the wavefunction $\psi_0(\varphi) = \langle\varphi|0\rangle$ is sharply peaked at $\varphi = 0$ and $\psi_1(\varphi) = \langle\varphi|1\rangle$ is sharply peaked at $\varphi = 2\pi$. This immediately provides us with the estimate of $\varphi_{eg} = \int_{-\infty}^{\infty} d\varphi \psi_0(\varphi) \psi_1(\varphi) \varphi$:

$$\begin{aligned}
\varphi_{eg}(\varphi_{\text{ext}}) &= \pi, \quad E_\varphi \ll E_{SB} \\
\varphi_{eg}(\varphi_{\text{ext}}) &= \pi \frac{E_{SB}}{E_\varphi(\varphi_{\text{ext}})}, \quad E_\varphi \gg E_{SB}
\end{aligned} \tag{3.7}$$

We have thus arrived at the following property of the phase matrix element φ_{eg} in the phase-slip regime. It is sharply peaked at $\varphi_{\text{ext}} = \pi$ reaching the value of π and away from that point reduces approximately as the inverse transition frequency $\nu_{eg} = E_{ge}/h$. The peak width can be evaluated as $\delta\varphi_{\text{ext}} = E_{SB}/2\pi E_L^\Sigma$, so that the larger the splitting E_{SB} , the wider the peak. Overall, this behavior of $\varphi_{eg}(\varphi_{\text{ext}})$ makes sense, because away from $\varphi_{\text{ext}} = 0$, the number of fluxon states are no longer mixed, the total number of flux quanta in the loop is a conserved quantum number, so the dynamics freezes. Numerically, we confirm these conclusions in Fig. 3-2-A. The solid and dashed line both correspond to the deep phase-slip regime and fully concurs with expression (3.7). The dotted line agrees

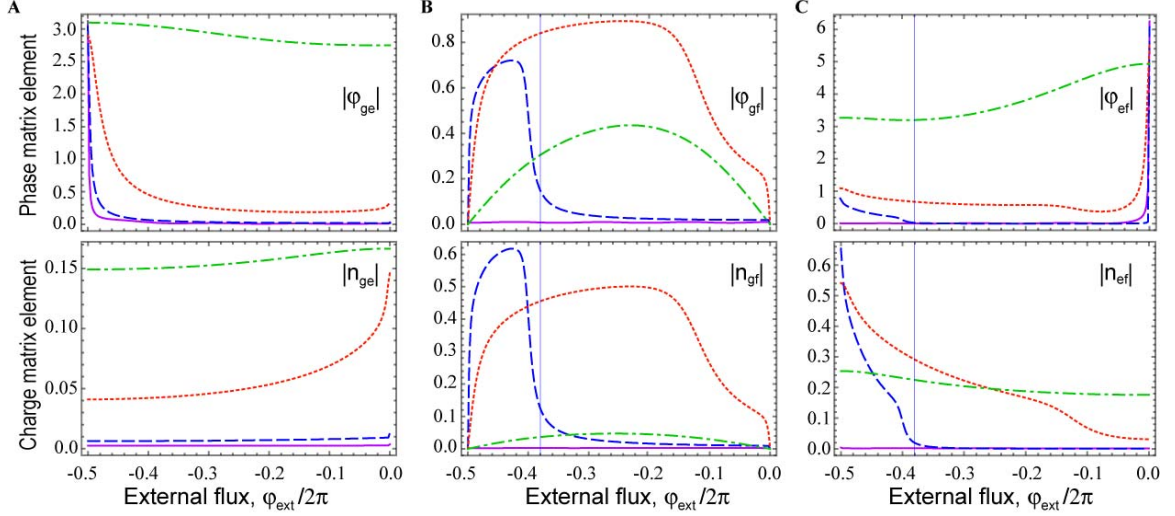


Figure 3-2: Matrix elements of n and φ for the fluxonium transitions as a function of external flux φ_{ext} : (A) $g \leftrightarrow e$, (B) $g \leftrightarrow f$, and (C) $e \leftrightarrow f$. Parameter choice coincides with that of Fig. (3-1): solid lines ($E_J = 100$, $E_C = 4$), dashed lines ($E_J = 20$, $E_C = 2.5$), dotted line ($E_J = 10$, $E_C = 2.5$) and dash-dot-dash line ($E_J = 10$, $E_C = 20$). Thin vertical line in (B) and (C) schematically separates the region in flux φ_{ext} where the f state changes from fluxon-like (to the right of the line) to the plasmon-like (to the left of the line), for the dashed line case ($E_J = 20$, $E_C = 2.5$).

qualitatively, but instead of vanishing at $\varphi_{\text{ext}} = 0$ actually shows a small rise – this is the effect of small mixing with the plasma states. Finally, the dash-dot-dash line bears no resemblance to expression (3.7), because the fluxon picture is lost and the ground to first excited transition is much closer to that of an oscillator made from inductance L and capacitance C , hence the weak flux dependence of φ_{eg} for that parameter choice.

Let us remark that the Cooper pair box charge matrix element follows exactly the same pattern (replace external flux with the gate charge and $|0\rangle$ and $|1\rangle$ states correspond to zero and one extra Cooper pairs on the island). We also note that the quantum phase-slip number matrix element m_{eg} from the hamiltonian (1.13) obeys to exactly the same relation (3.7).

As for the matrix element n_{eg} , it can be directly calculated from φ_{eg} and the transition frequency ν_{eg} using the following universal relation²:

²This expression is valid for arbitrary non-linear oscillator defined by a linear capacitance C and a non-linear inductance. For derivation, see the discussion around Eq.(3.30) and Eq.(3.33).

$$|n_{\alpha\beta}| = |\varphi_{\alpha\beta}| \nu_{\alpha\beta} R_Q C_J \quad (3.8)$$

Combining the relations (3.8, 3.7, and 3.4), we conclude that the number matrix element would be flux-independent in the phase-slip regime, and is given by (we are only interested in the absolute values of matrix elements here)

$$|n_{eg}(\varphi_{\text{ext}})| = \frac{\pi}{8} \frac{E_{SB}}{E_C} \quad (3.9)$$

The numerics fully respects (Fig. 3-2-A, bottom graph) the expressions (3.8, 3.9).

Next, we step forward and consider the third fluxonium state $|f\rangle$. In the case when $|f\rangle$ is still a fluxon state (plasma mode is higher up), the flux-dependence of the matrix element φ_{ef} counted from $\varphi_{\text{ext}} = 0$ is very similar to that of the matrix element φ_{ge} counted from $\varphi_{\text{ext}} = \pi$. There are two quantitative distinctions though. First, the peak value of φ_{ef} at $\varphi_{\text{ext}} = 0$ is given by $\varphi_{ef} = 2\pi$, not π , because the transition $e \leftrightarrow f$ mixes the fluxon states differing by two flux quanta. Second, since the mixing of the states $|0\rangle$ and $|2\rangle$ occurs via the state $|1\rangle$ as a second order process in E_{SB} (which one could interpret as a double phase-slip in the black-sheep junction), the splitting between the states $|e\rangle$ and $|f\rangle$ would be $E_{SB}^2/2E_\varphi(\varphi_{\text{ext}} = 0)$; the same quantity determines the width of the peak in φ_{ef} around $\varphi_{\text{ext}} = 0$. The situation gets more complicated when the $|f\rangle$ state mixes strongly with the plasma vibration states. Fig. (3-2-C) illustrates the discussion of this paragraph.

The direct $g \leftrightarrow f$ transition and its matrix elements (Fig. 3-2-B) display an additional feature. Since at the symmetry spots $\varphi_{\text{ext}} = 0$ and $\varphi_{\text{ext}} = \pi$ the fluxonium wavefunctions respect coordinate inversion symmetry, $\varphi_{gf}(\varphi_{\text{ext}} = 0, \pi) = 0$. Away from the symmetry spots, φ_{gf} is also strongly suppressed as it involves connecting the states involving zero and two flux quanta. In the case that the $|f\rangle$ state is a plasmon state, the matrix element would be similar to that in an harmonic oscillator of inductance L_J and capacitance C , and will show weak dependence on flux.

3.1.3 The fluxonium qubit regime

Which parameter set defines the fluxonium qubit? Let us go over the possible qualitatively-different regimes of our circuit.

First of all, let us again emphasize that we at all times work in the regime $E_L \ll E_J$, or using the RF-SQUID language, $\beta_L \gg 1$. In this regime the effective potential energy has well-defined fluxon wells, with the depth approaching E_J and separation approaching 2π . This is an inevitable requirement from having large number of junctions in the array. Depending on the E_J/E_C ratio, each fluxon well hosts a number of semi-stable plasmon states with approximate energy separation $\sqrt{8E_J E_C}$. For very large inertia, corresponding to the case $E_J/E_C \ll 1$, each fluxon well will host a forest of nearly harmonic states, corresponding to vibrating fluxons within each well. In the case of $\sqrt{8E_J E_C} \ll 2\pi^2 E_L^\Sigma$ these harmonic states will dominate the low-energy spectrum. It being somewhat trivial, we did not present this case in our numerical analysis.

The next regime corresponds to a smaller inertia of the phase coordinate, such, that $\sqrt{8E_J E_C} > 2\pi^2 E_L^\Sigma$, and $\exp(-\sqrt{8E_J/E_C}) \ll 1$. Then, the fluxon states dominate the low-energy spectrum (Fig. 3-1-A,D) and the inter-well tunneling is weak (or the quantum phase-slip amplitude via the black-sheep junction is small), and so the phase-slip language efficiently describes the lowest transitions.

The extreme limit of very large E_C (vanishing inertia) corresponds again to a harmonic low-energy spectrum, but this time with the transition energy is $\sqrt{8E_L E_C}$. The equivalent particle is so light that it does not feel the potential barriers of the fluxon wells and eventually undergoes bound motion due to the parabolic part of the potential given by the array inductance L . This regime starts when the parameter $\sqrt{E_J/E_C} < 1$ (Fig. 3-1-J). Although this qubit regime presents an attractive energy spectrum, easily tunable over several GHz frequency range, but essentially insensitive to practical levels of flux noise, it suffers from one serious disadvantage. The vibrations in the LC oscillator involve the flux motion of order Φ_0 (superinductance!), which results in a strong coupling of the $g \leftrightarrow e$ transition to the outside world (dissipation!).

The fluxonium qubit regime, at least that considered in the present thesis, corresponds to a special choice of parameters, similar to that used for the Fig. 3-1-J. In this regime, the

lowest energy $g \leftrightarrow e$ transition still retains its fluxon character. On the contrary, the next transition $g \leftrightarrow f$ corresponds to a strong hybridization between plasmons and fluxons. This requires the approximate balance $\sqrt{8E_J E_C} \simeq 2\pi^2 E_L^\Sigma$ and a certain range of the quantum phase-slip energies E_{SB} (recall formula 1.16), such that $E_{SB}/8E_J E_C \approx \exp(-\sqrt{8E_J/E_C}) \in [10^{-3}, 10^{-1}]$. The key interests of this regime to our experiments are: (i) the multi-octave frequency range of the fluxon-like $g \leftrightarrow e$ from nearly zero (actually E_{SB}/h) to the value of approximately $2\pi^2 E_L^\Sigma/h$; (ii) the suppressed transition matrix elements (Fig. 3-2-A, dotted red lines) leading to weaker energy relaxation and longer life-times; (iii) options to read the weakly coupled $g \leftrightarrow e$ transitions using strong coupled (due to the plasmon nature of the f level) $g \leftrightarrow f$ and/or $e \leftrightarrow f$ transitions.

What about the absolute value of E_L and the practical frequency range? Well, an inductance satisfying $L\omega_p \gtrsim R_Q$ calculates to $L \gtrsim 100$ nH or $E_L = (\Phi_0/2\pi)^2/L < 1$ GHz. Then, the maximum $g \leftrightarrow e$ transition frequency (at $\varphi_{\text{ext}} = 0$) is $2\pi^2 \times 1$ GHz = 20 GHz. Therefore, the absolute value of L just entering the superinductance regime naturally lands inside the range of parameters necessary to reach the fluxonium qubit regime.

3.2 Readout

The physical transmission line resonator (Fig. 1-14, Fig. 2-1) appears as two different circuits to the qubit and to the incoming microwaves. While the scattering of microwaves off the resonator takes place as if it is replaced by an effective *series* LCR circuit (see expression 2.1 and Fig. 2-3), by contrast, to the qubit, the resonator appears as a *parallel* effective LCR circuit! The parameters of the parallel circuit are the inductance L_R and the capacitance C_R , or, more relevant to our discussion, the resonance frequency $\nu_0 = \omega_0/2\pi$, $\omega_0 = 1/\sqrt{L_R C_R}$ and the impedance $Z_0 = \sqrt{L_R/C_R}$. The coupling capacitance C_Q sets the quality factor Q of the resonator due to dissipation in the measurement leads. The voltage U across the capacitance C_R could be written in terms of creation and annihilation operators, $U = U_0(a + a^\dagger)$, where U_0 has the physical meaning of the vacuum RMS voltage. The coupling of the qubit to the resonator is given, according to the circuit theory, by the product $-2en \frac{C_c}{C_c + C_J} \times U$, where $2en \frac{C_c}{C_c + C_J}$ is the operator of the displacement charge on the coupling

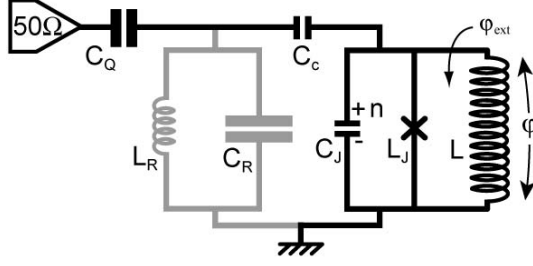


Figure 3-3: Circuit model of the fluxonium-readout resonator interaction. The physical readout resonator (Fig. 2-1) appears to the fluxonium circuit as an $L_R C_R$ -circuit (marked in grey) which is decoupled from the 50Ω line by the capacitance C_Q , resulting in the resonator loaded quality factor Q . The fluxonium circuit, represented by the Josephson inductance L_J , capacitance C_J and the array inductance L , is coupled via the charge operator n , by means of the capacitance $C_c \ll C_J$.

capacitance C_c . Estimating U_0 using Eq. (1.1) we introduce the coupling constant g :

$$g = \frac{C_c}{C_c + C_J} \sqrt{\pi \frac{Z_0}{R_Q}} h\nu_0 \quad (3.10)$$

and the hamiltonian describing the coupled fluxonium and readout:

$$H_{\text{F+R}} = 4E_C n^2 - E_J \cos \varphi + \frac{1}{2} E_L (\varphi - \varphi_{\text{ext}})^2 + h\nu_0 a^\dagger a - gn(a + a^\dagger) + H_{\text{bath}}[a, a^\dagger] \quad (3.11)$$

Here the term $H_{\text{bath}}[a, a^\dagger]$ describes the coupling of the readout degree of freedom to the dissipation, which eventually is responsible for the finite quality factor of the resonator. However, since in practice $Q \gg 1$ we can always treat the dissipation perturbatively. It is interesting to note that the fine structure constant essentially determines g , just as it does in the case of real-atom QED [66]. However in the case of circuits, other coupling schemes exist where the effect of the fine structure constant can even be inverted [67].

The type of coupling $gn(a + a^\dagger)$ between an atomic momentum n and the resonator mode coordinate $a + a^\dagger$ is usually treated in terms of effective Jaynes-Cummings hamiltonian [68, 69]. The atom is usually replaced with an effective spin with the transition frequency ν_{ge} detuned from the readout resonator frequency ν_0 by an amount Δ . The main result of this treatment is that the resonator frequency acquires shifts χ_g and χ_e when the qubit

is prepared in the ground or first excited states. The difference $\Delta\nu_0 = (\chi_e - \chi_g)$ defines the sensitivity of the readout resonator to the qubit state change. At the same time, since the resonator has a finite quality factor, even a purely dissipationless artificial atom will acquire certain finite lifetime, or linewidth κ , due to the energy emission via the resonator, the so-called Purcell effect [70, 62]. For a two-level-like atoms, κ and $\Delta\nu_0$ are very strongly linked, so that the larger the signal the smaller the lifetime. In practice, this link limits the range of qubit frequencies in which the readout works with a reasonable fidelity.

Quite on the contrary, the coupled fluxon-plasmon spectrum of the fluxonium qubit allows to break this unwanted link between κ and $\Delta\nu_0$. In this section, we will treat the coupling of the fluxonium to its readout (Eq. 3.11), entirely within second-order perturbation theory, in a somewhat more transparent way compared to the conventional Jaynes-Cummings approach.

3.2.1 Dispersive shifts by an arbitrary atom

Here we will derive the generic formula for the dispersive shifts of the resonator frequency by an arbitrary multi-level artificial atom. We ignore the term $H_{\text{bath}}[a, a^\dagger]$ and treat the coupling $V = -gn(a + a^\dagger)$ perturbatively in the coupling constant g . Let us label the unperturbed states of the qubit-resonator system as $|\alpha, i\rangle$ or $|\beta, j\rangle$ where $\alpha, \beta = g, e, f, \dots$ denote the number of quanta in the atom and $i, j = 0, 1, 2, \dots$, denote the number of photons in the resonator. The states can be conveniently arranged into the following groups (or ladders) $\{|g, 0\rangle, |e, 0\rangle, |f, 0\rangle, \dots\}$, $\{|g, 1\rangle, |e, 1\rangle, |f, 1\rangle, \dots\}$, $\{|g, 2\rangle, |e, 2\rangle, |f, 2\rangle, \dots\}$, etc., so that each group corresponds to a fixed number of quanta in the resonator. The energy of the state $|\alpha, i\rangle$ is given by $E_{\alpha, i} = E_\alpha + ih\nu_0$. Turning on the interaction causes shifts to every energy level $E_{\alpha, i}$ by $\delta E_{\alpha, i}$. According to second order perturbation theory, the shifts $\delta E_{\alpha, i}$ are given by the expression

$$\delta E_{\alpha, i} = g^2 \sum_{\beta \neq \alpha, j \neq i} \frac{|\langle j|a + a^\dagger|i\rangle|^2 |n_{\alpha\beta}|^2}{E_{\alpha, i} - E_{\beta, j}} \quad (3.12)$$

Each term in the sum (3.12) contributes a shift to the level $|\alpha, i\rangle$ due to its repulsion from the level $|\beta, j\rangle$. Since $a^\dagger|i\rangle = \sqrt{i+1}|i+1\rangle$ and $a|i\rangle = \sqrt{i}|i-1\rangle$, only the levels from the

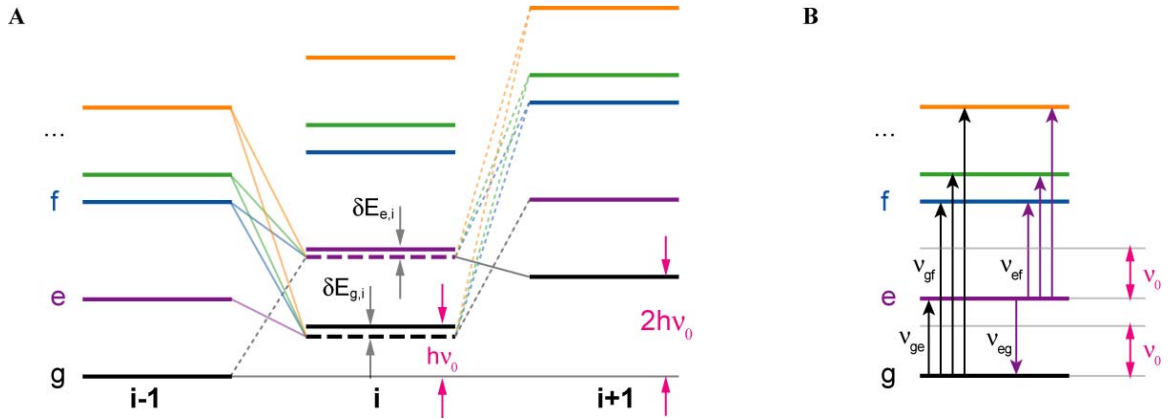


Figure 3-4: Dispersive shifts of the cavity by an atom with an arbitrary spectrum. (A) Interpretation of formula (3.13) using the combined atom-cavity spectrum, arranged into a set of ladders. The three ladders correspond to a fixed number i of quanta in the resonator. Atomic states within each ladder are labeled as g , e , f , ... etc. Only levels from the neighboring ladders can repel each other due to harmonic oscillator selection rules. Repulsion “forces” exerted by the neighbors at the pair of levels (g, i) and (e, i) are indicated with colored lines. Each line corresponds to a term in the sum (3.13). Dashed lines correspond to the weaker terms (“blue” side-bands, or the “counter-rotating” terms) in the expression (3.13). They correspond to the addition of the transition frequency and the resonator frequency in the denominators. (B) Diagrammatic representation of the formula (3.13) for the dispersive shift. Each transition connecting the given atomic state to any other atomic state contributes to the dispersive shift, with the appropriate sign. The contribution is stronger for nearly resonant transitions.

nearest neighbor ladders actually repel each other. The closer the two repelling levels, the stronger the repulsion, due to the energy denominators in (3.12). The expression (3.12) thus drastically simplifies to the following:

$$\delta E_{\alpha,i} = g^2 \sum_{\beta \neq \alpha} \frac{i |n_{\alpha\beta}|^2}{(E_\alpha - E_\beta + h\nu_0)} + g^2 \sum_{\beta \neq \alpha} \frac{(i+1) |n_{\alpha\beta}|^2}{(E_\alpha - E_\beta - h\nu_0)} \quad (3.13)$$

The expression (3.12) has an intuitive interpretation in terms of level repulsion (Fig. 3-4-A). For fixed i , each term in the sum (3.12) comes from the repulsion of level $\{\alpha, i\}$ from level $\{\beta \neq \alpha, i \pm 1\}$. The transitions $\{\alpha, i\} \leftrightarrow \{\beta \neq \alpha, i \pm 1\}$ are called side-bands [71, 72] to the qubit transition $\alpha \leftrightarrow \beta$. The side-band transition frequency could take two types of values: $|\nu_{\alpha\beta} - \nu_0|$ and $|\nu_{\alpha\beta} + \nu_0|$; the former is called the “red” side-band, the latter is called the “blue” side-band, respecting the link between frequency and color. Within the framework of the rotating-wave approximation [69] (RWA), the terms involving blue side-bands are called “counter-rotating” terms and are often neglected when calculating the dispersive shifts. The dispersive shift of the cavity frequency defined as $\chi_\alpha = (E_{\alpha,i+1} - E_{\alpha,i})/h$, does not depend on the occupation of the cavity i to the second order in g . The dispersive shift of the cavity frequency is given only in terms of the charge matrix elements $n_{\alpha\beta}$ and the transition frequencies $\nu_{\alpha\beta} = (E_\alpha - E_\beta)/h$ (the sign is crucial here!):

$$\chi_\alpha = g^2 \sum_{\beta \neq \alpha} |n_{\alpha\beta}|^2 \frac{2\nu_{\alpha\beta}}{\nu_{\alpha\beta}^2 - \nu_0^2} \quad (3.14)$$

This is the most general expression for the dispersive shift of the readout resonator frequency coupled to an arbitrary artificial atom. Every term in the sum (3.14) could be represented as a virtual transition in the atomic spectrum (Fig. 3-4-B). The expression is valid as long as $\chi_\alpha/g \ll 1$. The perturbation theory breaks down whenever expression (3.14) happens to have a pole, $|\nu_{\alpha\beta}| = \nu_0$. This situation corresponds to the vacuum Rabi resonance between the atomic transition $\alpha \leftrightarrow \beta$ and the readout resonator frequency ν_0 . The degeneracy between the two transitions is then lifted by the vacuum Rabi frequency, given by the typical secular perturbation theory expression

$$\Omega_{\alpha\beta} = 2g |n_{\alpha\beta}| \quad (3.15)$$

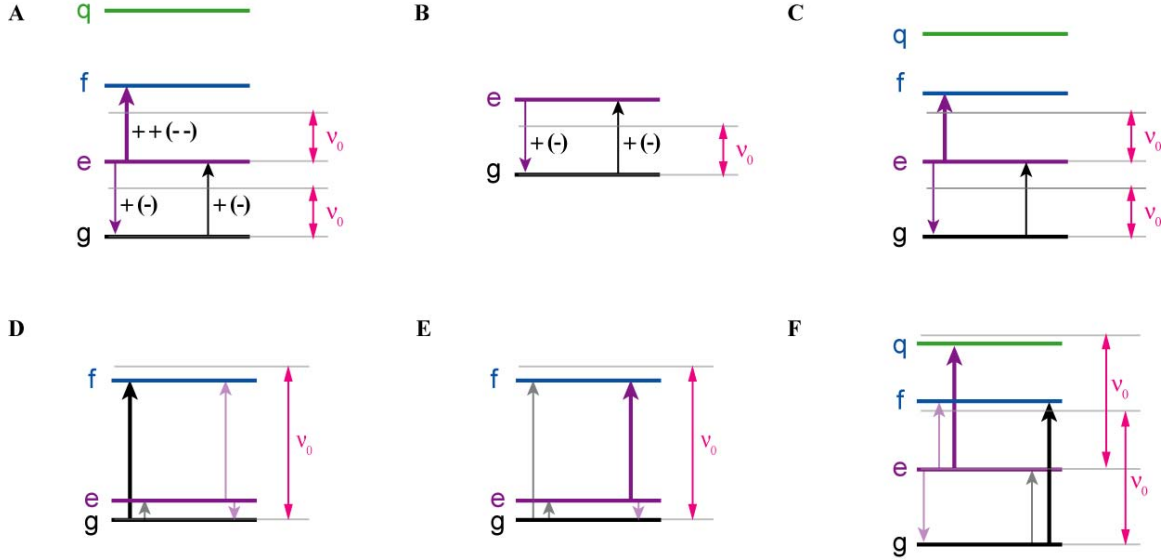


Figure 3-5: Dispersive shifts for several common types of spectra. (A) Harmonic oscillator, shifts cancel to zero exactly (B) Two-level system, the shift reduces as one detunes the qubit from the readout frequency. (C) Transmon, unlike the case of the harmonic oscillator, the cancellation does not take place due to finite anharmonicity. (D) Three-level system with a forbidden transition $e \leftrightarrow f$. The highly detuned $g \leftrightarrow e$ transition produces large dispersive shifts due to the contribution of the $g \leftrightarrow f$ transition, tuned close to the resonance with the readout frequency. (E) Same as (D) but transitions $g \leftrightarrow f$ and $e \leftrightarrow f$ switch roles. (F) Nearly harmonic spectrum, but with allowed transition $g \leftrightarrow f$. Large dispersive shifts appear not only when the transition $g \leftrightarrow e$ is resonant, but also when the transition $g \leftrightarrow f$ is resonant.

Experimentally we usually measure the differential dispersive shift $\chi_{\alpha\beta} = \chi_{\alpha} - \chi_{\beta}$, which is given by:

$$\chi_{\alpha\beta} = g^2 \sum_{\gamma \neq \alpha} |n_{\alpha\beta}|^2 \frac{2\nu_{\alpha\gamma}}{\nu_{\alpha\gamma}^2 - \nu_0^2} - g^2 \sum_{\gamma \neq \beta} |n_{\alpha\gamma}|^2 \frac{2\nu_{\beta\gamma}}{\nu_{\beta\gamma}^2 - \nu_0^2} \quad (3.16)$$

3.2.2 Common examples

Now, let us see how the general formula (3.16) applies to the specific cases of frequently encountered spectra. In general, it is clear that only transitions with large matrix elements and lying sufficiently close to the readout frequency will contribute to the dispersive shift.

Harmonic oscillator

Common sense suggests that for a harmonic spectrum, $\chi_{\alpha\beta} = 0$, otherwise one could use this to measure the Fock states of this oscillator using another oscillator, without employing any non-linearity whatsoever. For a harmonic atom, $\nu_{eg} = \nu_{fe} = \nu$, etc., as well as $n_{ef}^2 = 2n_{ge}^2$, and all the non-nearest neighbor matrix elements are zero. Then we have $\chi_g = 2g^2 n_{ge}^2 \nu / (\nu^2 - \nu_0^2)$ (only one term in the sum) while $\chi_e = -2g^2 n_{ge}^2 \nu / (\nu^2 - \nu_0^2) + 4g^2 n_{ge}^2 \nu / (\nu^2 - \nu_0^2) = \chi_g$ (two terms in the sum), so that $\chi_e - \chi_g = 0$, Q.E.D. (Fig. 3-5-A).

Spin

In the case of a two-level atom with a single transition frequency ν_{eg} , we set α to g and β to e , so the sums in the expression (3.16) contribute single identical terms each, resulting in $\chi_{eg} = \chi = 4g^2 |n_{ge}|^2 \nu / (\nu^2 - \nu_0^2)$ (see Fig. 3-5-B). It is usually fair to assume that $\nu + \nu_0 \approx 2\nu$, the so-called rotating wave approximation, which further simplifies the expression for the dispersive shift to:

$$\chi_{eg} = \frac{2g_{eg}^2}{\nu_{eg} - \nu_0} \quad (3.17)$$

where we have introduced $g_{eg} = g|n_{ge}|$. Note the sign change in χ_{eg} when the qubit transition crosses through the vacuum Rabi resonance with the cavity. It is interesting to note here, that the Purcell effect (see discussion around Eq. 3.30 and Eq. 3.36 later in the text) results in the qubit acquiring a finite lifetime due to spontaneous emission into the measurement apparatus via the cavity filter, with the lorentzian frequency dependence, $T_{\text{Purcell}}^{-1} \propto 1/(\nu_{eg} - \nu_0)^2$. Therefore, the Purcell-induced relaxation reduces with the detuning $\nu_{eg} - \nu_0$ faster than the dispersive shift, allowing a parametric compromise for optimal fidelity. This situation applies to the cases of a Cooper pair box qubit in the charging regime and a flux-qubit.

Transmon

The transmon qubit has a weakly anharmonic spectrum with the following properties: $n_{ef} = \sqrt{2}n_{ge}$, all other matrix elements being either exactly or approximately zero, similar to the

case of a harmonic oscillator. However, there is a finite anharmonicity, $\nu_{fe} - \nu_{eg} \approx -E_C/h \ll \nu_{eg}$ (E_C is the charging energy of the transmon). Then there is again only one term in the sum (3.14) for χ_g but two terms for χ_e [73], with the result (Fig. 3-5-C):

$$\chi_{eg} = 4g_{eg}^2 \frac{E_C/h}{\nu_{eg}^2 - \nu_0^2} \approx \frac{2g_{eg}^2}{\Delta} \frac{E_C/h}{\nu_{eg}} \quad (3.18)$$

The compromise between the magnitude of the dispersive shift and the Purcell-induced relaxation is harder to reach in the case of the transmon, because the higher levels tend to suppress the dispersive shift compared to the two-level system with equivalent coupling constant (assuming large detuning $\Delta \gg g/h$, E_C/h). This is not a surprise - transmon is close to a harmonic oscillator, so χ_{eg} must be suppressed by the small parameter $E_C/h\nu_{eg}$.

Three-level atom

An atom with a spectrum which is neither two-level nor a semi-harmonic may offer an attractive way to measure dispersively with a negligible Purcell effect (Fig. 3-5-D, E). For that, we need a qubit transition to be sufficiently detuned down from the cavity frequency, and yet a sizable amount of dispersive shift χ_{eg} . Clearly, the $g \leftrightarrow e$ transition alone cannot contribute to χ_{eg} due to the large energy denominator. However, the proper choice of the readout frequency may add a large contribution from the transitions $g \leftrightarrow f$ or $e \leftrightarrow f$. In general, every transition with non-zero matrix element may contribute. The answer is particularly illuminating if, due to some difference in the symmetry of the states, $n_{eg} \approx 0$, and $n_{ef} \ll n_{gf}$, so that

$$\chi_{eg} = -g^2 |n_{gf}|^2 \frac{2|\nu_{gf}|}{\nu_{gf}^2 - \nu_0^2} \quad (3.19)$$

In this expression, remarkably, the dispersive shift of the qubit transition between the lowest states g and e is given entirely by the properties of another transition, connecting states g and f , which could be vastly detuned from the qubit transition.

Phase qubit

The phase qubit differs from the transmon by the non-zero matrix element n_{gf} due to the asymmetry of the washboard potential well. Provided that this asymmetry is sufficiently strong, one could play the following trick to measure dispersively without Purcell effect. Let's choose the readout frequency to be around twice the qubit frequency, more precisely, $\nu_0 = 2\nu_{fe}$. Then two new terms contribute to the expression for χ_{eg} compared to the regular transmon case (Fig. 3-5-F). The final expression would be (we will have to introduce the 4-th qubit state q)

$$\chi_{eg} = 2g^2 \left(\frac{|n_{eg}|^2}{\nu_{eg} - \nu_0} \frac{E_C/h}{\nu_{eg}} + |n_{fg}|^2 \frac{\nu_{fg}}{\nu_{fg}^2 - \nu_0^2} - |n_{qe}|^2 \frac{\nu_{qe}}{\nu_{qe}^2 - \nu_0^2} \right) \quad (3.20)$$

The first term of this expression would be weak because we choose $|\nu_{eg} - \nu_0| \simeq \nu_{eg}$. However, the denominators of the second two terms could be chosen to be of order $(E_C/h)\nu_{fg}$, a situation reminiscent the so-called straddling regime of the transmon but at twice the qubit frequency. For the optimal readout frequency choice of $\nu_0 = 2\nu_{fe}$, we get

$$\chi_{eg}^{\max} = 2 \frac{g^2}{E_C/h} \left(-|n_{eg}|^2 \left(\frac{E_C/h}{\nu_{eg}} \right)^2 + |n_{fg}|^2 + |n_{qe}|^2 \right) \quad (3.21)$$

3.2.3 Dispersive shifts by fluxonium circuit

In order to investigate the dispersive shifts of a fluxonium circuit it is more convenient to change the labeling of the atomic states from letters to numbers, $\{e, g, f, \dots\} \rightarrow \{0, 1, 2, \dots\}$. This is because far more than two states contribute to the shift. We examine the dispersive shifts by the fluxonium qubit for the two sets of parameters, $\{E_L = 0.5, E_J = 20, E_C = 2.5\}$ (see Fig. 3-1-D,E,F), characteristic of the phase-slip regime, and $\{E_L = 0.5, E_J = 10, E_C = 2.5\}$ (see Fig. 3-1-G,H,I), characteristic of the fluxonium qubit regime, as well as several values of the readout frequency ν_0 .

Phase-slip regime

Deep in the phase-slip regime the origin of the dispersive shifts may be understood from the following qualitative picture. For $E_L \ll E_J$ (our usual condition) and $\exp(-\sqrt{8E_J/E_C}) \ll$

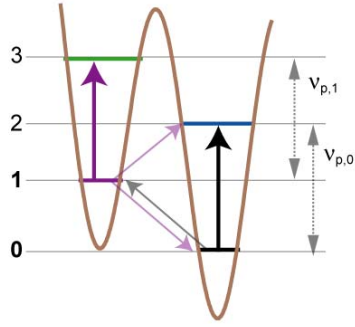


Figure 3-6: Origin of dispersive shift by the fluxonium circuit, phase-slip regime. The two neighboring fluxon wells (Fig. 3-1-F) each host a ladder of plasmon states (only two states in each ladder in this case). The ground state of the right ladder is the ground state of the entire circuit, corresponding to zero fluxons in the loop. The ground state of the left ladder is the second excited state of the entire circuit. Interwell transitions ($0 \leftrightarrow 1$ and $1 \leftrightarrow 2$, faint arrows) contribute negligibly to the dispersive shift (3.16), while the plasmon transitions ($0 \leftrightarrow 2$ and $1 \leftrightarrow 3$, thick arrows) contribute dominantly. The frequency of the plasmon vibrations in the left well $\nu_{p,1}$ is slightly lower than that, $\nu_{p,0}$, in the right well, due to finite value of E_L/E_J . This difference in the plasma frequencies in the two fluxon wells eventually yields a finite dispersive shift χ_{01} for the qubit transition (see Eq. 3.23), provided that the readout frequency is chosen to be close to the plasmon frequency (see Eq. (3.25) and Eq. (3.24)). Importantly, in contrast to the case of either spin or transmon qubits, this mechanism of dispersive shift makes the latter to be independent of the properties of the qubit transition.

1, the plasmon and fluxon levels are clearly separated in the spectrum (Fig. 3-1-D,E,F; Fig. 3-6). The plasmon frequency is given by the curvature of the fluxon well. This curvature is approximately given by L_J , but has some weak dependence on the fluxon well number. By employing standard differential analysis, one can calculate that the curvature of the second minimum of the potential in the hamiltonian (3.1) differs from L_J by a fraction of order $\beta_L^{-1} = L_J/L$ [64]. Therefore, while the plasma vibration in the zero fluxon state takes place at the frequency $\nu_{p,0} \simeq \sqrt{8E_J E_C}$, the vibration in the excited fluxon state takes place at a slightly smaller frequency $\nu_{p,1} < \nu_{p,0}$, given by

$$\nu_{p,1} \simeq \nu_{p,0} \left(1 - \frac{L_J}{L}\right) \simeq \nu_{p,0} - E_L \sqrt{8E_C/E_J} \quad (3.22)$$

Given the weakness of the inter-well transition matrix elements, as well as the harmonic oscillator selection rules, only two terms contribute to the dispersive shift χ_{eg} (even if each fluxon well contains a large number of plasma states):

$$\chi_{01} = 2g^2 \left(\frac{\nu_{p,0} |n_{02}|^2}{\nu_{p,0}^2 - \nu_0^2} - \frac{\nu_{p,1} |n_{13}|^2}{\nu_{p,0}^2 - \nu_0^2} \right) \quad (3.23)$$

Now, taking into account the relation (3.22), and also the fact that $|n_{02}|^2 \simeq |n_{13}|^2 \simeq (E_J/8E_C)^{1/2}$ (harmonic oscillator approximation [73]), we get two simple expressions for the dispersive shift, depending on the choice of the readout frequency ν_0 . The largest shift takes place when $\nu_{p,1} < \nu_0 < \nu_{p,0}$, so that the transitions $0 \rightarrow 2$ and $1 \rightarrow 3$ contribute to the dispersive shift with equal signs (straddling regime again!), and we get

$$\chi_{01} = \frac{1}{4} \frac{g^2}{E_C} E_J/E_L \quad (3.24)$$

We remind the reader again that this formula is only valid when $\chi_{01} \ll g$. In the case of some detuning of the readout frequency from the plasmon frequency, $|\nu_0 - \nu_{p,0}| > E_L \sqrt{8E_C/E_J}$, we get a transmon-like [73] expression

$$\chi_{01} = \frac{g^2}{\nu_{p,0} - \nu_0} \times \sqrt{\frac{8E_C}{E_J}} \frac{1}{\beta_L} \quad (3.25)$$

in which the quantity $\sqrt{\frac{8E_C}{E_J}} \frac{1}{\beta_L}$ plays the role of the transmon anharmonicity. Note, however,

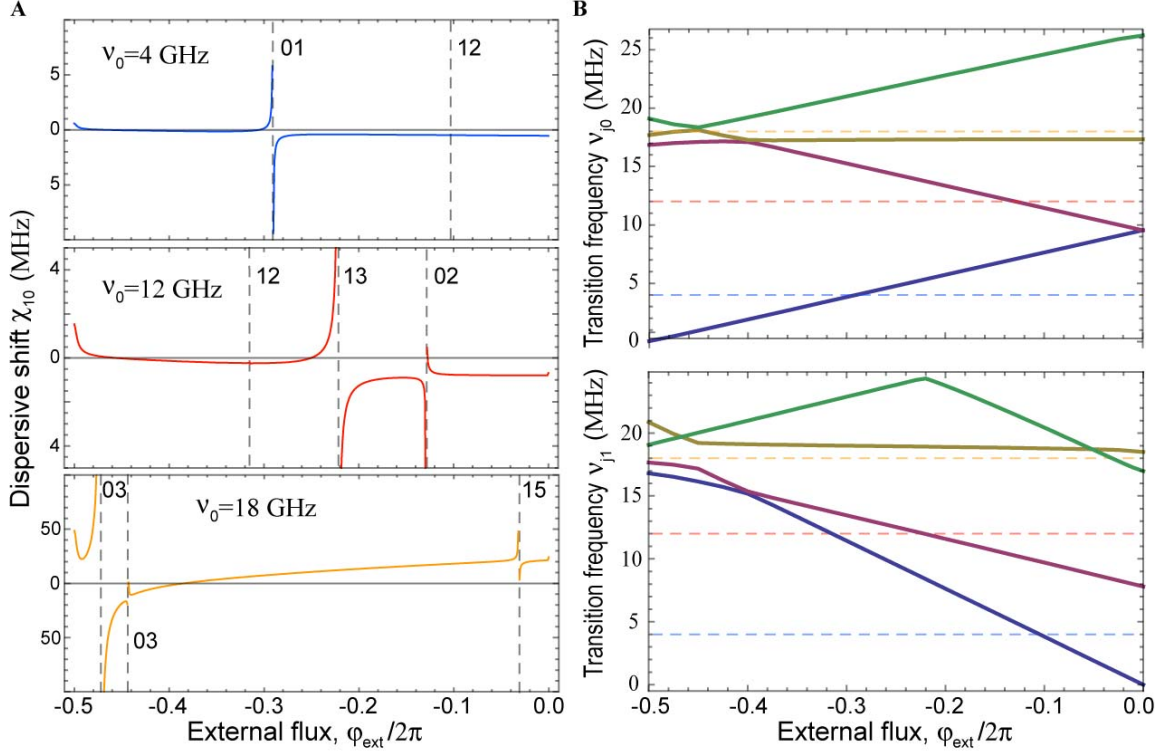


Figure 3-7: Numerically computed dispersive shifts, phase-slip regime. The choice of parameters is the same as in Fig. (3-1-D,E,F). (A) Dispersive shifts for the three values of the readout frequency, top to bottom $\nu_0 = 4, 12,$ and 18 . Vacuum Rabi resonances indicated with vertical dashed lines. (B) Transition spectrum from ground state (top graph) and from the first excited state (bottom graph). Location of the vacuum Rabi resonances in the qubit dispersive shifts correspond to the crossing of the transitions connecting either qubit states with the readout frequency (blue, red and orange faint dashed lines). Note how $\nu_0 = 12$ GHz lies between the $0 \leftrightarrow 3$ and $1 \leftrightarrow 4$, satisfying the straddling condition (see Eq. 3.25).

that unlike the transmon case, here the dispersive shift χ_{01} essentially depends on neither the flux or the qubit transition frequency ν_{01} . A proper choice of cavity frequency ν_0 would guarantee the visibility of the $g \rightarrow e$ transition in the entire multi-octave frequency range. Note also that the estimates (3.25 and 3.24) fail near the sweet-spots $\varphi_{\text{ext}} = 0, \pi$, where the fluxon transitions become degenerate and the selection rules for the matrix elements apply. For instance, the increase in χ_{01} towards $\varphi_{\text{ext}} = \pi$, happens because $n_{02}(\pi) = 0$ there due to the parity conservation and $n_{12}(\pi)$ sharply takes the maximum value.

Turning to numerical analysis, we compute the dispersive shifts $\chi_{eg}(\varphi_{\text{ext}})$ using the tran-

sition spectrum (Fig. 3-1), the matrix elements (Fig. 3-2) and our general expression (3.16). We choose three readout frequencies, $\nu_0 = 4, 12, \text{ and } 18$ GHz. The results of the numerics for χ_{01} in the case of the deep phase-slip regime, $\{E_L = 0.5, E_J = 20, E_C = 2.5\}$ are summarized in Fig. (3-7). Each time either the transition frequency ν_{j0} or ν_{j1} ($j = 0, 1, 2, \dots$) crosses ν_0 , we get a corresponding vacuum Rabi resonance in the dispersive shift. The stronger the corresponding matrix element $|n_{0j}|$ or $|n_{1j}|$, the broader the resonance. Quantitative values of the dispersive shifts cannot be trusted if they are not much smaller than the coupling constant g .

The readout frequency $\nu_0 = 4$ GHz corresponds to two resonances, the $0 \leftrightarrow 1$ and $1 \leftrightarrow 2$. The resonance $1 \leftrightarrow 2$ is so narrow, that it cannot even be resolved, because of the extremely small matrix element $|n_{12}|$. Due to the large (compared to g) detuning between the plasmon frequency and the readout frequency, the dispersive shift is tiny away from the vacuum Rabi resonances. The readout frequency $\nu_0 = 8$ GHz crosses transitions $1 \leftrightarrow 3$ and $0 \leftrightarrow 2$ with stronger matrix elements, so the corresponding vacuum Rabi resonances are wider. Since $\nu_0 = 8$ GHz is closer to the plasmon frequency, the dispersive shift in between the resonances is larger than in the case $\nu_0 = 4$ GHz and is indeed weakly dependent on the external flux, just as the qualitative formula (3.25) predicts. The choice of readout frequency $\nu_0 = 12$ GHz satisfies the ‘‘straddling’’ condition $\nu_{p,1} < \nu_0 < \nu_{p,0}$, and leads to very large dispersive shift of order $g/10$. Note, how the competition between different transitions can lead to strictly zero dispersive shifts for certain values of external flux.

Fluxonium qubit regime

In this regime of circuit parameters $\{E_L = 0.5, E_J = 10, E_C = 2.5\}$ (Fig. 3-1-G,H,I) the best way to intuitively understand the dispersive shift, is to approximate the spectrum with a three-level system, in which the ground and first excited states are fluxon-like while the third state is plasmon-like state (Fig. 3-8). In this model, only one plasmon transition is present, which provides the dominant contribution to the dispersive shift. An approximate expression for the dispersive shift then will be

$$\chi_{01} \sim -\frac{g^2}{\nu_{02} - \nu_0} |n_{02}|^2 + \frac{g^2}{\nu_{12} - \nu_0} |n_{12}|^2 \quad (3.26)$$

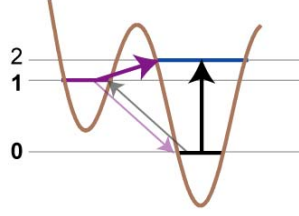


Figure 3-8: Origin of dispersive shift by the fluxonium circuit, fluxonium qubit regime. The lowest transition from the ground state corresponds to the excitation of a fluxon, which is still fairly well localized in its respective fluxon well, while the second transition from the ground state corresponds to a plasmon, which is fairly well spread between the two wells. Therefore, the direct $0 \leftrightarrow 1$ transition is still negligible (faint lines), so the dispersive shift is determined by the competition between the intense transitions $1 \leftrightarrow 2$ and $0 \leftrightarrow 2$ (Eq. 3.26).

which clearly can be quite large with the proper choice of ν_0 even when $\nu_{01} \ll \nu_0$. The behavior of the matrix elements could be seen from the Fig. (3-2, red dotted lines) and the discussion in the corresponding section.

Numerically, we try the set of three frequencies $\nu_0 = 4, 8,$ and 12 GHz. The vacuum Rabi resonances here are stronger than in the phase-slip regime, due to larger charge matrix elements. For low readout frequency, $\nu_0 = 4$ GHz, the vacuum Rabi resonances $1 \leftrightarrow 2$ and $1 \leftrightarrow 3$ contribute as much as the conventional $0 \leftrightarrow 1$ resonance. Moving the frequency closer toward the plasmon frequency, by setting $\nu_0 = 8$ GHz, changes the vacuum Rabi resonance pattern, but in general produces a larger shift, in accord with our estimate (3.26). Finally, the case of $\nu_0 = 12$ GHz shows even stronger resonances and larger shifts, with the level number as high as 5 contributing. These analyses confirm that choosing the readout close to the plasmon frequency guarantees large dispersive shift for the $0 \leftrightarrow 1$ fluxon transition in the fluxonium qubit regime. Just as in the case of the phase-slip regime, the interference between different vacuum Rabi resonances results in a large number of nulls in the dispersive shift as a function of flux. Nevertheless, the qubit transition is, on average, equally well visible in the entire frequency range from nearly zero frequency to as high as $2\pi^2 E_L/h$.

3.2.4 Spurious resonances

The hamiltonian (3.11) equally well describes the coupling of the fluxonium to any other non-readout degrees of freedom – spurious modes of the electromagnetic environment of the

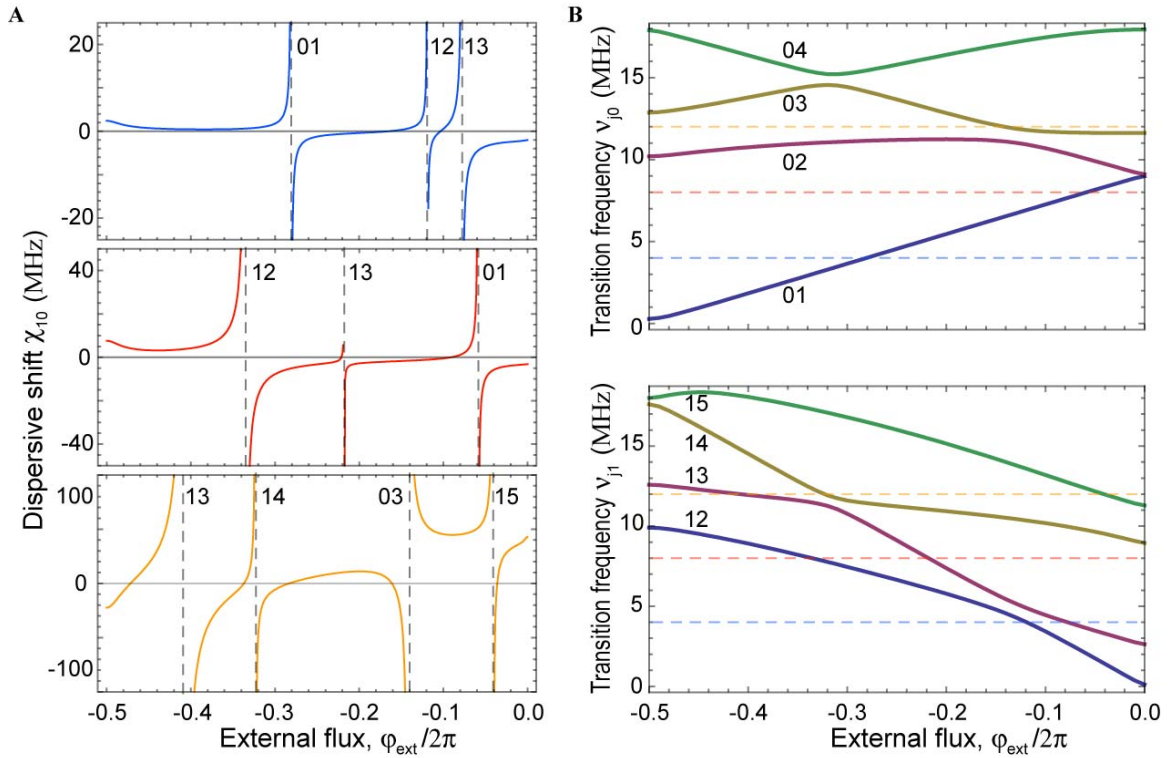


Figure 3-9: Numerically computed dispersive shifts, the fluxonium qubit regime. The choice of parameters is the same as in Fig. (3-1-G,H,I). (A) Dispersive shifts for the three values of the readout frequency, top to bottom $\nu_0 = 4, 8,$ and 12 . Vacuum Rabi resonances indicated with vertical dashed lines. (B) Transition spectrum from ground state (top graph) and from the first excited state (bottom graph). Location of the vacuum Rabi resonances in the qubit dispersive shifts correspond to the crossing of the transitions connecting either qubit states with the readout frequency (blue, red and orange faint dashed lines).

circuit or impurities in the oxide of the Josephson junctions, to name a couple. The linear interaction of the fluxonium with these spurious modes could be described by the following generalization of the hamiltonian (3.11):

$$H_{\text{sp}} = \sum_k \left(\hbar\nu_k a_k^\dagger a_k + g_k^{\{n\}} (a_k^\dagger + a_k)n + g_k^{\{\varphi\}} i(a_k^\dagger - a_k)\varphi \right) \quad (3.27)$$

where the operator a_k is the lowering ladder operator for the k -th mode, which could be either a spin or a harmonic oscillator. The coupling constants $g_k^{\{\varphi\}}$ and $g_k^{\{n\}}$ would depend on the details of the coupling, usually in a way that only one constant out of the two can be non-zero, for a given mode k . For instance, in the case of capacitive coupling to the readout resonator (Fig. 3-3) $g_k^{\{\varphi\}} = 0$ and $g_k^{\{n\}} = g$ and is given by expression (3.10). Irrespective of the details of coupling, the effect of the spurious modes on the spectrum of the fluxonium is qualitatively the same as that of the readout. The spectroscopy will reveal the vacuum Rabi resonances between the fluxonium transitions and the spurious modes, as well as the blue and red side-band transitions and so on. The brightness of these new features in the spectrum will depend on the values of the coupling constants and the matrix elements of n and φ .

3.3 Decoherence

In a spectroscopy experiment, every qubit resonance has a finite width in frequency. This width appears either from the finite lifetime of the qubit excited state, a process called spontaneous emission (or energy relaxation), or because the circuit parameters defining the transition frequency fluctuate in time, on the time scale faster than the time of the experiment, a process called dephasing.

3.3.1 Spontaneous emission

The energy relaxation of the fluxonium circuit comes from the coupling of either its charge n or phase φ operator to a bath capable of dissipating an electromagnetic wave at the frequency of the qubit transition. Irrespective of the microscopic origin of the bath, its effect on the qubit can be modelled as a frequency-dependent resistance. The coupling

to the the charge n is represented by replacing the readout resonator in Fig. (3-3) with a resistance R . The perturbation to the circuit hamiltonian due to the coupling to this resistance is given by $V = -4E_C n C_c U_R = \frac{C_c}{C_J + C_c} 2enU_R$, where U_R is the voltage operator across the resistance. The rate of energy loss resulting in the qubit transition $\alpha \rightarrow \beta$ is given by the generic Fermi's Golden Rule expression [44]

$$\Gamma_{\alpha\beta} = \frac{1}{(\Phi_0/2\pi)^2} \left(\frac{C_c}{C_J + C_c} \right)^2 |\langle \alpha | n | \beta \rangle|^2 S_{U_R}(\omega_{\alpha\beta}) \quad (3.28)$$

in which the spectral density of the voltage quantum noise $S_{U_R}(\omega)$, defined as $S_{U_R}(\omega) = \int dt \langle U_R(t) U_R(0) \rangle \exp(i\omega t)$ (the average $\langle \dots \rangle$ is taken over the ground state of the resistor R) is given by

$$S_{U_R}(\omega) = R\hbar\omega \left(1 + \coth \left(\frac{\hbar\omega}{2k_B T} \right) \right) \quad (3.29)$$

resulting in the final expression for the energy relaxation rate

$$\Gamma_{\alpha\beta}(\nu_{\alpha\beta}) = (2\pi)^2 \left(\frac{C_c}{C_J + C_c} \right)^2 \frac{R}{R_Q} |n_{\alpha\beta}|^2 \nu_{\alpha\beta} \left(1 + \coth \left(\frac{\hbar\nu_{\alpha\beta}}{2k_B T} \right) \right) \quad (3.30)$$

This expression is valid as long as $\Gamma_{\alpha\beta} \ll \nu_{\alpha\beta} \equiv \omega_{\alpha\beta}/2\pi$, which is easily satisfied if $C_c \ll C_J$, or $R \ll R_Q$, or if the transition is naturally weak, i.e. $|n_{\alpha\beta}| \ll 1$.

It is interesting to look at the alternative way of coupling of the fluxonium to the resistor R , by treating the series combination of R and the coupling capacitance C as an admittance $Y(\nu) = (R + (i2\pi\nu C_c)^{-1})^{-1}$, directly shunting the black-sheep junction. Then the coupling hamiltonian is given by $\tilde{V} = -(\Phi_0/2\pi)\varphi I_Y$, where I_Y is the operator of the current noise generated in the admittance Y . The Fermi's golden rule expression for the relaxation rate is now:

$$\Gamma_{\alpha\beta} = \frac{1}{(2e)^2} |\varphi_{\alpha\beta}|^2 S_{I_Y}(\omega_{\alpha\beta}) \quad (3.31)$$

The spectral density $S_{I_Y}(\nu)$ of the current noise in the admittance Y is given by

$$S_{I_Y}(\omega) = 2\text{Re}[Y(\omega)]\hbar\omega \coth \left(\frac{\hbar\omega}{2k_B T} \right) \quad (3.32)$$

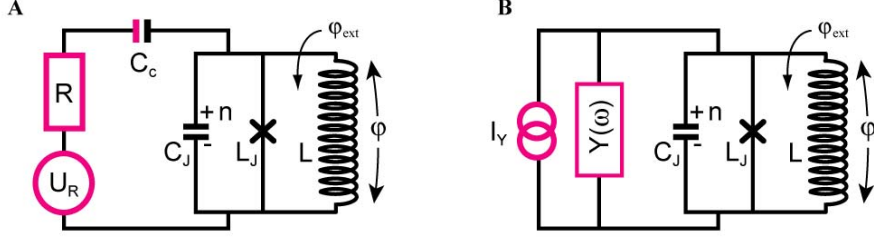


Figure 3-10: Two models of spontaneous emission. (A) The fluxonium charge operator n couples to the fluctuating voltage U_R across a resistance R via a series capacitance C_c . (B) The fluxonium phase operator φ couples to the fluctuating current I_Y in an admittance $Y(\omega)$ directly shunting the junction.

Taking into account that $\text{Re}[Y(\omega)] = \frac{1}{R} \frac{(\omega RC_c)^2}{1 + (\omega RC_c)^2} \simeq (\omega RC_c)^2 / R$ for sufficiently small R or C_c , we get the following final expression for the relaxation rate:

$$\Gamma_{\alpha\beta} = (2\pi)^2 (\nu_{\alpha\beta} R_Q C_c)^2 \frac{R_Q}{R} |\varphi_{\alpha\beta}|^2 \nu_{\alpha\beta} \left(1 + \coth \left(\frac{h\nu_{\alpha\beta}}{2k_B T} \right) \right) \quad (3.33)$$

Now an important remark is in order. The two expressions (3.30) and (3.33) must give identical relaxation rates, which could only be satisfied if $|n_{\alpha\beta}|^2 = |\varphi_{\alpha\beta}|^2 (\nu_{\alpha\beta} R_Q C_J)^2$ (assuming $C_c \ll C_J$). The reasoning above is a proof by the circuit theory of the formula (3.8), which links the matrix elements of the phase φ and its conjugate reduced charge n of an arbitrary non-linear oscillator circuit. Note, that formula (3.8) is nothing else than a manifestation of the fact that the phase φ and the reduced charge n are conjugate variables, like position x and momentum p of a particle with a mass m described by a hamiltonian $H(x, p)$. Indeed, since $p = m\dot{x}$ we have $p_{\alpha\beta} = m \langle \alpha | \frac{i}{\hbar} [H, x] | \beta \rangle = im2\pi\nu_{\alpha\beta} \times x_{\alpha\beta}$, where $\nu_{\alpha\beta} = (H_{\alpha\alpha} - H_{\beta\beta})/h$ is the transition frequency between the eigenstates α and β . Similarly, given that $n = (C_J R_Q / 2\pi) \times \dot{\varphi}$ (capacitance plays the role of mass) we arrive at formula (3.8).

In analyzing the relaxation of the fluxonium qubit, we prefer to use the admittance representation and the resulting formula (3.31). Any linear dissipation source which is coupled to the fluxonium device could be represented as an admittance shunting the junction. More generally, the linear dissipation sources coupled to the junctions of the fluxonium could be represented as admittances shunting the junctions.

3.3.2 Emission into measurement apparatus

Here we calculate the relaxation rate due to the coupling of the fluxonium to the 50 Ω dissipation via the readout resonator. The classical version of our analysis was performed in the past in Ref. [62] for the case of the transmon qubit. This source of dissipation corresponds to shunting the black-sheep junction with the admittance

$$Y_{\text{Purcell}}(\omega) = \left(\left(\left(iZ_{\infty} \tan \frac{\pi}{2} \frac{\omega}{\omega_0^{\text{geom}}} \right)^{-1} + (R + (i\omega C_Q)^{-1})^{-1} \right)^{-1} + (i\omega C_c)^{-1} \right)^{-1} \quad (3.34)$$

where the $R = 100 \Omega$ comes from the two coaxial lines differentially driving the balanced coplanar strips type readout resonator (Fig. 2-2, Fig. 2-3) and ω_0^{geom} is the resonance frequency associated with the geometric length of the transmission line. The resonator contribution (the Z_{∞} -term) comes directly from the formula (1.2). The function (3.34) has a pole at the frequency of the fundamental resonance $\omega_0 = \omega_0^{\text{geom}} (1 - \frac{2}{\pi} Z_{\infty} (C_Q + C_c) \omega_0^{\text{geom}}) \approx \omega_0^{\text{geom}}$, with the quality factor Q given by

$$Q = \frac{4}{\pi} / Z_{\infty} R (\omega_0 C_Q)^2 \quad (3.35)$$

Assuming that $Q \gg 1$, we can find the simplified expression for $\text{Re}[Y(\omega)]$:

$$R_{\text{Purcell}}^{-1}(\omega) \equiv \text{Re}[Y(\omega)] = Z_{\infty}^{-1} \frac{(\omega Z_{\infty} C_c)^2}{Q} \times \frac{\pi}{4} (\omega/\omega_0)^2 \tan^2\left(\frac{\pi}{2} \omega/\omega_0\right) \quad (3.36)$$

The life-time T_1^{eg} of the ground to first excited state transition $g \leftrightarrow e$ can then be calculated using the formula (3.33) by substituting R with R_{Purcell}^{-1} .

For a fixed Q and ω , one can increase T_1^{eg} by making the matrix element $|\varphi_{eg}|$ small. Unfortunately, for transmons and two-level qubits, this is not an option because the same matrix elements n_{eg} and φ_{eg} determine the magnitude of the dispersive shift. On the contrary, the dispersive shifts of fluxonium are determined by the transitions other than $g \leftrightarrow e$ so choosing the qubit parameters such that $|\varphi_{eg}| \rightarrow 0$ is quite an option. Furthermore, choosing a small value of the coupling capacitance helps to reduce R_{Purcell}^{-1} : for $C_c = 1$ fF (value compatible with the Cooper-pair box device), $Z_{\infty} = 100 \Omega$ and $\omega = 2\pi \times 10^{10}$ GHz,

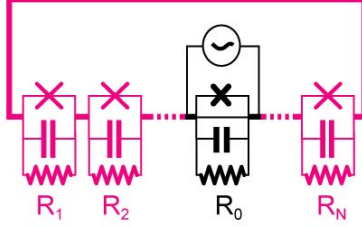


Figure 3-11: Fir-tree garland model of intrinsic dissipation in fluxonium array junctions. Phase-slip event across the black-sheep junction could be represented as a voltage source generating a voltage spike with total flux Φ_0 . Each of the array junctions experiences only a fraction $1/N$ of the voltage across the black-sheep.

the prefactor $Z_\infty^{-1} \frac{(\omega Z_\infty C_c)^2}{Q_{\text{ext}}}$ calculates to about 1 G Ω . This is to be contrasted with a typical transmon qubit, in which $C_c \propto 20$ fF, so the Purcell resistance is a factor of 400 smaller (with similar numerical values of the coupling constant g , see Eq. (3.10))!

3.3.3 Intrinsic dissipation and the garland effect

Now lets us turn to the effects of intrinsic dissipation. Every junction of the array suffers from intrinsic, generally unknown, dissipation sources, all lumped into a frequency-dependent resistance R_j shunting the j -th junction. Given the fact that (away from $\varphi_{\text{ext}} = 1/2$) the transition energy is shared equally by all of the $N = 43$ array junctions, and that junctions with similar area of order $1\mu\text{m}^2$ are reportedly lossy, the issue of dissipation appears crucial. Nevertheless, a simple classical reasoning establishes that the dissipation in the black sheep solely dominates the intrinsic relaxation of the fluxonium transitions with the contribution from array junctions being suppressed as $1/N$. Indeed, the dominant phase-slip process (or even the simple plasmon vibrations) generates a voltage pulse across the black sheep; each array junction receives only a $1/N$ portion of that voltage, and the total energy dissipated in the array resistors is only $1/N$ of that dissipated in the black sheep junction. We can therefore express the effective resistance $R_{\text{intrinsic}}$ entering the formula (3.33) through the effective shunting resistances of the junctions:

$$R_{\text{intrinsic}}^{-1} = R_0^{-1} + \left(\sum_{j=1}^N R_j \right)^{-1} \quad (3.37)$$

Since the area of the black-sheep junction is only a factor of 6 – 7 smaller than that of the array junctions, and assuming that R^{-1} is proportional to the area, it is likely that $R_{\text{intrinsic}} \approx R_0$, so for large N , only the black-sheep junction contributes. For exactly the same reason, adding extra light bulbs in series with a fir-tree garland reduces its total brightness. We thus conclude that the apparent multi-junction complexity of the fluxonium circuit remarkably does not a priori penalize it with enhanced energy relaxation.

In the case of lossy array junctions, calculating the effect of quantum phase-slip in the array inductance on the dissipation in the fluxonium goes beyond the scope of this work. We believe that for our parameter choice, for which the probability of a phase-slip in the array junctions is much smaller than that in the black-sheep junction, there is no observable contribution to the dissipation.

3.3.4 Dephasing: common mechanisms

Here we estimate the dephasing times from the most common sources of noise in superconducting qubits. For the purpose of our discussion, it is sufficient to treat dephasing as some kind of inhomogeneous broadening phenomenon. More rigorous analysis of noise can be adopted from the past work[74].

Thermal photons in the resonator

Just like with any other superconducting qubit in a cavity, fluxonium transitions acquire linewidth due to the thermal occupation of the readout resonator. We have already seen that the energy of the qubit when there are exactly n photons in the resonator is proportional to n (3.13). Therefore, fluctuating photon number results in fluctuating qubit frequency, or, equivalently, in a finite dephasing time. The physical interpretation of this dephasing time is that the thermal photons perform a measurement of the dispersive shift, similarly to the action of the coherent photons, which we populate the cavity with during a readout pulse. Therefore, according to the uncertainty principle, thermal photons must dephase the qubit transition.

At low enough temperatures we have $n \ll 1$ and it is safe to assume that thermal photons perform a measurement of the qubit state at a rate much slower than the cavity

lifetime $1/\kappa$, in which case the fluctuations of the qubit frequency $\delta\nu_{\alpha\beta}$ can be estimated as [23]

$$\delta\nu_{\alpha\beta} \simeq (\chi_{\alpha\beta}/\kappa)^2 \kappa \times n \propto \exp(-h\nu_0/k_B T) \quad (3.38)$$

For the typical parameters, $\chi_{eg} \approx 1-10$ MHz, $\kappa \simeq 10$ MHz, so to make sure that the thermal dephasing time is longer than, say, $1 \mu\text{s}$ one needs $\exp(-h\nu_0/k_B T) < 10^{-2}$. In principle the temperature of the sample enclosure may reach $10-20$ mK but the true photon temperature in the exponent depends on the filtering. Having $\nu_0 = 10$ GHz and $T = 100$ mK makes $\exp(-h\nu_0/k_B T) = \exp(-5) \simeq 7 \times 10^{-3}$. However, the choice of $\nu_0 = 5$ GHz is already 10 times worse with $\exp(-h\nu_0/k_B T) = \exp(-2.5) \simeq 8 \times 10^{-2}$. Therefore, the higher the readout frequency, the longer the thermal dephasing time, a situation exactly the same for any dispersive readout scheme.

Flux noise

There is one remarkable fact about the sensitivity of the fluxonium to the flux bias. External flux φ_{ext} through the fluxonium loop tunes the transition frequencies, so any fluctuations in φ_{ext} would dephase the spectrum. The fluctuations of φ_{ext} could come from improper shielding or from the dynamics of microscopic flux-generating degrees of freedom located directly “inside” the qubit: on the surface of the superconducting films, to give an example. The resulting dephasing time is given by

$$1/T_{\phi}^{\varphi_{\text{ext}}}(\alpha \leftrightarrow \beta) \approx \delta\varphi_{\text{ext}} \times \frac{d\nu_{\alpha\beta}}{d\varphi_{\text{ext}}} \quad (3.39)$$

Qualitatively, the sensitivity $d\nu_{\alpha\beta}/d\varphi_{\text{ext}}$ is easy to evaluate. For the fluxon-like transitions the sensitivity $d\nu_{\alpha\beta}/d\varphi_{\text{ext}} \simeq E_L/\hbar$, for the plasmon transitions $d\nu_{\alpha\beta}/d\varphi_{\text{ext}} \sim 0$, flux-bias-independent for either. At the sweet-spots, even the fluxon transitions become insensitive to first order to the fluctuations in flux. The magnitude of the flux noise $\delta\varphi_{\text{ext}}$ depends on the spectral density of flux noise. Its presently accepted value is in the range $\delta\varphi_{\text{ext}} \sim 10^{-5} - 10^{-6}$. Note that the sensitivity of the fluxon transitions to the flux noise is almost a factor of $100 - 1000$ lower than that of the flux qubit [48] away from the sweet-spots, due

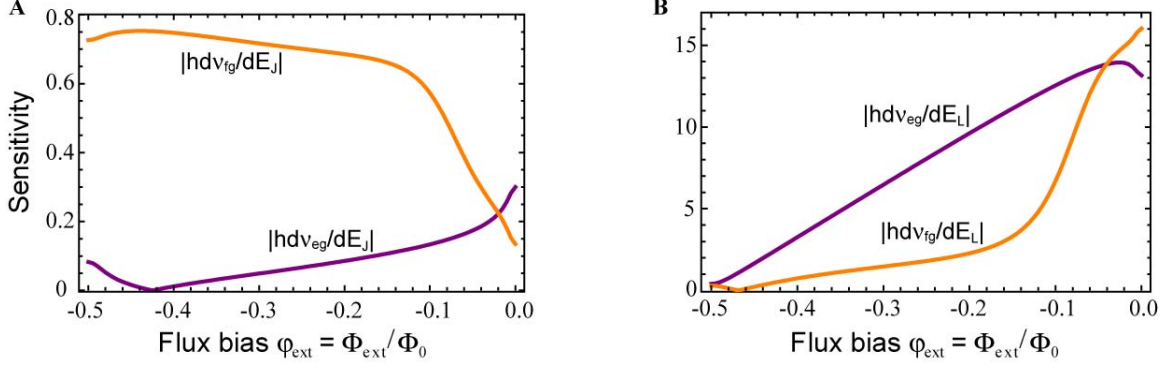


Figure 3-12: Sensitivity of fluxonium transitions to critical current noise. (A) Sensitivity to fluctuations in E_J . (B) Sensitivity to fluctuations in E_L .

to the small value of E_L , or equivalently, due to the large value of the array inductance L .

Critical current noise

There are two remarkable facts about the sensitivity of the fluxonium transitions to the critical current noise in its junctions. Fluctuations in the critical current [75] of the array junctions cause E_L to fluctuate, contributing to the dephasing time:

$$1/T_\phi^L(\alpha \leftrightarrow \beta) \approx \delta E_L \times \frac{d\nu_{\alpha\beta}}{dE_L} \quad (3.40)$$

The sensitivity $d\nu_{\alpha\beta}/dE_L$ of the plasmon-like transitions is again approximately zero. Away from the sweet-spots, the sensitivity of the fluxon transitions grows linearly from nearly zero at $|\varphi_{\text{ext}}| = \pi$ to the maximum value of $|\text{hd}\nu_{\text{fluxon}}/\text{d}E_L|_{\text{max}} = 2\pi^2$. At the $|\varphi_{\text{ext}}| = \pi$ the sensitivity to E_L of the $g \leftrightarrow e$ transition is still minimal as it is approximately given by an E_L -independent quantity E_{SB} .

Turning to the magnitude of the noise δE_L , a statistical argument would imply that it should be \sqrt{N} times smaller than that of an individual junction. Indeed, the quantity $E_L^{-1} = \sum_{j=1}^N E_{J_j}^{-1}$, where the sum is taken over all the array junctions. Fluctuations in E_{J_j} presumably come from the dynamics of the tunneling channels in the oxide, so the noise in different junctions should be uncorrelated. This immediately implies that $\delta E_L/E_L \simeq (\delta E_{J_j}/E_{J_j})/\sqrt{N} = (\delta I_0/I_0)/\sqrt{N}$, where I_0 is approximate value of the critical current of the array junctions. The presently accepted estimate of δI_0 is such that $\delta I_0/I_0 < 10^{-6}$,

which gives $\delta E_{J_j}/E_{J_j} < 10^{-6}$ and $\delta E_L/E_L < 10^{-7}$.

Thus, in the event that critical current noise would end up dominating superconducting qubit coherence, one may expect a $1/\sqrt{N}$ suppression of this effect using an N junction array. For instance, fluxonium $g \leftrightarrow e$ transition away from flux sweet-spots and in the limit $E_{SB} \ll 2\pi^2 E_L$ is entirely fixed by E_L and φ_{ext} (see Fig. 1-16 and discussion around it), hence the quality factor due to critical current noise estimates simply as $(\delta I_0/I_0)/\sqrt{N}$, winning the $1/\sqrt{N}$ factor compared to a transmon qubit of similar frequency [73]. This is remarkable fact number one.

Fluctuations in the critical current of the black-sheep junction lead to fluctuating E_J and the dephasing time contribution

$$1/T_\phi^{E_J}(\alpha \leftrightarrow \beta) \approx \delta E_J \times \frac{d\nu_{\alpha\beta}}{dE_J} \quad (3.41)$$

Qualitatively, the sensitivity of the fluxonium spectrum to E_J can be understood as follows: plasmon-like states have sensitivity to E_J exactly the same as the transmon qubits, $h d\nu_p/dE_J = \sqrt{2E_C/E_J} \sim 1$. As for the fluxon transitions, the sensitivity to E_J away from flux sweet spots comes from the small contribution of the black sheep inductance to the total inductance of the ring, so that the sensitivity $h d\nu_{\text{fluxon}}/dE_J|_{\text{max}} \approx 2\pi^2/N \ll h d\nu_{\text{fluxon}}/dE_L|_{\text{max}}$ is nearly zero away from the sweet-spots, while at $|\varphi_{\text{ext}}| = \pi$ it could be found by differentiating expression (1.16). More interestingly, one can argue that there must exist a value of φ_{ext} at which the sensitivity to E_J of the fluxon transitions in the spectrum (Fig. 3-1-G,H,I) turns to zero. Indeed, for $E_J \rightarrow 0$, the fluxon transitions are entirely determined by E_L . The finite E_J , apart from the contribution to the total inductance of the ring discussed above, rounds the sharp corners of the zigzag. Around zero flux, this rounding clearly reduces the transition frequency from its $E_J = 0$ value, while around half flux quantum bias point the rounding increases the transition frequency. In the fluxonium qubit regime of circuit parameters, the single phase-slip splitting at half flux quantum is of the same order as the double phase-slip splitting at zero flux. Therefore, somewhere in the middle between $|\varphi_{\text{ext}}| = \pi$ and $|\varphi_{\text{ext}}| = 0$, the sensitivity to E_J of the fluxon transition passes through zero, $h d\nu_{\text{fluxon}}/dE_J = 0$. This is remarkable fact number two.

3.3.5 Dephasing: Aharonov-Casher broadening

In this section we finally deal with the effect of quantum phase-slip in the array inductance, using the hamiltonian (1.22). Let us first write down the unperturbed wavefunctions of this hamiltonian in the limit of $|E_S| \rightarrow 0$. The hamiltonian (1.22) is invariant under the transformation $(\varphi, m) \rightarrow (\varphi - 2\pi, m + 1)$. This symmetry represents the fact that by looking only at the initial and final states of the junction loop (see also Fig. 1-7-B) we cannot distinguish which part of the loop (black-sheep junction or array) actually underwent a phase-slip. The unperturbed eigenstates $|\alpha\rangle^{(0)}$ of the hamiltonian (1.22) then take the following form:

$$|\alpha\rangle^{(0)} = \lim_{M \rightarrow \infty} \frac{1}{\sqrt{2M+1}} \sum_{m=-M}^{m=M} \Psi_\alpha(\varphi - 2\pi m) |m\rangle \quad (3.42)$$

Here $\Psi_\alpha(\varphi)$ is the wavefunction of the α -th (non-degenerate) eigenstate of the fluxonium hamiltonian (3.1), represented by the first three terms of the full hamiltonian (1.22) for strictly $m = 0$, kets $|m\rangle$ are the eigenstates of the array phase-slip number operator m , and the normalization is chosen to satisfy $\langle\alpha|\beta\rangle^{(0)} = \delta_{\alpha\beta}$. Now, treating the quantum phase-slip perturbation $\sum_m [\frac{1}{2}E_S |m\rangle \langle m+1| + \text{h.c.}]$ to first order in $|E_S|$, we find that the correction to the qubit transition frequency $\nu_{\alpha\beta}^{\{1\}}$ between the states α and β :

$$\nu_{\alpha\beta}^{\{1\}} = \frac{1}{h} \lim_{M', M'' \rightarrow \infty} \frac{1}{\sqrt{2M'+1} \sqrt{2M''+1}} \frac{1}{2} \sum_{m=-\infty}^{m=\infty} \sum_{m'=-M'}^{-M'} \sum_{m''=-M''}^{-M''} \left(\begin{aligned} & [E_S \langle m'|m\rangle \langle m+1|m''\rangle + E_S^* \langle m'|m+1\rangle \langle m|m''\rangle] \times \\ & (\int d\varphi \Psi_\alpha(\varphi - 2\pi m') \Psi_\alpha(\varphi - 2\pi m'') - \int d\varphi \Psi_\beta(\varphi - 2\pi m') \Psi_\beta(\varphi - 2\pi m'')) \end{aligned} \right)$$

Because states with $m \neq m'$ are orthogonal, the sum reduces to a compact expression

$$\nu_{\alpha\beta}^{\{1\}} = \frac{\text{Re}[E_S]}{h} F_{\alpha\beta}(\varphi_{\text{ext}}) \quad (3.43)$$

where

$$F_{\alpha\beta}(\varphi_{\text{ext}}) = \int d\varphi \Psi_\beta(\varphi) \Psi_\beta(\varphi - 2\pi) - \int d\varphi \Psi_\alpha(\varphi) \Psi_\alpha(\varphi - 2\pi) \quad (3.44)$$

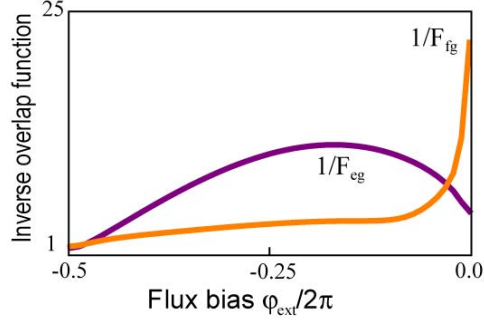


Figure 3-13: Sensitivity of fluxonium $g-e$ and $g-f$ transitions to fluctuating offset charges on the islands of the array. In order to turn the Y-axis into the corresponding dephasing time, one should use the scaling factor of order inverse array r.m.s. quantum phase-slip frequency, $h/\sqrt{N}|E_{SA}|$.

The flux dependence of $\nu_{\alpha\beta}^{\{1\}}$ (Fig. 3-13) comes from the flux-dependence of the fluxonium wavefunctions and their translational properties in the phase coordinate space (Fig. 3-14). In the deep phase-slip regime the wavefunctions are localized at the location of the minima of the fluxon wells, and given the relation of Eq. (3.5), $F_{eg}(\pi) = 1$. A similar overlap function appears in the recent work on a harmonic oscillator with a slippery inductance [76]

In order to convert the shift $\nu_{\alpha\beta}^{\{1\}}$ into the linewidth, let us recall (see Eq. 1.19) that $E_S = \sum_{j=1} E_{S_j} \exp(i2\pi Q_j/2e)$, where Q_j is the total offset charge between the first and the j -th junction, the sum running over all array junctions. Let us also assume that during the time it takes to measure the transition line-shape, the Q_j behave as random variables with a spread of values comparable to e [47, 51]. According to the central-limit theorem, for large N the quantity $\text{Re}[E_S]$ obeys to the Gaussian distribution with zero mean and standard deviation $\sigma = \sqrt{\overline{(\text{Re}[E_S])^2}}$,

$$P\{0 < \text{Re}[E_S] < x\} = \frac{1}{\sqrt{2\pi}\sigma} \exp(-x^2/2\sigma^2).$$

Assuming the array junctions to be approximately identical, i.e. $E_{S_j} \simeq E_{SA}$, we get $\overline{(\text{Re}[E_S])^2} = \frac{1}{2}E_{SA}^2 \times N$, and then readily compute the linewidth $\delta\nu_{\alpha\beta}$ (defined as $\sqrt{\overline{(\nu_{\alpha\beta}^{\{1\}})^2}}$)

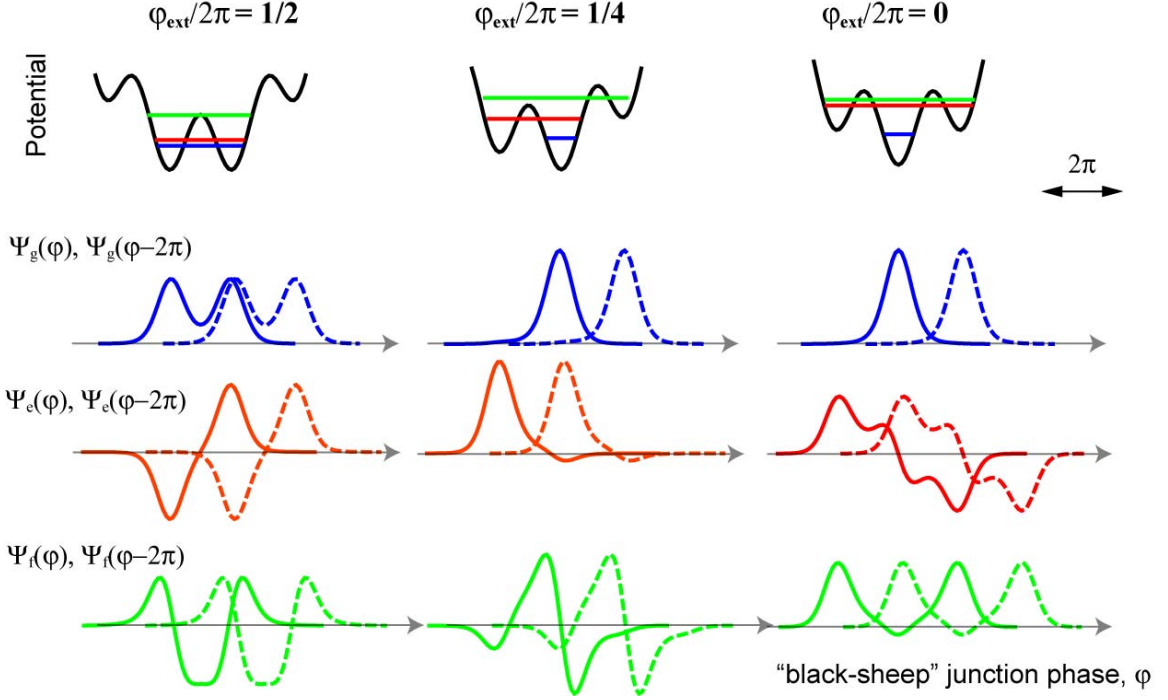


Figure 3-14: Translational properties of fluxonium wavefunctions, illustrated for the lowest three states g , e , and f , and for the three values of external flux. Dashed curves are copies of solid ones shifted exactly by 2π to the right.

given by

$$\delta\nu_{\alpha\beta}(\varphi_{\text{ext}}) = \frac{\sqrt{N/2}E_{SA}}{h} \left| \int d\varphi \Psi_{\beta}(\varphi)\Psi_{\beta}(\varphi - 2\pi) - \int d\varphi \Psi_{\alpha}(\varphi)\Psi_{\alpha}(\varphi - 2\pi) \right| \quad (3.45)$$

If charges Q_j vary slowly compared to the duration of a single Ramsey fringe experiment [77, 18] (of order $10 \mu\text{s}$), the decaying envelope of the Ramsey fringes is given by the absolute value of the characteristic function of the Gaussian distribution. The Ramsey fringe envelope is then given by a Gaussian $\exp\left(-\left(t/T_{\phi}^{\text{CQPS}}\right)^2\right)$, with the dephasing time of the $\alpha \rightarrow \beta$ transition due to the CQPS given by

$$1/T_{\phi}^{\text{CQPS}}(\alpha \leftrightarrow \beta) \simeq \sqrt{2\pi}\delta\nu_{\alpha\beta}(\varphi_{\text{ext}}) \quad (3.46)$$

Chapter 4

Fluxonium: a case study

In this chapter we present the results of our main experiments and their interpretation using the theory developed in Chapter 3.

4.1 Control experiments

The main goal of the experiments described in this section is to establish that the device and its readout are functioning correctly.

4.1.1 Ground state

What would be the simplest, least demanding experiment to establish whether a given fluxonium device, with completely unknown parameters, is functional? Evidently, the frequency shift of the readout resonator must be periodic in applied magnetic field, even if the fluxonium circuit remains in its ground state. This shift is given by $\chi_g(\varphi_{\text{ext}})$, which indeed depends periodically on the flux $\Phi_0\varphi_{\text{ext}}/2\pi$ (see Eq. (3.14)). Monitoring $\chi_g(\varphi_{\text{ext}})$ using a fixed-frequency CW signal, resonant with the readout cavity, for varying φ_{ext} , is indeed the most basic experiment on our device. The results (Fig. 4-1) reveal the expected periodicity with flux as well as the various vacuum Rabi resonances between the resonator frequency $\nu_0 \simeq 8.175$ GHz and fluxonium transitions. This immediately confirms that the entire 44-junction loop is superconducting and that the resonator-atom system is in the strong coupling regime of cavity QED [66, 19]. In this particular experiment,

we did not even bother to extract the phase and magnitude of the reflected signal. Instead, we directly measured the homodyne voltage after mixing the reflected signal with its refrigerator-bypassing copy (Fig. 2-6-B). We recorded the curve from Fig. 4-1 point by point, averaging for about 1 s per point, because the phase stability allowed us to do so. A smarter way to acquire this data would be to sweep φ_{ext} as fast as the coil-qubit bandwidth allows, and then repeat the measurement to average the gaussian noise. In our case the coil bandwidth turned out to be about 1 Hz, probably limited by a huge low-frequency inductance value of the coil and also by the filtering effect of the highly conductive walls of the copper sample holder (Fig. 2-7).

We would like to stress how powerful this technique is for the initial qubit detection. Even in the absence of resonant features, like the full swing of the homodyne signal around $\varphi_{\text{ext}}/2\pi \approx \pm 0.06$ (Fig. 4-1), the base-line of the cavity pull signal is clearly flux-dependent. Averaging time is only limited by the stability of the offset flux, which in our case exceeded the scale of days (see Fig. 4-14).

Although in principle, given the large number of features visible in such a remarkably simple measurement, we could decode the underlying spectrum, in this work we prefer to measure the spectrum directly. We used the ground state modulation data as an approximate road-map in the frequency-flux parameter space of the fluxonium device. The conclusion of this basic experiment is that the array not only superconducts electrical current, but also that the fluxonium device is strongly coupled to its readout resonator.

4.1.2 Fluxon-photon vacuum Rabi resonance

Here, we add one “unit” of complexity to our previous experiment and now sweep the readout frequency ν around the cavity resonance ν_0 . This way we record magnitude and phase of the reflection amplitude as a function of two parameters: readout tone frequency ν and flux bias φ_{ext} . A color density plot (Fig. 4-2-A) of the reflection phase derivative with respect to frequency $\partial\theta(\nu, \varphi_{\text{ext}})/\partial\nu$ reveals a sharp anticrossing between the readout cavity frequency and some transition of the qubit, the so-called vacuum-Rabi resonance. This transition was later identified as the ground to first excited $g \leftrightarrow e$ transition of fluxonium, which, as expected from theory, shows correct linear flux dependence. At the anticrossing,

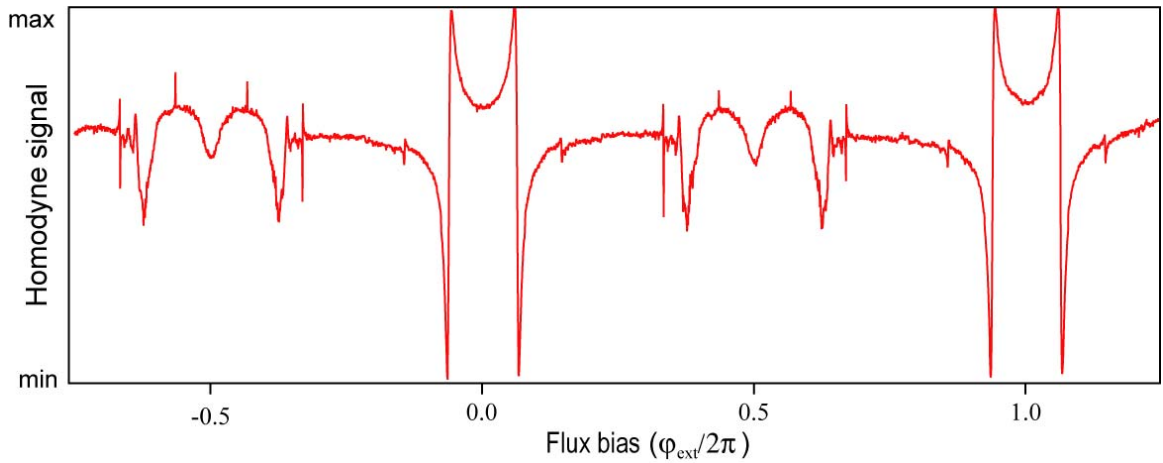


Figure 4-1: Modulation of the nearly resonant reflected $8.18 \text{ GHz} \simeq \nu_0$ microwave signal with externally applied flux φ_{ext} . The signal is clearly flux-periodic indicating that the junction ring is closed and superconducting. The values of φ_{ext} at which the signal undergoes full swings correspond to the anticrossings of the $g \leftrightarrow e$ transition of the device with the later inferred resonator bare frequency $\nu_0 = 8.1755 \text{ GHz}$. Measurement tone populates the resonator with less than 0.01 photon on average (see Fig. 4-3).

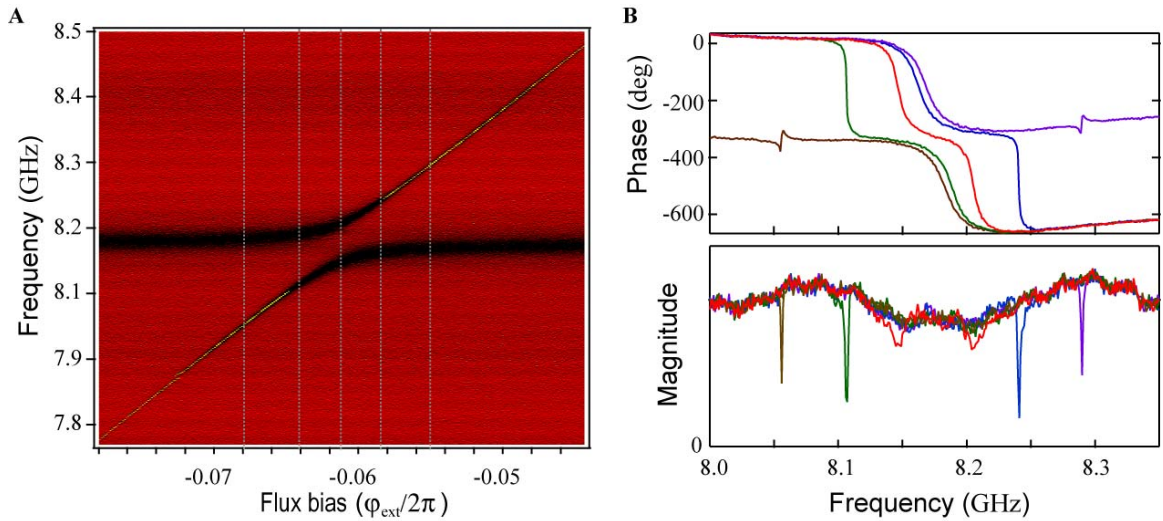


Figure 4-2: (A) Color density plot of the derivative of the phase of the reflection amplitude with respect to frequency. Red, black and yellow colors correspond to zero, negative, and positive values, respectively. Reflection amplitude is measured in a CW experiment with the power level set to -20 dBm (B) Individual traces of reflection phase (top) and magnitude (bottom) as a function of frequency and for a set of φ_{ext} indicated with dashed lines on (A).

both the phase and the amplitude responses split into two identical resonances, as a result of the qubit-cavity hybridization. Away from the anticrossing point, the qubit resonance gradually dims away, while the cavity resonance becomes twice as wide, reaching the qubit-unperturbed value of its quality factor $Q = 400$.

It should be noted that an identical signal is expected from a system of two coupled linear oscillators. In fact the shapes of both phase and the amplitude responses (Fig. 4-2-B) are given by the formula (2.1) for the reflection amplitude off the LCR circuit in the Chapter 2. Indeed, at the anticrossing, the amplitude response is nearly absent, while the phase response wraps by 360 degree, corresponding to the quality factor of $2Q = 800$. This means that the qubit intrinsic dissipation is negligible compared to that in the readout. As we detune the qubit further from the readout resonator, we decouple it more from the measurement leads, therefore tuning it into the undercoupled regime. This is clearly seen as a sharp change from 360 degree phase wrapping to less-than-180 degree phase wrapping, accompanied by an increased dip in the magnitude response (Fig. 4-2-B).

The non-linearity of the qubit manifests itself clearly when looking at the phase response as a function of increasing readout tone power, when $\varphi_{\text{ext}}/2\pi = -0.06$, the anticrossing value. For a range of powers between -30 dBm to -20 dBm¹ the phase response is power-independent, but above -20 dBm the vacuum-Rabi splitting is drastically deformed. When the power reaches close to 0 dBm, the phase response at anticrossing turns into a single cavity response, as if the fluxonium circuit was absent. Effectively, at large photon occupations the system ignores the frequency scale of 60 MHz (the size of the anticrossing) on top of the ~ 8 GHz resonator frequency. The non-linear response of the vacuum Rabi resonance was studied for the case of the transmon artificial atom [78], and probably, as such, does not apply to fluxonium, due to its vastly different transition spectrum. However, the general techniques of [78], must be applicable to treat the non-linear vacuum Rabi resonance(s) of fluxonium.

Let us provide the physical interpretation of the vacuum Rabi resonance in the case of

¹In this section we always give the power at the output of our microwave generators. Since the experimental setup is linear, this power reaches the sample with some frequency-dependent attenuation. Fortunately, the frequency of the readout tone is bounded within the cavity linewidth around the resonance frequency ν_0 , and its value there could be calibrated in terms of photon occupation of the readout (see Fig. 4-5).

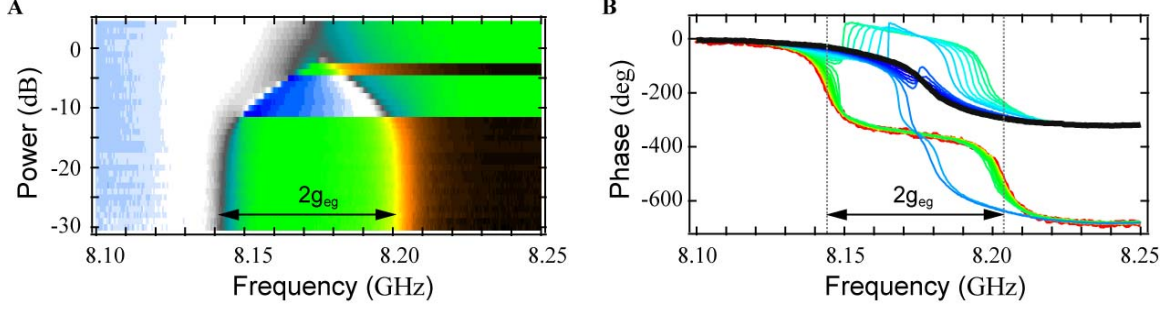


Figure 4-3: Power dependence of the vacuum Rabi resonance. Phase of the reflection amplitude measured as a function of spectroscopy tone power at the vacuum Rabi resonance position of $\varphi_{\text{ext}}/2\pi = 0.06$. (A) Color density plot representation. (B) Individual traces shifted for clarity to the same origin point (top-left). The red trace corresponds to the lowest power (-30 dBm), the black trace corresponds to the higher power ($+5$ dBm). Sharp transition in the shape of the phase-frequency response is an artifact of phase wrapping.

fluxonium circuit. Since the fluxonium $g \leftrightarrow e$ transition really corresponds to the change in the phase-slip number in the loop by unity (or to the change in the generalized flux in the array inductance by approximately Φ_0), it is safe to say that the splitting in the spectrum at $\varphi_{\text{ext}}/2\pi = -0.06$ at sufficiently low powers takes place because a single quanta (photon) in the readout cavity exchanges coherently with the phase-slip (fluxon) in the fluxonium loop. This situation is partially analogous to the original cQED experiment [19], in which a single photon in the cavity was exchanging with the even or odd superpositions of states with/without a single excess Cooper pair on a superconducting island. Remarkably, just like in the case of a Cooper-pair box, the interaction between fluxons and photons originates from the coupling of the voltage U at the end of the CPS resonator to the charge $2en$ on the leads of the black-sheep junction. This is only possible because the phase across the black-sheep junction fluctuates quantum-mechanically even in the state with a well defined phase-slip number, thus leading to the finite-frequency electric polarizability. With the coupling capacitance of less than a fF we reach the vacuum Rabi frequency of $g_{eg} = 30$ MHz (Eq. 3.10).

4.1.3 AC-Stark effect

Here, we detune the flux bias φ_{ext} away from the $g \leftrightarrow e$ vacuum Rabi resonance, fix the frequency of the readout tone to be about ν , and add a second, spectroscopy tone, to excite

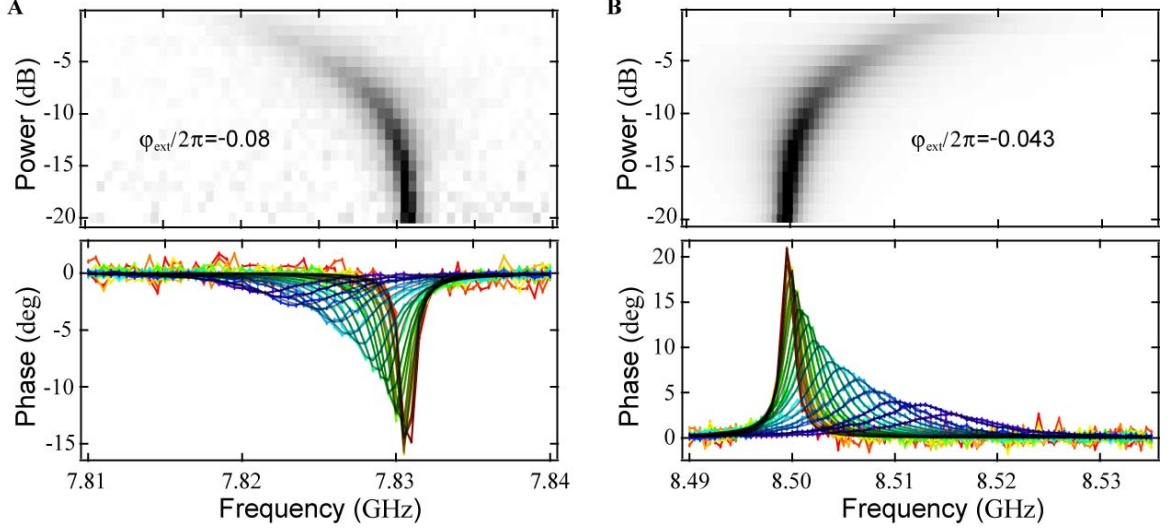


Figure 4-4: Two-tone spectroscopy of the fluxonium for a fixed qubit tone power and cavity tone frequency of 8.185 GHz while varying the cavity tone power and the qubit tone frequency. The qubit tone power is set to populate the excited state by approximately 1/4.

the qubit separately [46]. This experiment tests the backaction of the measurement circuit on the qubit. Of practical importance, this experiment also allows us to calibrate the power at the output of the readout microwave generator in terms of photon numbers in the readout resonator. Just as with the previous two experiments, we only use CW signals, so the system is always in a steady state. We chose two values of the flux bias, $\varphi_{\text{ext}}/2\pi = -0.06$, where the qubit frequency $\nu_{eg} = 7.831 \text{ GHz} < \nu_0$, and $|g_{eg}/(\nu_{eg} - \nu_0)| \simeq 0.1 \ll 1$, and also for $\varphi_{\text{ext}}/2\pi = -0.043$, where $\nu_{eg} = 8.499 \text{ GHz} > \nu_0$, and $|g_{eg}/(\nu_{eg} - \nu_0)| \simeq 0.1 \ll 1$ also takes place. We will refer to these two situations as the qubit being “below the cavity” and “above the cavity”, respectively. We select the qubit probe tone power to a value which gives a population of the excited states of about 1/4 (see Fig. 4-6) and sweep the frequency of this tone. We monitor the reflected signal using a set of increasing readout tone powers (Fig. 4-4) and find that the qubit resonances acquire both an AC-Stark shift and a width, both growing with increasing readout tone power. The sign of the qubit frequency shift is positive above the cavity and negative below the cavity. The qubit lineshape fits well a lorentzian for the explored range of readout tone power. For both negative and positive AC-Stark shifts, the linewidth increases by absolute value linearly with the readout tone power, or

equivalently with the average number of photons n in the readout resonator² (see Eq. 3.13), according to the relation [46]

$$\Delta\nu_{eg}(n) = 2\frac{g_{eg}^2}{\nu_{eg} - \nu_0}n \quad (4.1)$$

The expression for $\nu_{eg}(n)$ generically follows from the general expression (3.13), by computing the expression $\nu_{eg} = (\delta E_{e,n} - \delta E_{g,n})/h = n\chi_{eg}$. Fitting the AC-Stark shifts vs. readout power to a line (see Eq. 4-5), we get

$$n = (2 - 4) \times P_{\text{in}}/1 \text{ mW} \quad (4.2)$$

using, the data both below (Fig. 4-5-A) and above (Fig. 4-5-B) the cavity. The broadening of the qubit line with increasing the readout power could be probably be attributed, at least in part, to the readout back-action effect (3.38), however the quoted formula works only in the limit of small n .

Thus, we obtain a rough but very informative link between the input microwave readout power and the cavity photon number. The obtained photon number to mW conversion makes sense quantitatively (Fig. 4-3): 0 dBm, or 2 – 4 photons indeed spoils completely the vacuum-Rabi resonance, –10 dBm, or around half a photon already distorts the splitting considerably, no power dependence takes place at –20 dBm. In the rest of this work, we used readout power of about –20 dBm in continuous measurement and the readout power around 3 dBm in pulsed measurement.

The still Lorentzian qubit shape even in the presence of $n = 4$ readout photons also makes sense. Indeed, we have estimated $\chi_{eg} \simeq 2$ MHz for both below and above cavity experiments from the power broadening measurements described below; the quantity which determines the measurement strength is given by $n\chi_{eg}^2/\kappa^2 \simeq 1/10$ and is still much smaller than unity ($\kappa = 10$ MHz), so we should still be in the Lorentzian regime. We also note that the height of our Lorentzians reduced drastically for $n = 4$, which indicates that perhaps our dispersive scheme is not as well understood at $n = 4$ as it is at $n = 0.04$.

²The number of photons n is linked to the total power reflecting off the cavity $P_{\text{out}}/h\nu_0\Gamma_{\text{cavity}}$. The power P_{out} is linked to the readout tone power by the total attenuation on the way from the generator to the chip.

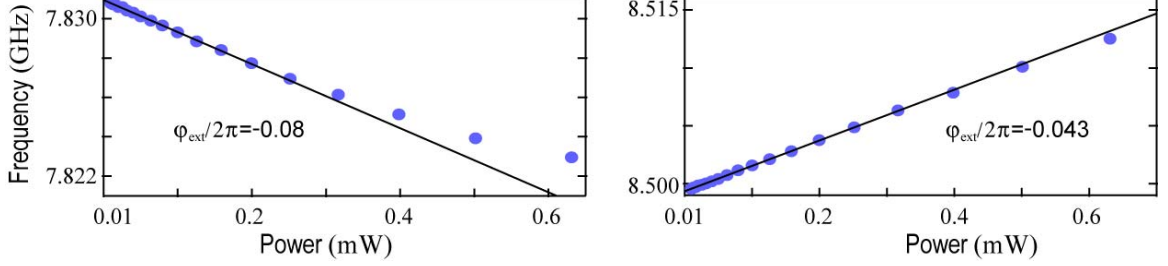


Figure 4-5: Photon number calibration. AC Stark shifts vs the cavity tone power for the two values of φ_{ext} , above and below the cavity.

4.1.4 Power broadening

Here we fix both the power and the frequency of the readout tone, but vary the frequency ν_{spectr} of the qubit tone and its power P_{spectr} and perform qubit spectroscopy at $\varphi_{\text{ext}}/2\pi \simeq -0.043$. We focus on the three peaks (Fig. 4-6) found at frequencies 8.500 GHz, 9.923 GHz, and 11.235 GHz, later identified as transitions from the ground states to the first, second, and third excited states of fluxonium, respectively. We find the phenomena of power broadening and transition population saturation (Fig. 4-6-insets), familiar from the NMR field. Namely, the lorentzian transition lineshape increases its width linearly with the excitation tone amplitude (and not power!) and the height of the resonance, given by $\theta_{g\alpha} = (2p_\alpha - 1) \times \chi_{g\alpha}/\kappa$, where p_α is the population of the state α , first grows linearly with power and then saturates at $p_\alpha|_{\text{max}} = 1/2$. The qubit excited state population obeys to the well-known Bloch-type NMR equation result [79]

$$p_\alpha = \frac{1}{2} \frac{\Omega_{\text{drive}}^2}{1/T_2^2 + (\nu_{\text{spectr}} - \nu_{eg})^2 + \Omega_{\text{drive}}^2} \quad (4.3)$$

where T_2 is the intrinsic linewidth of the qubit and Ω_{drive} is the effective drive strength, proportional to the $\sqrt{P_{\text{spectr}}}$ and the charge matrix element.

4.2 Spectroscopy

Here we report detailed measurements of the fluxonium transition spectrum for the parameter space $\{\nu, \varphi_{\text{ext}}/2\pi\} \in \{(300 \text{ MHz}, 12 \text{ GHz}), (-0.5, 0)\}$. Since the linewidth of most of the transitions is only a few MHz, the only way to examine the raw data is to zoom in

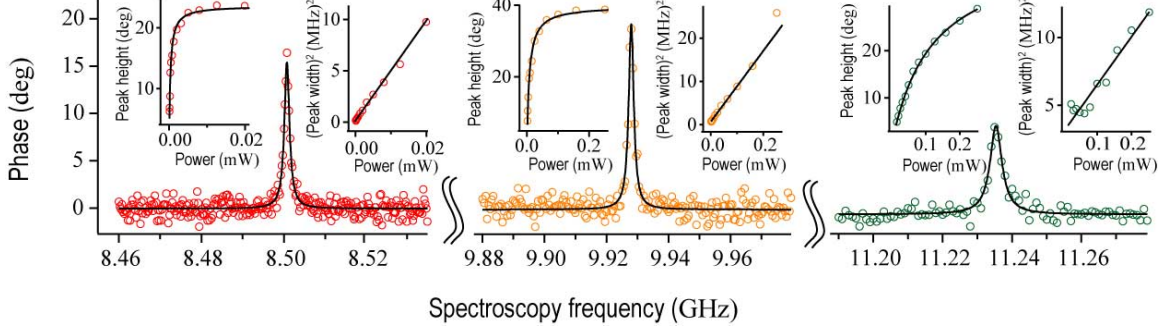


Figure 4-6: Power broadening of qubit transitions. Phase (colored circles) of reflected readout tone as a function of spectroscopy tone frequency taken at $m_{\text{ext}} = -0.043$. Data for the first three resonances (further identified as transitions from the ground state to states 1, 2 and 3) is shown from left to right in red, orange and green respectively. Resonances are well-fitted by Lorentzians (solid black lines) for a broad range of spectroscopy powers. Insets on the two sides of each resonance show the dependence of the resonant peak height (left) and width squared (right) on the spectroscopy tone power. Data in all insets follow the predictions (solid black lines) of Bloch equations describing relaxation dynamics for a spin 1/2 and indicate that all transitions involve one photon.

on the individual interesting regions. Therefore, below we focus every subsection onto a separate fluxonium feature, discussed in the theory chapter. At the end of this section we provide comparison of the experimental data to the theory, by processing the raw data into the coordinates of the spectroscopic resonances in the $\{\nu, m_{\text{ext}}\}$ parameter space. Such a comparison provides us with the parameters of the fluxonium: E_J, E_C, E_L, g (see Table 5.2)

4.2.1 Single phase-slip splitting near $\varphi_{\text{ext}} = \pi$

Setting $|\varphi_{\text{ext}}| = \pi$, we perform a spectroscopy scan at low frequencies and find a resonance at approximately $\nu_{eg}(|\varphi_{\text{ext}}| = \pi) = 370$ MHz (Fig. 4-7-A, left). The resonance is narrower than one MHz, and fits well to the loretzian shape. Repeating this experiment for varying values of φ_{ext} , we obtain a 2D image showing a flux dependent line (Fig. 4-7-A, right), which fits well to the typical avoided-crossing hyperbolic shape, given by Eq. (3.4). Repeating this experiment for a broader range of φ_{ext} and spectroscopy frequency, this time around $|\varphi_{\text{ext}}| = \pi/2$, we find a clean straight line (Fig. 4-7-B). These observations imply that the transition we are measuring is the fluxon transition with the phase-slip energy $E_{SB} = h \times \nu_{eg}(|\varphi_{\text{ext}}| = \pi)$. The slope of the straight line section in this case should be given by

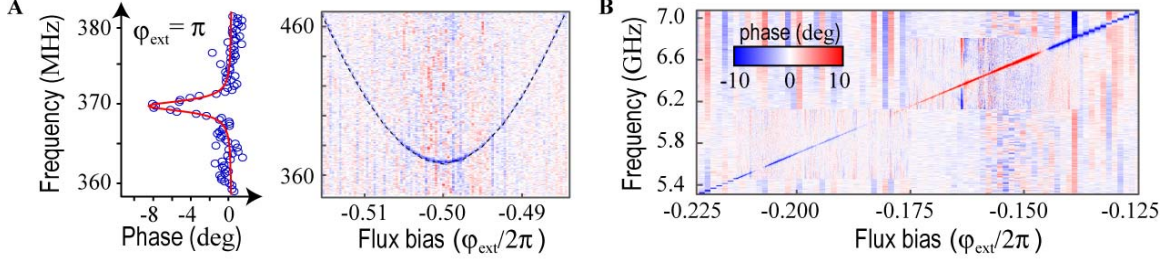


Figure 4-7: Single phase-slip in the black-sheep junction. (A) Left: Lowest frequency $g \leftrightarrow e$ transition measured at $|\varphi_{\text{ext}}| = \pi$. Solid line is a Lorentzian fit; traces from left collected as a function of external flux around $|\varphi_{\text{ext}}| = \pi$, color scale shows the reflected phase values. Dashed line is a hyperbolic (see Eq. 3.4) fit. (B) $g \leftrightarrow e$ transition measured as a function of flux around $|\varphi_{\text{ext}}| = \pi/2$. The change in color of the resonance line corresponds to the change in the sign of the dispersive shift (Eq. 3.16) as shown in the inset of panel (B).

$2\pi E_L^\Sigma/h$ GHz (see Eq. 1.13 and discussion in the section 1.3). Experimentally, the slope measures to 2.9 GHz, implying $E_L^\Sigma = 0.46$ GHz, not far from the value of E_L determined later (Table 5.2) from the global fit to the larger scale data, shown below.

4.2.2 Double phase-slip splitting and plasmon near $\varphi_{\text{ext}} = 0$

Now we move to around $\varphi_{\text{ext}} = 0$ and also move up in frequency to catch the maximum of the $g \leftrightarrow e$ transition (Fig. 4-8). We find an avoided crossing exactly at $\varphi_{\text{ext}} = 0$ between the $g \leftrightarrow e$ transition and the next, $g \leftrightarrow f$ transition. This anticrossing could be interpreted as the double phase-slip in the black-sheep junction which changes the flux quanta (fluxon) occupation of the loop by two. The frequency of the avoided crossing measures to be about $\nu_{fe}(\varphi_{\text{ext}} = 0) = 290$ MHz, which is of the same order as the single phase-slip frequency E_{SB}/h . In the deep phase-slip regime one expects negligible $\nu_{fe}(\varphi_{\text{ext}} = 0)$ compared to $\nu_{eg}(|\varphi_{\text{ext}}| = \pi) = E_{SB}/h$, see Fig. (3-1-B, E, H). However, the proximity of the plasmon resonance combined with the relatively large E_{SB} distorts the phase-slip picture. The presence of the plasmon mode can already be seen in the flattening of the $g \leftrightarrow f$ transition around $|\varphi_{\text{ext}}/2\pi| = 0.1$. Another interesting observation one makes from Fig. (4-8) is the variation of the sign of the dispersive shift χ_{eg} . The sign of χ_{eg} changes during the passing of the ν_{eg} frequency through the vacuum Rabi resonance (color changes from blue to red), however, at around $|\varphi_{\text{ext}}/2\pi| = 0.08$, the dispersive shift goes through zero and changes

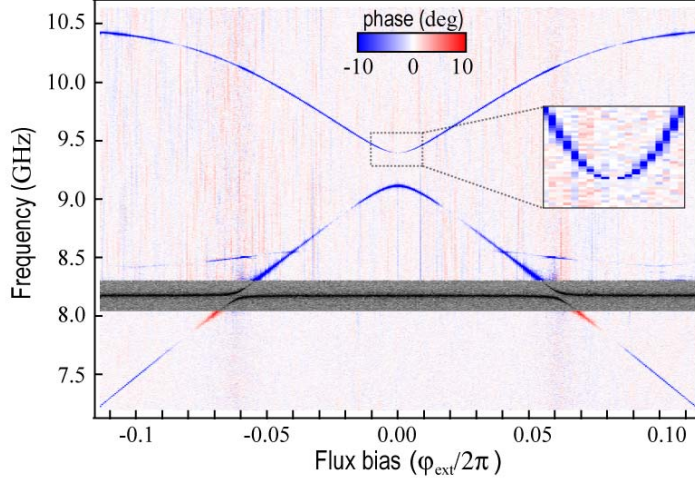


Figure 4-8: Spectroscopy data piece around $\varphi_{\text{ext}} = 0$. Gray section data is taken using the single-tone protocol of Fig. (4-2). The horizontal black resonance is the readout frequency. The avoided crossing between the two blue spectroscopy lines ($g \leftrightarrow e$ and $g \leftrightarrow f$ transitions) could be interpreted as the double phase-slip in the black-sheep junction. The flattening of the $g \leftrightarrow f$ transition happens because away from $\varphi_{\text{ext}} = 0$, it turns into a plasmon resonance. The “hole” exactly at $\varphi_{\text{ext}} = 0$ in the spectroscopy line of the upper curve manifests the selection rule $\varphi_{ef}(\varphi_{\text{ext}} = 0) = 0$ (see Fig. 3-2-B,E)

sign again. This change of sign happens because of the competition between the regular $e \leftrightarrow g$ vacuum Rabi resonance and other resonances, like $e \leftrightarrow f$ and $g \leftrightarrow f$ (see Fig. 3-9).

4.2.3 The $e \leftrightarrow f$ vacuum Rabi resonance and side-band transitions

Spectroscopy around $|\varphi_{\text{ext}}| = \pi$ but at higher frequencies, of order the plasma frequency, reveals side-bands of the qubit $g \leftrightarrow e$ transition – not visible here being far down in frequency – with the readout resonator frequency (Fig. 4-9). The frequency of the side-band transitions verify $\nu_{g,0 \leftrightarrow e,1} = \nu_{eg} + \nu_0$ and $\nu_{e,1 \leftrightarrow g,0} = |\nu_{eg} - \nu_0|$, and are indicated with red and blue arrows at (Fig. 4-9-right). In addition, two more qubit transitions are visible, the $g \leftrightarrow f$ transition and the $e \leftrightarrow f$. Note how the transition $g \leftrightarrow f$ is almost flux-independent (on the scale of the blue side-band), which points to plasmonic nature of the former. The transitions starting from the qubit excited state e show up due to finite occupation of the excited state at the temperatures of about 15 mK³. The anticrossing between the blue side-band $\nu_{g,0 \leftrightarrow e,1}$ and

³ $h \times 20 \text{ GHz} \simeq k_B \times 1 \text{ K}$, so the $g \leftrightarrow e$ transition frequency at $\varphi_{\text{ext}} = \pi$ of $E_{SB}/h = 370 \text{ MHz}$ corresponds to the temperature of approximately 20 mK. Therefore, the excited state e has a fraction of about 30% of

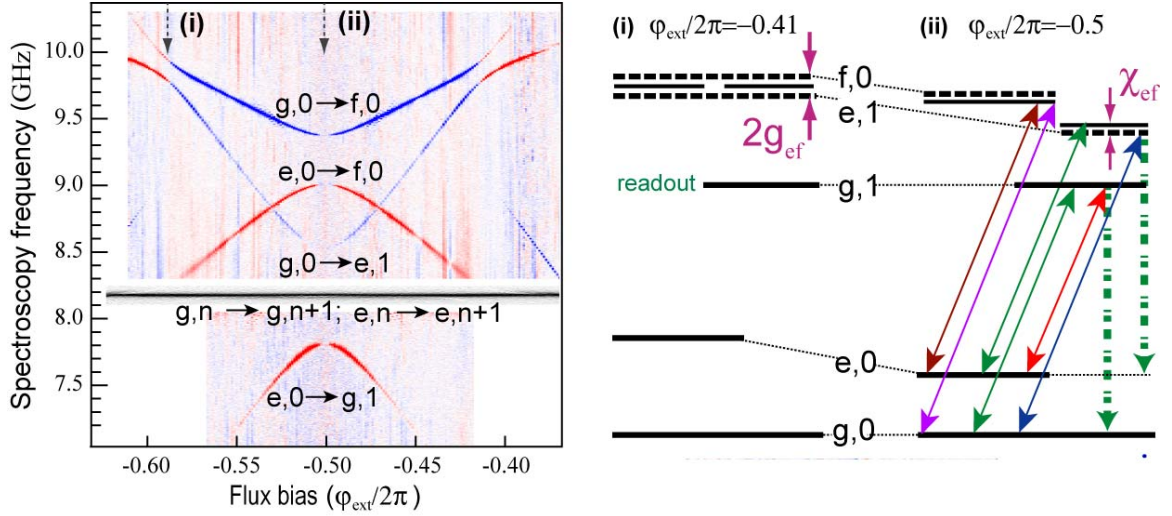


Figure 4-9: Side-band transitions and the $e \leftrightarrow f$ vacuum Rabi resonance. Left: Low power spectroscopy revealing red ($e,0 \leftrightarrow g,1$) and blue ($g,0 \leftrightarrow e,1$) side-band transitions, involving both an excitation of the atom and the readout, as well as atomic transitions ($g,0 \leftrightarrow f,0$) and ($e,0 \leftrightarrow f,0$), not involving the readout. Right: schematic of the combined atom-cavity transition spectrum, for two values of φ_{ext} . The occupation of the readout is limited to one quanta. The anticrossing of the blue side-band transition and the $g \leftrightarrow f$ transition results in the corresponding vacuum Rabi resonance. Away from the resonance the qubit $g \leftrightarrow e$ transition acquires a dispersive shift χ_{eg} due to the repulsion of the state $e,1$ from the state $f,0$. The thick green arrows indicate quick relaxation of the states $g,1$ and $f,1$ into, respectively, $g,0$ and $f,0$.

the qubit second-excited state transition frequency $\nu_{g \leftrightarrow f}$ manifests the very strong vacuum Rabi resonance of the transition $e \leftrightarrow f$, with the splitting $2g_{ef} \simeq 180$ MHz. This resonance is largely responsible for the fluxonium dispersive shifts χ_{eg} of the $g \leftrightarrow e$ transition. The origin of the $\chi_{eg}(\varphi_{\text{ext}} = \pi)$ is illustrated in Fig. (4-9-right). Despite the enormous detuning of the 370 MHz qubit transition and the 8.175 GHz readout resonator frequency, the dispersive shift χ_{eg} comes from the repulsion of the state $(e, 1)$ and $(g, 0)$, in terms of the language of Fig. (3-4-A) or from the vacuum Rabi resonance of the frequency ν_{ef} , which is of order plasma frequency, in terms of the language of Fig. (3-4-B).

4.2.4 Experiment vs. theory

The summary of the spectroscopy data and its theory fit are presented in Fig. (1-18) in the introductory chapter. The data points are collected by analyzing the peak position from the data like in Fig. (4-2), Fig. (4-7), Fig. (4-8), and Fig. (4-9). The theory comes from diagonalization of the hamiltonian (3.11) (without dissipation) with the following parameters⁴: E_J , E_C , E_L , ν_0 , and g . The transition spectrum shows up a number of feature, each strongly restricting the circuit parameters. Thus, the cavity frequency can be measured almost independently up to some small dispersive shift χ_g , which does not exceed few MHz. The ratio $\sqrt{E_J/E_C}$ is restricted by the single phase-slip, while the inductive energy E_L is defined by the slope of the $g \leftrightarrow e$ transition. The double phase-slip transition depends exponentially not only on E_J but also on E_L , as the latter contributes considerably to the potential barrier for tunneling at $\varphi_{\text{ext}} = 0$. All the parameters are extracted into the Table (5.2).

4.2.5 High power spectroscopy and spurious modes

At sufficiently high qubit irradiation powers, the fluxonium spectrum is very rich (Fig. 4-11). Some of the features were already exposed and discussed previously in Fig. (4-8)

the ground state population.

⁴Actually, in order to reach better fit at higher frequencies, we had to include the coupling to a single spurious mode (check hamiltonian 3.27), characterized with the coupling constant $g^{\{\varphi\}} = 0$, $g^{\{n\}} = g_{\text{sp}}$ and frequency ν_{sp} . This mode shows up in the spectroscopy above 10 GHz and presumably corresponds to a charged impurity (Fig. 4-10).

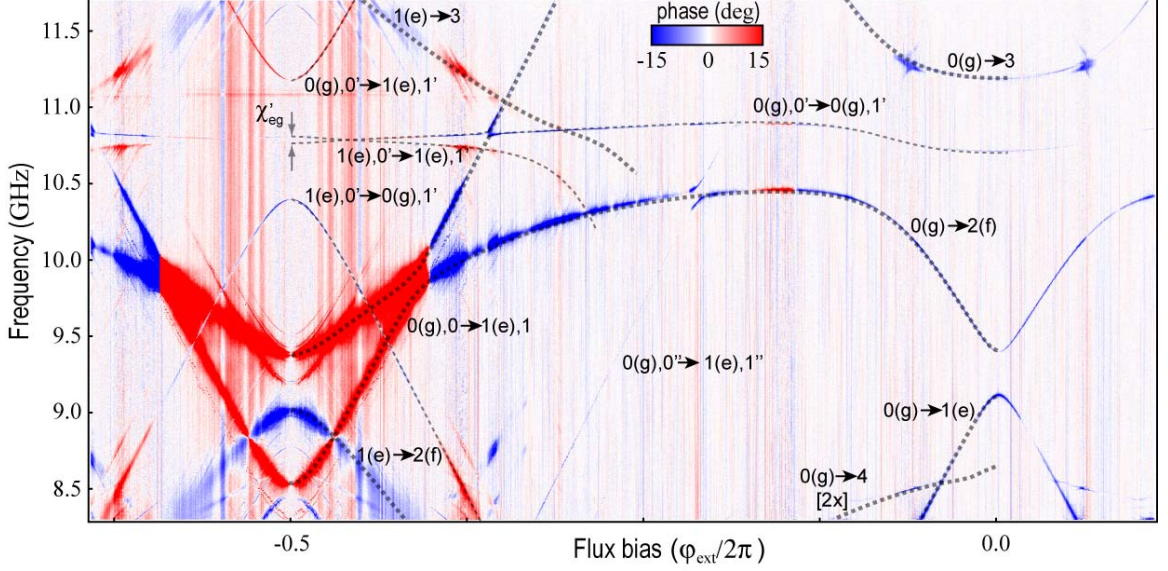


Figure 4-10: Large-scale and high-power spectroscopy data. Dashed lines represent the theory fit, thick lines for transitions involving only fluxonium or readout, thin lines for transitions involving an impurity. Qubit excitation is labeled with the first number(letter), readout excitation is labeled with a second number, and impurity excitation is labeled with a second number and a “'” superscript.

and Fig. (4-9). In order to include higher than f -state fluxonium states we turn to using numbers instead of letters (we keep the corresponding letter notation in parenthesis), just like we did in the discussion around Fig. (3-7) and Fig. (3.26). Around $\varphi_{\text{ext}} = 0$ we see the second order (double-photon) $0(g) \leftrightarrow 4$ transition and also the direct $0(g) \leftrightarrow 3$ transition. The $0(g) \leftrightarrow 2(f)$ transition anticrosses the blue side-band of the readout, labeled here $0(g), 0 \leftrightarrow 1(e), 1$; however the anticrossing is not as clean as in Fig. (4-9), which was taken at very low irradiation powers. The distortion of this $e \leftrightarrow f$ vacuum Rabi resonance at high irradiation powers is not surprising, in view of the similar distortion with the basic $g \leftrightarrow e$ vacuum Rabi resonance, discussed in Fig. (4-3).

A qualitatively new transition appears between 10.5 and 11 GHz. Despite its weak flux-dependence, it cannot be associated with the plasmon excitation. This transition testifies to the presence of a new degree of freedom in the circuit, which we call an “impurity” and label it $0(g), 0' \leftrightarrow 0(g), 1'$, by analogy with the qubit-readout interaction discussion. The impurity certainly interacts with the fluxonium, because of the evident repulsion of the transition in question from both $0(g) \leftrightarrow 3$ and $0(g) \leftrightarrow 2(f)$ around $\varphi_{\text{ext}} = 0$. We were able

to precisely model this new degree of freedom by employing the hamiltonian (3.27) with a coupling constant $g_k^{\{n\}} = g_{\text{imp}}$, $g_k^{\{\varphi\}} = 0$, and $\nu_k = \nu_{\text{imp}}$ (see Table 5.2 for the values). Qualitatively, the interaction of the fluxonium with the impurity could be understood within the theory of interaction of the fluxonium with its readout; a diagram like that on Fig. (4-9-left) is helpful in approximate calculations. Although the inclusion of the impurity adds two more parameters to fit, we earn several new distinct features in the spectrum. First, around $|\varphi_{\text{ext}}/2\pi| = 1/2$ we find the two side-bands with the $0(g) \leftrightarrow 1(e)$ transition of the qubit, the red side-band $1(e), 0' \leftrightarrow 0(g), 1'$ and the blue side-band $0(g), 0' \leftrightarrow 1(e), 1'$. The blue side-band of the impurity $0(g), 0' \leftrightarrow 1(e), 1'$ matches the blue side-band of the readout $0(g), 0 \leftrightarrow 1(e), 1$ after a translation down by the frequency $\nu_{\text{imp}} - \nu_0$. The second neat feature of the interaction of the impurity with the fluxonium circuit is the splitting of the impurity mode $0(g), 0' \leftrightarrow 0(g), 1'$ into two lines at $|\varphi_{\text{ext}}/2\pi| = 1/2$, by an amount $\chi'_{1(e)0(g)}$. The choice of the name for this splitting is not accidental: it indeed carries the meaning of the dispersive shift of the impurity frequency by the qubit transition. The lower frequency could be interpreted as the transition $0(g), 0' \leftrightarrow 0(g), 1'$, with the frequency $\nu_{\downarrow} = \nu_{\text{imp}} + \chi'_{0(g)}$, while the higher frequency would be the transition starting from the qubit excited state, $1(e), 0' \leftrightarrow 1(e), 1'$, with the frequency $\nu_{\uparrow} = \nu_{\text{imp}} + \chi'_{1(e)}$, by analogy with the interaction of the fluxonium with the readout resonator. Given the absolute value of the impurity frequency and the selection rules of the fluxonium spectrum at $|\varphi_{\text{ext}}/2\pi| = 1/2$, we can write the approximate expression for $\chi'_{1(e)0(g)}(|\varphi_{\text{ext}}/2\pi| = 1/2)$

$$\chi'_{1(e)0(g)}(|\varphi_{\text{ext}}/2\pi| = 1/2) = g_{\text{imp}}^2 \left(\frac{|n_{21}|^2}{|\nu_{21} - \nu_{\text{imp}}|} + \frac{|n_{03}|^2}{|\nu_{03} - \nu_{\text{imp}}|} \right) \quad (4.4)$$

which provides a correct estimate. The numerical treatment with only two extra adjustables (ν_{imp} and g_{imp}) fully covers the two features in the spectrum, and, in addition, precisely models the small, yet considerable flux-dependence of the $0(g), 0' \leftrightarrow 0(g), 1'$ around $|\varphi_{\text{ext}}/2\pi| = 1/2$. The impurity also interacts with the transition $1(e) \leftrightarrow 3$ and $1(e) \leftrightarrow 4$ (not shown), which results in a strong anticrossing of the $1(e), 0' \leftrightarrow 1(e), 1'$ transition with the $1(e) \leftrightarrow 3$ transition.

The impurity discussed above is not the only extra mode revealed in the high-power spectroscopy. For instance, the $0(g) \leftrightarrow 2(f)$ transition anticrosses around $|\varphi_{\text{ext}}/2\pi| \approx 0.25$

some transition which appears like a qubit blue side-band with another impurity, at much lower frequency than that of the first one. We therefore label it $0(g), 0'' \leftrightarrow 1(e), 1''$. The anticrossing would involve the matrix element n_{12} , which reaches its maximum values (see Fig. 3-2-B,E) around those values of flux. Interestingly, we did not find any anticrossing of this impurity mode (down to few MHz in size) with the lowest $0(g) \leftrightarrow 1(e)$ transition, which should be taking place around 5 GHz. This is likely because the matrix element $|n_{01}(|\varphi_{\text{ext}}/2\pi| \approx 0.25)|$, determining the size of that anticrossing is much smaller than $|n_{12}(|\varphi_{\text{ext}}/2\pi| \approx 0.25)|$, $|n_{01}(|\varphi_{\text{ext}}/2\pi| \approx 0.25)| \ll |n_{12}(|\varphi_{\text{ext}}/2\pi| \approx 0.25)|$ (see Fig. 3-2-B,E).

In addition to these two well-visible impurities, there is a whole forest of them, in the form of the side-bands with the qubit, both red and blue. In an attempt to test their origin we have performed thermal cycling of the device to about the temperature of liquid nitrogen, 77 K, and repeated the spectroscopy (Fig. 4-11). The key finding is that the thermal cycling moved the frequencies of all the non-fluxonium transitions in the spectrum, leaving the fluxonium circuit parameters unchanged. Indeed, the transitions highly sensitive to circuit parameters, $\nu_{01}(|\varphi_{\text{ext}}| = \pi)$ and $\nu_{12}(\varphi_{\text{ext}} = 0)$ have remained the same within 1 MHz resolution. The impurity frequency seems to have moved towards a higher value with the coupling constant drastically reduced. As a result, it no longer pushes on the $0(g) \leftrightarrow 2(f)$ and $0(g) \leftrightarrow 3$ transitions, which results in some small deviation between the old theory and new data. The frequency of the “second” impurity, involving the blue side-band of the qubit, has moved up, with the splitting nearly unchanged. All other impurity-involving transitions have changed their frequency.

The only possible explanation, that the fluxonium parameters E_L , E_J , E_C remain unchanged while the non-fluxonium transitions change drastically under thermal cycling, implies the microscopic nature of the observed non-fluxonium transitions, hence the name for them, “impurities”⁵. Several properties of the observed impurity states are worth noting. Individual impurities exhibit coupling to the fluxonium circuit exceeding 100’s of MHz, larger than that to the readout resonator. However, none of the impurities anticrosses with the main $0(g) \leftrightarrow 1(e)$ transition, at least down to the anticrossing frequency of few MHz.

⁵It is not excluded that some of the “impurities” we encounter originate from trapped vortices.

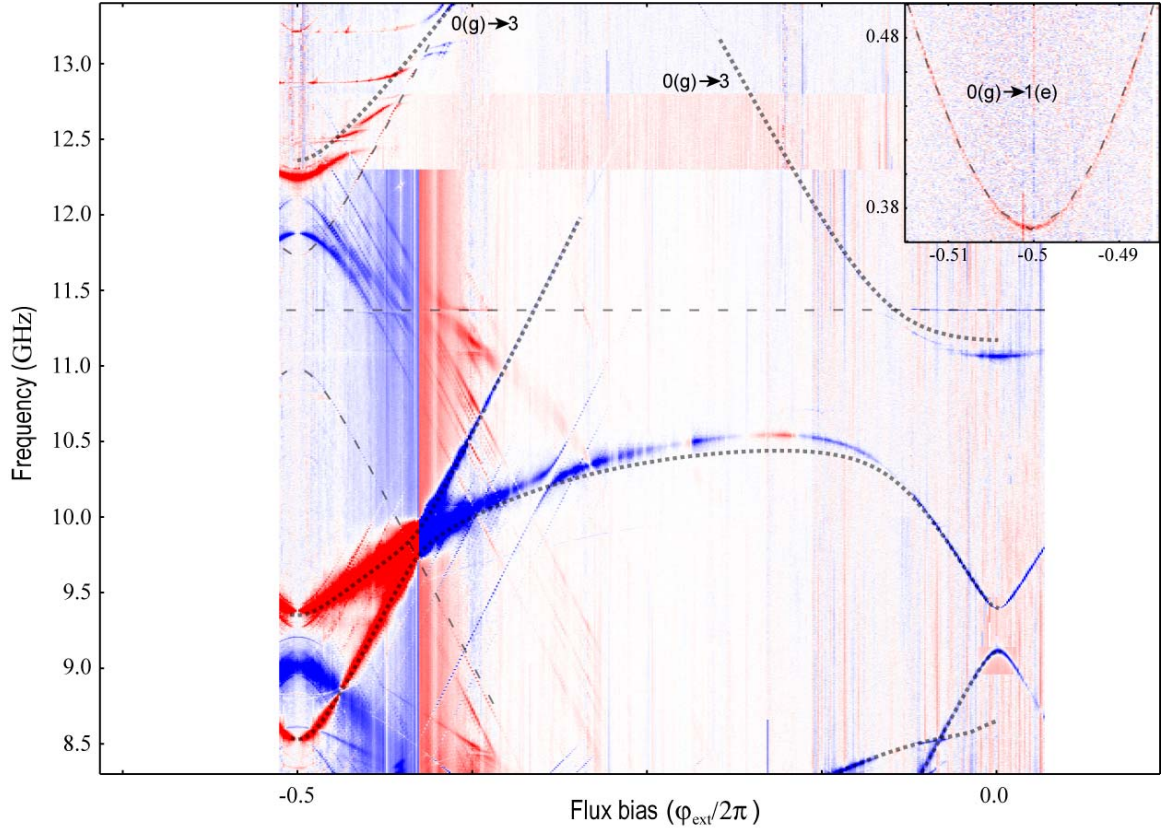


Figure 4-11: Spectroscopy data after thermal cycling to 77 K. Theory lines are identical to those used in Fig. (4-10). Inset shows the $0(g) \leftrightarrow 1(e)$ transition at $|\varphi_{\text{ext}}| = \pi$. While the qubit $0(g) \leftrightarrow 1(e)$ transition did not change, the higher frequency $0(g) \leftrightarrow 2(f)$ and $0 \leftrightarrow 3$ transitions have shifted notably. This is likely due to their interaction with an impurity transition, which now lies at approximately 11.4 GHz and is almost independent of flux. Side-bands of the qubit $0(g) \leftrightarrow 1(g)$ transition with this new impurity frequency are clearly visible (dashed lines) around $\varphi_{\text{ext}} = \pi$.

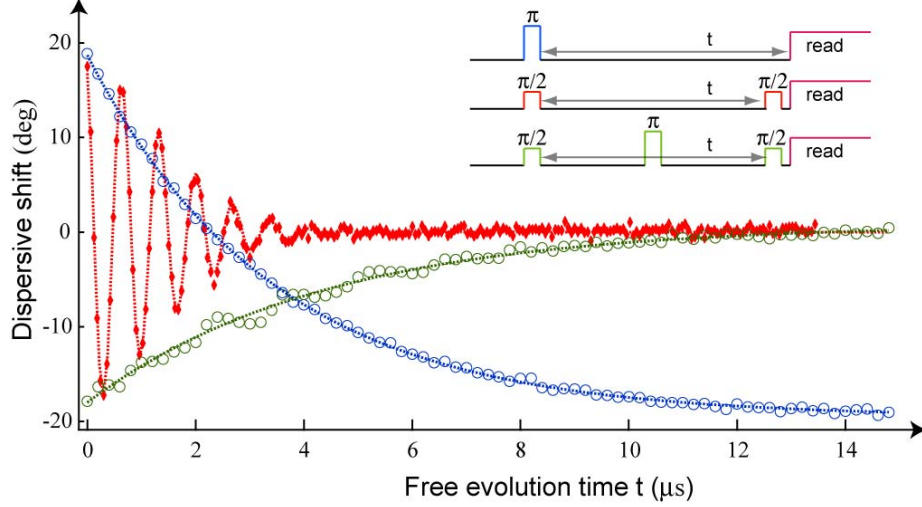


Figure 4-12: Evolution of the qubit after a π -pulse (blue), between two $\pi/2$ pulses, the Ramsey experiment (red) and between the two $\pi/2$ pulses with a π -pulse echo in between. The protocols are sketched in the right-top corner. Relaxation and echo signals are fitted to an exponential function, the decay of the Ramsey fringe is fitted to a gaussian.

No impurity transitions with frequencies below about 5 GHz were observed. Even very weakly coupled impurities show up in the qubit side-band transitions, offering a tool to investigate very weak impurities. Since the phase-drop across the array junctions is $1/N$ times smaller than that across the black-sheep, the coupling of impurities to the black-sheep junction phase or charge must be $N = 43$ times stronger than to the array junctions. So it is likely that all the impurity states observed in the spectrum come from the impurities located either in the black-sheep junction oxide or somewhere around the interdigitated coupling capacitances.

4.3 Time-domain decoherence measurement

The decoherence of fluxonium transitions was analyzed using three standard experiments, the relaxation after a π -pulse, the Ramsey fringes using two $\pi/2$ pulses and the π -pulse echo. Example data of such three-step characterization is shown in Fig. (4-12), the transition is $g \leftrightarrow e$ at about 5.3 GHz (see Fig. 4-7-B) corresponding to roughly $|\varphi_{\text{ext}}/2\pi| = 0.2$. In order to achieve the shown signal-to-noise, every experiment must be repeated about $1 - 2 \times 10^4$ times. The relaxation and the echo traces were measured using the interleaved pulse

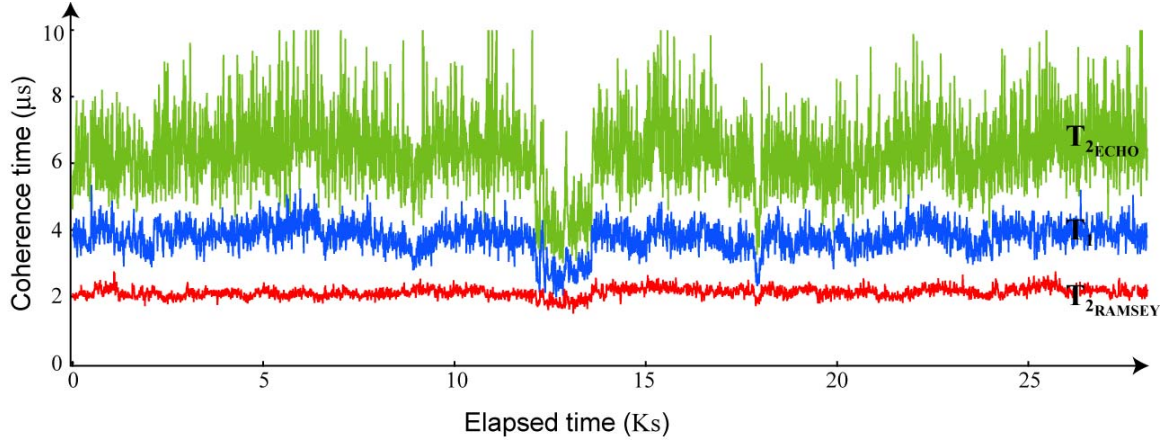


Figure 4-13: Measurement of T_1 (blue trace), $T_{2_{\text{RAMSEY}}}$ (red trace) and $T_{2_{\text{ECHO}}}$ (green trace) as a function of time. A set of three data points ($T_1, T_{2_{\text{RAMSEY}}}, T_{2_{\text{ECHO}}}$) was taken every 8 seconds.

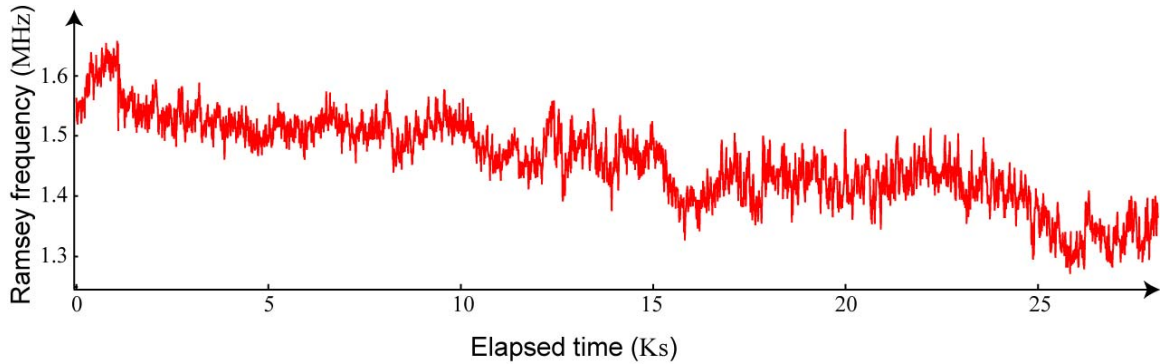


Figure 4-14: Ramsey fringe frequency measured as a function of time, using the same data set as in Fig. (4-13).

sequences, making the two traces as simultaneous, as possible in an averaging experiment. The Ramsey data was taken within a couple of minutes after the relaxation and the echo data acquisition finished. The π -pulse relaxation fits to an exponent with the characteristic decay time $T_1 = 3.5 \mu\text{s}$. The Ramsey fringe envelope fits to a gaussian with the decay time of $T_{2_{\text{RAMSEY}}} = 2 \mu\text{s}$, which means that some amount of pure dephasing is present. The echo signal decays also according to an exponent with the decay time of $T_{2_{\text{ECHO}}} = 4.5 \mu\text{s}$. This tells us that although some of the dephasing might be originating from noise slower than the $10 \mu\text{s}$ scale, the dominant decoherence mechanism for this particular transition and bias comes from energy relaxation.

Another interesting piece of information is the evolution of the three decoherence times with time, which we obtain by recording in an interleaved manner all three types of decoherence signals, approximately every 8 seconds. The relaxation time T_1 may fluctuate by as much as 50% on the time scale from several minutes to several hours. The decoherence time $T_{2\text{ECHO}}$ follows the T_1 , proving that it is mostly limited by the T_1 itself. Fluctuations in T_1 may be associated with many effects, starting from the fluctuations in the temperature of the circuit, and ending with the cosmic rays hypothesis. Since the Ramsey time $T_{2\text{RAMSEY}} \simeq 2 \mu\text{s}$ is considerably smaller than the maximum possible value of $2T_1 \simeq 8 \mu\text{s}$, the effect of fluctuations of T_1 by 50% contributes at most a 10% change in $T_{2\text{RAMSEY}}$. Therefore, the Ramsey time is very well defined and its flux dependence could be used for quantitative analysis. It is also interesting to look at the stability of Ramsey fringes frequency which, given the superb stability of our microwave sources, translates directly into the stability of the qubit frequency (Fig. 4-14).

Below in this section we investigate the behavior of the three times T_1 , $T_{2\text{RAMSEY}}$, and $T_{2\text{ECHO}}$ as a function of the external flux for the transitions $g \leftrightarrow e$ and $g \leftrightarrow f$.

4.3.1 Energy relaxation: fluxonium as a quantum spectrum analyzer

We have measured the lifetime T_1 of the $g \leftrightarrow e$ transition of the fluxonium as a function of external flux φ_{ext} , which, given the fluxon nature of the transition, directly translates into the frequency ν_{eg} (Fig. 4-15). Theoretically, the quantity T_1 is linked to the spectral density of noise which couples to the black-sheep junction phase φ according to Eq. (3.33). Since we know the matrix element $|\varphi_{eg}(\varphi_{\text{ext}})|$, the measurement of T_1 translates directly to the measurement of the real part of the environmental admittance Y shunting the black-sheep junction (Fig. 3-10). It is convenient to split the real part of the environmental admittance to the Purcell and the intrinsic contributions, by writing $\text{Re}[Y(\omega)]^{-1} = 1/(1/R_{\text{intrinsic}}(\omega) + 1/R_{\text{Purcell}}(\omega))$. Here $R_{\text{Purcell}}(\omega)$ is given by expression (3.34) and represents an inevitable dissipation introduced by the connection of the fluxonium circuit to the measurement leads. The intrinsic contribution $R_{\text{intrinsic}}(\omega)$ represents any source other than the measurement-leads-induced dissipation.

Our data shows that the energy relaxation is affected by R_{Purcell} only in a few hundred

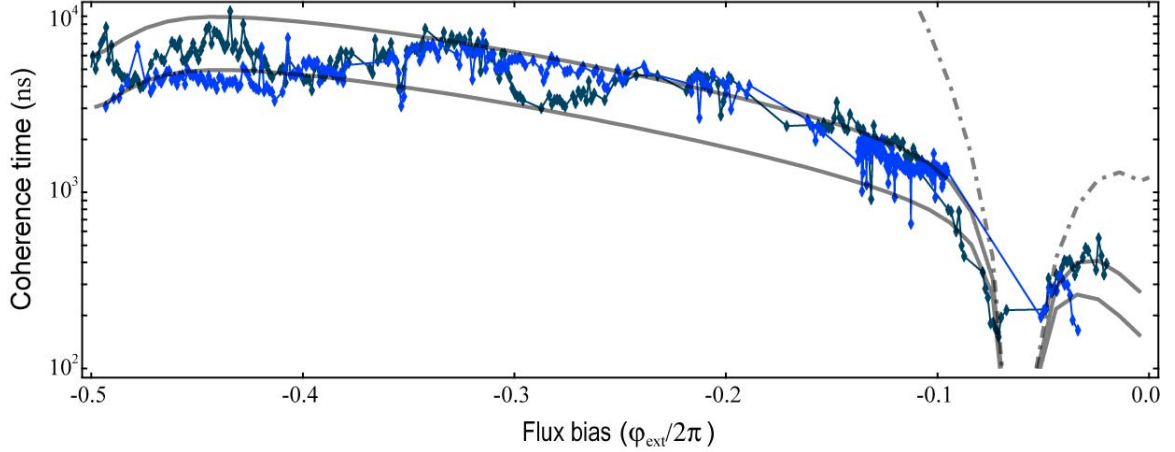


Figure 4-15: Two sets of energy relaxation data (T_1) measured for the $e \rightarrow g$ transition. The two data sets (bright blue and dark blue markers) correspond to thermal cycling of the device to about 77 K (see Fig. 4-10 and Fig. 4-11). Solid lines correspond to the intrinsic relaxation theory, one with $r_0 = 120 \text{ M}\Omega \times \text{GHz}$ and another with $r_0 = 240 \text{ M}\Omega \times \text{GHz}$. The dash-dot-dash line represents the Purcell contribution defined by Eq. (3.34).

MHz vicinity of the readout frequency ν_0 . Starting from the lowest frequency $\nu_{eg}(\varphi_{\text{ext}}/2\pi) = E_{SB}/h = 370 \text{ MHz}$ and up to about $\nu_{eg} \simeq 7.5 \text{ GHz}$ our measurement of T_1 actually performs the spectroscopy of the environment of the fluxonium over several frequency octaves. In other words, our Purcell-free qubit acts as a broad-band quantum spectrum analyzer. Perhaps the most interesting conclusion from our T_1 data is the extremely simple frequency dependence of $R_{\text{intrinsic}}(\omega)$ over the entire qubit frequency range. Namely, $R_{\text{intrinsic}}(\omega) = r_0/\omega$, where the quantity r_0 is in the interval $r_0 = 180 \pm 60 \text{ M}\Omega \times \text{GHz}$. Such $1/\omega$ frequency dependent resistance usually arises from the coupling to a large ensemble of discrete energy absorbers[50], whose microscopic origin is presently unclear [80]. Dissipation in the black sheep may likely come from dielectric losses in the coupling finger capacitors (Fig. 2-1). Interestingly, the inferred absolute value of $R_{\text{intrinsic}}$ matches well to that reported in other experiments with small-junction qubits [62]. Alternatively, but less plausibly, our energy relaxation data could be explained by a lossless black sheep and dissipation in the larger area junctions of the array, but with an r_0 factor $N = 43$ stronger (see Eq. 3.37).

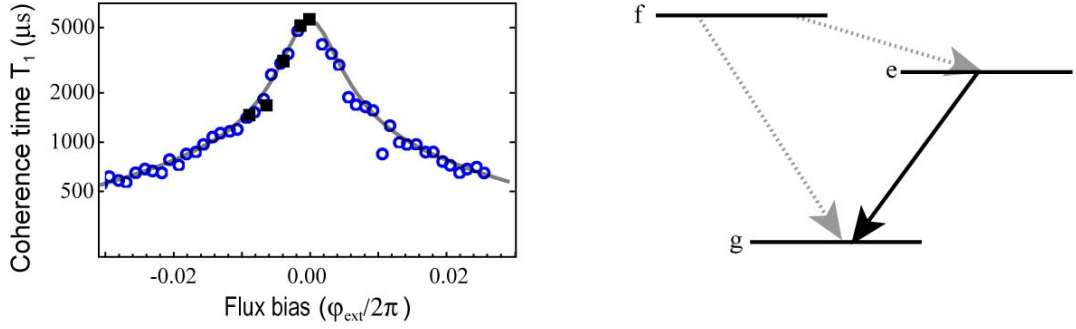


Figure 4-16: The T_1 sweet-spot at $\varphi_{\text{ext}} = 0$ of the $f \rightarrow e$ transition. Blue black markers represent the data measured by exciting the f -state directly. The solid line is a theory based on Eq. (4.5). Right: the three-level energy diagram explaining the relaxation dynamics. Direct transition $f \rightarrow g$ is weak due to parity selection rule, the intermediate transition $f \rightarrow e$ is weak because of the small frequency of this transition, and the transition $e \rightarrow g$ is so strong that could be considered instantaneous.

4.3.2 Energy relaxation sweet-spot

Transition $f \rightarrow g$ near $\varphi_{\text{ext}} = 0$ possesses a property worthy of mentioning: despite its fairly large frequency $\nu_{fg}(\varphi_{\text{ext}} = 0) \simeq 9.4$ GHz, at $\varphi_{\text{ext}} = 0$ this transition exhibits a sweet-spot for T_1 (Fig. 4-16). In the vicinity of $\varphi_{\text{ext}} = 0$, we have $\Gamma_{e \rightarrow g} \gg \Gamma_{f \rightarrow e}, \Gamma_{f \rightarrow g}$. In the two-step transition $f \rightarrow e \rightarrow g$ the step, $f \rightarrow e$, is the bottleneck ((Fig. 4-16-Right). Therefore, the relaxation time associated with the $f \rightarrow g$ transition can be written as $(T_1^{fg})^{-1} \simeq \Gamma_{f \rightarrow e} + \Gamma_{f \rightarrow g}$, and, neglecting the Purcell contribution, we get

$$(T_1^{fg})^{-1} \simeq 2 \frac{RQ}{R_{\text{intrinsic}}(\nu_{fg})} |\varphi_{fg}|^2 \nu_{fg} + 2 \frac{RQ}{R_{\text{intrinsic}}(\nu_{fe})} |\varphi_{fe}|^2 \nu_{fe} \frac{1}{1 - \exp\left(-\frac{h\nu_{fe}}{k_B T}\right)} \quad (4.5)$$

We dropped the temperature-dependent factor in the first term because, in our experiment, in the vicinity of $m_{\text{ext}} = 0$, the transition energies are such that $h\nu_{fe} \approx k_B T \ll h\nu_{fg}$. Once $k_B T \simeq h\nu_{fg}$, the relaxation process becomes more complicated.

Given the properties of the matrix elements φ_{fg} and φ_{fe} , and assuming the $1/\omega$ frequency dependence of $R_{\text{intrinsic}}$ we get the prediction that T_1^{fg} reaches maximum value at $\varphi_{\text{ext}} = 0$. Our data fully confirms this prediction, with the parameter $r_0 \approx 190 \text{ M}\Omega \times \text{GHz}$, in excellent agreement with the value extracted from the lifetimes of the $e \rightarrow g$ transition. We

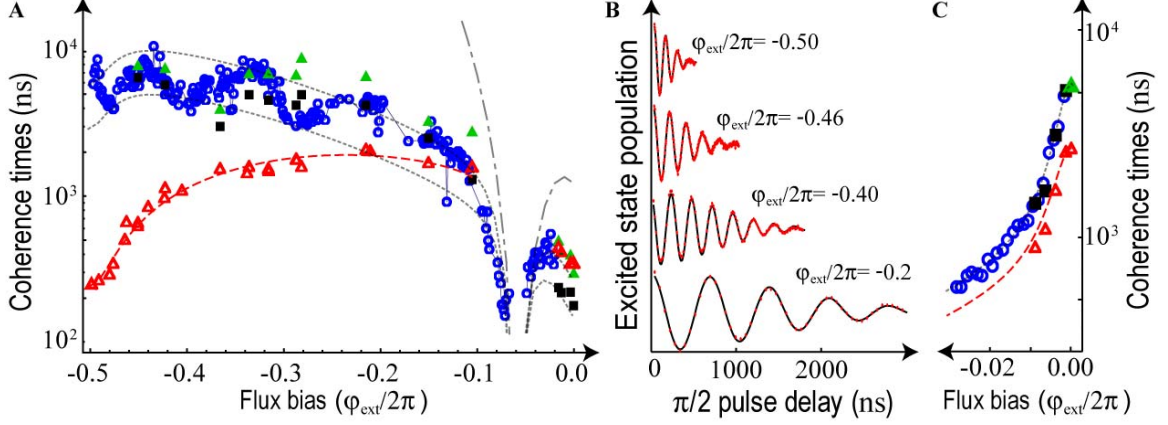


Figure 4-17: Summary of the fluxonium decoherence. (A) Relaxation data from Fig. (4-15) combined with Ramsey fringe times $T_{2\text{RAMSEY}}$ (red open triangles) and echoed times $T_{2\text{ECHO}}$ (green filled triangles). The dashed red line corresponds to the theory given by Eq. (3.46) with $|E_S|$ as an adjustable parameter. (B) Examples of Ramsey fringes. (C) Decoherence data for the transition $f \leftrightarrow g$, the relaxation data is taken from Fig. (4-16) and multiplied by two for easy comparison with T_2 data (green triangle) and T_{Ramsey} (red open triangles). The dashed red line is the dephasing theory also obtained from Eq. (3.46), without adjustable parameters.

emphasize that T_1^{fg} exhibits the local maximum at $\varphi_{\text{ext}} = 0$ specifically because of the $1/\omega$ frequency dependence of $R_{\text{intrinsic}}$. For instance, a $1/\omega^2$ frequency dependence would not fit the the shape of the T_1 -data, while frequency-independent $R_{\text{intrinsic}}$ would even produce a minimum in T_1 at $\varphi_{\text{ext}} = 0$ because of the properties of the matrix elements.

4.3.3 Dephasing

Finally we reach the main goal of the decoherence measurements – the flux-dependence of the dephasing times (Fig. 4-17). Dephasing times $T_{2\text{RAMSEY}}$, measured from the decay of Ramsey fringes, display a pronounced minimum of about 250 ns at the flux sweet-spot and spectacularly rise by almost an order of magnitude (Fig. 4-17-A), exceeding $2 \mu\text{s}$ at $|\varphi_{\text{ext}}/2\pi| \simeq 0.2$ ($\nu_{ge} = 5.5 \text{ GHz}$). Around $|\varphi_{\text{ext}}| = \pi$, the Ramsey fringes decay is well fitted with gaussian envelopes (Fig. 4-17-B), just like in the case of Fig. (4-12). This confirms the irrelevance of the energy relaxation for $|\varphi_{\text{ext}}/2\pi| < 0.2$, while it dominates at φ_{ext} close to zero. Coherence times $T_{2\text{ECHO}}$ obtained with echo experiments are drastically larger than $T_{2\text{RAMSEY}}$, particularly around $|\varphi_{\text{ext}}| = \pi$, and, for the most part, turn out to be limited by

energy relaxation. Therefore, the noise that causes Ramsey fringes to decay is slow on the time scale of about $50 \mu\text{s}$, but fast on the time scale of the typical Ramsey fringe acquisition time, of order one minute, typical of e -jumps seen with superconducting SET's and charge qubits [47, 51].

Obviously, flux noise cannot explain the observed anti-sweet-spot of $T_{2\text{RAMSEY}}$ at $|\varphi_{\text{ext}}| = \pi$ (see Eq. 3.39 and Fig. 1-16). However, the small discrepancy between $2T_1$ and $T_{2\text{ECHO}}$ at $|\varphi_{\text{ext}}/2\pi| \simeq 0.2$ results in a pure dephasing time $T_\phi > 35 \mu\text{s}$ and can be accounted for by a $1/f$ flux noise with amplitude of $2 \times 10^{-6} \Phi_0/\sqrt{\text{Hz}}@1 \text{ Hz}$, similar to that reported in flux qubit measurements[48]. Fluctuations in the array inductance are also ruled out because their effect is minimal at the $|\varphi_{\text{ext}}| = \pi$ half-flux quantum bias (the transition frequency is given by $|E_{SB}|$), and grows linearly towards zero flux, in contradiction with the data (see Eq. (3.40) and Fig. 3-12-B). Sensitivity to the critical current noise in the black sheep junction also cannot explain the data (see Eq. (3.41) and Fig. 3-12-A). Our key result is that the paradoxical flux-dependence of the dephasing time is well explained with the Aharonov-Casher effect. Upon subtraction of the small contribution from T_1 we find excellent agreement of $T_{2\text{RAMSEY}}(\varphi_{\text{ext}})$ with Eq. (3.46), with only one adjustable parameter, the $|\varphi_{\text{ext}}| = \pi$ value of $T_{2\text{RAMSEY}}$. Furthermore, this adjustable parameter agrees well with a WKB calculation of E_{S_j} (Eq. 1.16) based on our estimates of the array junction parameters (see Table 5.2)

As a control experiment, we measure coherence times of the second lowest, $g \leftrightarrow f$ transition in a narrow vicinity of $\varphi_{\text{ext}} = 0$ (Fig. 4-17-C), where the lifetime T_1 reaches $3 \mu\text{s}$. The Ramsey fringe measurement on this transition, at $\varphi_{\text{ext}} = 0$, still yields $T_{2\text{RAMSEY}} = 2.5 \mu\text{s}$, a significantly smaller value than $2T_1$. However, such discrepancy is again precisely accounted for by expression (3.46). In other words, both the $(250 \text{ ns})^{-1}$ linewidth of the $g \leftrightarrow e$ transition at $|\varphi_{\text{ext}}| = \pi$ and the $(2.5 \mu\text{s})^{-1}$ linewidth of the $g \leftrightarrow f$ at $\varphi_{\text{ext}} = 0$ are linked without any adjustable parameter. Echo measurement at $\varphi_{\text{ext}} = 0$ yields a $T_{2\text{ECHO}}$ almost matching $2T_1$ with pure dephasing times $T_\phi > 50 \mu\text{s}$. Taking this number and assuming a $1/f$ character of possible array inductance fluctuations, we estimate using Eq. (3.40) that its amplitude must be smaller than $3 \times 10^{-6} L/\sqrt{\text{Hz}}@1 \text{ Hz}$.

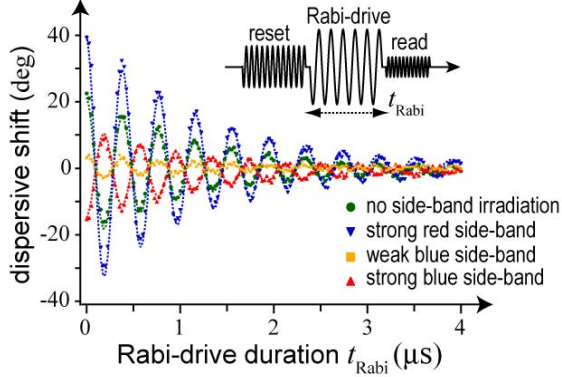


Figure 4-18: Demonstration of population inversion of the fluxonium transition at $\varphi_{\text{ext}} \simeq \pi$. Four types of reset pulses are applied followed by the Rabi pulse of variable duration, and then the readout pulse. The reset pulse corresponds to either red or blue side-band irradiation.

4.4 Bonus track

Here we present experiments which do not aim at testing the superinductance with fluxonium circuit, but rather explore several phenomena useful to the superconducting qubit community in general.

4.4.1 Optical pumping and population inversion

At $|\varphi_{\text{ext}}| = \pi$, the fluxonium $g \leftrightarrow e$ transition energy, given by E_{SB} is comparable to the thermal energy. Therefore, in equilibrium, both qubit states g and e are populated. We can offset these populations using the side-band transitions with the readout resonator, taking advantage of the fact that the lifetime of the excitation in the resonator (about 50 ns) is much shorter than the T_1 time of the qubit (about 5 μs). The population of the excited state e can be reduced by irradiating the circuit at the frequency of the red side-band, while the population of the g state can be reduced by irradiating at the frequency of the blue side-band (Fig. 4-9).

Following this idea [81, 82], we performed Rabi oscillation of the qubit $g \leftrightarrow e$ transition, after it is reset by a side-band irradiation (Fig. 4-18). With no reset irradiation we get Rabi-oscillations with some contrast and decay time of about 1 μs . Irradiating the red side-band with some optimum power results in Rabi-oscillations with improved contrast with the same

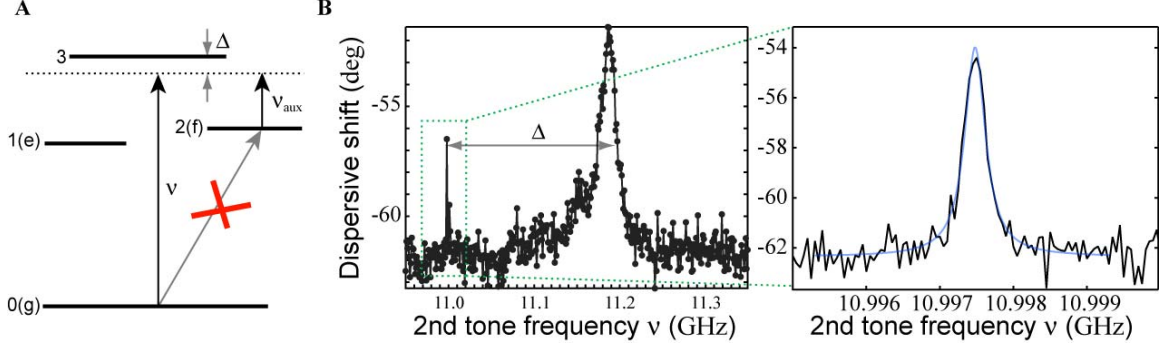


Figure 4-19: (A) Transition structure of fluxonium at $\varphi_{\text{ext}} \simeq 0$. Transition $0(g) \leftrightarrow 2(f)$ is suppressed due to the parity conservation at $\varphi_{\text{ext}} \simeq 0$. Instead, two continuous tones are applied, to connect state 0 to the state 2 via the state 3. Transitions $0 \leftrightarrow 3$ and $2 \leftrightarrow 3$ are parity allowed. (B) Resulting Raman spectroscopy signal. Large resonance corresponds to direct excitation of $0 \leftrightarrow 3$ transition, while the narrow line corresponds to the forbidden $0 \leftrightarrow 2$.

coherence time. The maximum contrast improvement by a factor of about 1.5 is consistent with the assumption of vanishing excited state population $P_e \simeq 0$ and $T \simeq 15$ mK. Changing to the blue side-band irradiation for a resetting pulse, we observe that contrast vanishes as one applies some sufficiently large power. Moreover, further increasing the reset irradiating power, the contrast of Rabi oscillation inverts, which means that we have prepared the population inversion of the qubit states. This technique is analogous to the well-known optical pumping[81]. More work is needed for high-fidelity qubit state preparation using this method.

4.4.2 Raman excitation of forbidden fluxonium transition

Irrespective of fluxonium parameters, the transition $g \leftrightarrow f$ is forbidden at $\varphi_{\text{ext}} = 0$ due to the symmetry of the hamiltonian (3.1) with respect to $\varphi \leftrightarrow -\varphi$ (see Fig. 3-2-B,E and Fig. 4-8-Inset). Given the long T_1 of the f -state (Fig. 4-16) the transition $g \leftrightarrow f$ looks attractive for quantum manipulations. Although the direct driving is forbidden, the f -state can be excited via a Raman process involving two tones and another state to which transitions are allowed from both states g and f . An example of a Raman scheme is illustrated in Fig. (4-19-A). We apply a CW tone at the frequency $\nu_{\text{aux}} = \nu_{32(f)} - \Delta$, where Δ makes sure the transition $2(f) \leftrightarrow 3$ is not driven resonantly. In order to transfer coherently the population

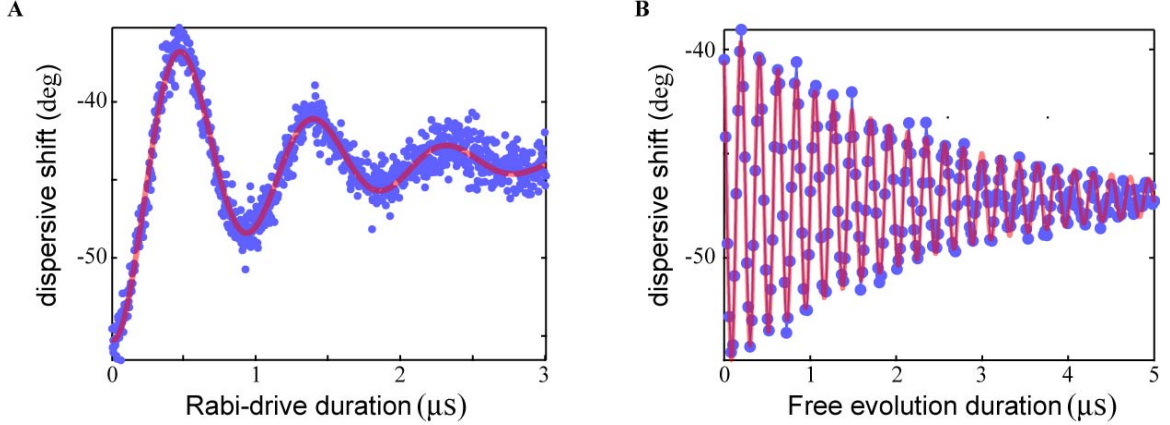


Figure 4-20: Time-domain Raman experiment. Rabi oscillations and Ramsey fringes of the $0 \leftrightarrow 2$ transition measured the pulsed Raman tones from the previous figure.

from the ground state g to the state f we apply another tone (which could be pulsed for discrete rotations) at the frequency $\nu = \nu_{30(g)} - \Delta$ ([83, 72]). By choosing Δ sufficiently large we excite state $2(f)$ without exciting the intermediate state 3. We have performed the Raman spectroscopy by choosing $\Delta \simeq 200$ MHz and scanning continuously the second tone frequency ν . When $\nu = \nu_{30(f)}$ we encounter a broad resonance corresponding to the direct excitation of the 3 state, which is not forbidden by the symmetry. However, at a slightly smaller frequency we find a narrow resonance which corresponds to the excitation of the forbidden $g \leftrightarrow f$ transition via the Raman process involving the state 3.

Combining the standard Rabi protocol with our Raman scheme (first tone at the frequency ν_{aux} is fixed, second tone at frequency ν is pulsed), we indeed observe coherent oscillations at frequencies up to several MHz (Fig. 4-20-A). Having extracted the parameters of the $\pi/2$ pulse from the Rabi oscillations, we implement the Ramsey protocol and indeed observe the Ramsey fringes. The decay time of the fringes is about $T_{2\text{RAMSEY}} = 2.5 \mu\text{s}$ and is compatible with the value we measured using a high-power direct driving slightly away from the symmetry point (Fig. 4-17-C). This proves that the Raman protocol is efficiently exciting the forbidden transition without the loss of coherence to the helper state 3.

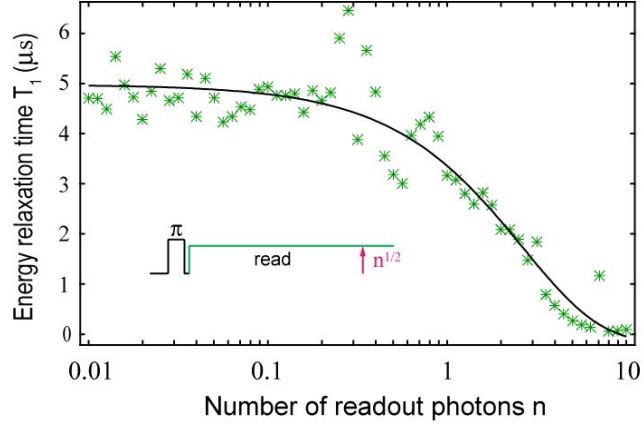


Figure 4-21: Life-time of the qubit state measured as a function of the average cavity photon population n . The protocol consists of exciting the qubit by a π -pulse and monitoring continuously the heterodyne signal of the readout. Solid line is a fit to $T_1 = T_1(n = 0) \exp(-n/n_{\text{crit}})$.

4.4.3 Suppression of qubit life-time by the readout photons

Theory of dispersive readout predicts a relaxation time independent of the readout photon number n . However, we find that the lifetime of the qubit transition, decaying *while* the resonator is populated with photons, drastically decreases with n (Fig. 4-21). The measured dependence of $T_1(n)$ can roughly be approximated as $T_1(n) = \exp(-n/n_{\text{crit}})$ where $n_{\text{crit}} \approx 1$. Essentially, we find that once the readout is performed using more than 1 photon, our readout scheme quickly loses its quantum non-demolition character. This effect is responsible for sub-single shot performance of our dispersive readout, despite its immunity to Purcell effect. More experiments and theoretical analysis [84] are needed to understand this effect.

Chapter 5

Conclusions and perspectives

5.1 Availability of superinductance

The main results of this thesis work can be summarized with the following technical specs of the available Josephson array superinductance (operation temperature 15 mK):

Self-resonance frequency $\omega_{\max}/2\pi$	$\omega_{\max}/2\pi > 12 \text{ GHz}$
Impedance at $\omega_{\max}/2\pi$	$\omega_{\max}L > 22 \text{ k}\Omega > 3R_Q$
Dissipation (shunting resistance model) at $\omega_{\max}/2\pi$	$R > 20 \text{ M}\Omega$
CQPS frequency	$ E_S /h \simeq 1 \text{ MHz}$
Low-frequency L -noise (assuming $1/f$ character)	$\delta L/L < 3 \times 10^{-6}/\sqrt{\text{Hz}}@1 \text{ Hz}$

Table 5.1: Specs of the in-stock Josephson array superinductance

Later experiments on new fluxonium devices (not included into this thesis) showed that the CQPS amplitude could be suppressed by an order of magnitude, simply by increasing the ratio $E_{J_{j \neq 0}}/E_{C_{j \neq 0}}$ by about a factor of 2. This is indeed expected due to the exponential sensitivity of the CQPS frequency (Eq. 1.16) on this parameter. We thus conclude that the coherent quantum phase-slip process places almost no limit on the product $\omega_{\max}L$. Instead, this product is limited by the effect of shunting the inductance by the vacuum, which translates (see Eq. 1.7) into a limit on the maximum number of junctions N , such that $N \lesssim \sqrt{C_J/C_g}$. In our experiments, $N = 43$. New experimental tricks of reducing the ratio of island to junction capacitances C_g/C_J , for instance by stacking the junctions vertically, instead of horizontally as in the present work, will help to further increase the

ratio $\omega_{\max}L/R_Q$ beyond the presently achieved factor of 3.

Another recent experiment [85] suggests that the measured $R_{\text{intrinsic}}$ in our experiment is likely to come from the coupling finger capacitors of the fluxonium circuit, rather than from the dissipation inside the array junctions. Therefore, the energy relaxation of the fluxonium circuit may be much improved by switching from capacitive coupling to inductive coupling, or by reducing the losses in the interdigitated capacitances.

Let us also remark on the low-frequency stability of our superinductance. Although our implementation contains $N \gg 1$ junctions, all with a possibly fluctuating in time L_{J_j} (critical current noise!), the total array inductance L will probably fluctuate by a fractional factor of $N^{-1/2}$ less, due to a statistical argument. Indeed, since $\delta L = \sum_{j=1}^N \delta L_{J_j}$, and assuming that junctions fluctuate independently, we conclude that $\delta L^2 = N \times \delta L_{J_j}^2$, and $\delta L/L \simeq N^{-1/2} \times \delta L_{J_j}/L_{J_j}$. Our measurement of the dephasing times of the fluxonium circuit places an upper bound on the low-frequency noise in L , which however may be much overestimated.

Finally, the fluxonium circuit, developed in the present work to test superinductance of the Josephson junction array, is equally suitable for testing other possible implementations of superinductances, for instance using thin films of high-kinetic inductance superconductors [28], like Ti, NbN, etc. If developed, such superinductances may be useful in applications requiring higher operation temperatures and/or magnetic fields, compared to Al based junctions. If ultrathin superconducting nanowires indeed undergo the coherent quantum phase-slip process, one will resolve this phenomenon by replacing the junction array of the fluxonium circuit by a “slippery” nanowire of similar kinetic inductance. By measuring the decoherence times T_2^* and T_2 as a function of external flux, a quantum phase-slip frequency as low as 100 KHz can be resolved, provided that replacing our array with a wire does not reduce T_1 of the fluxonium transitions [86].

5.2 Offset-charge free quantum Josephson networks?

Networks of Josephson junctions attracted much interest in the past, because by playing with the network geometry, flux frustration, and parameters E_J and E_C , one may model

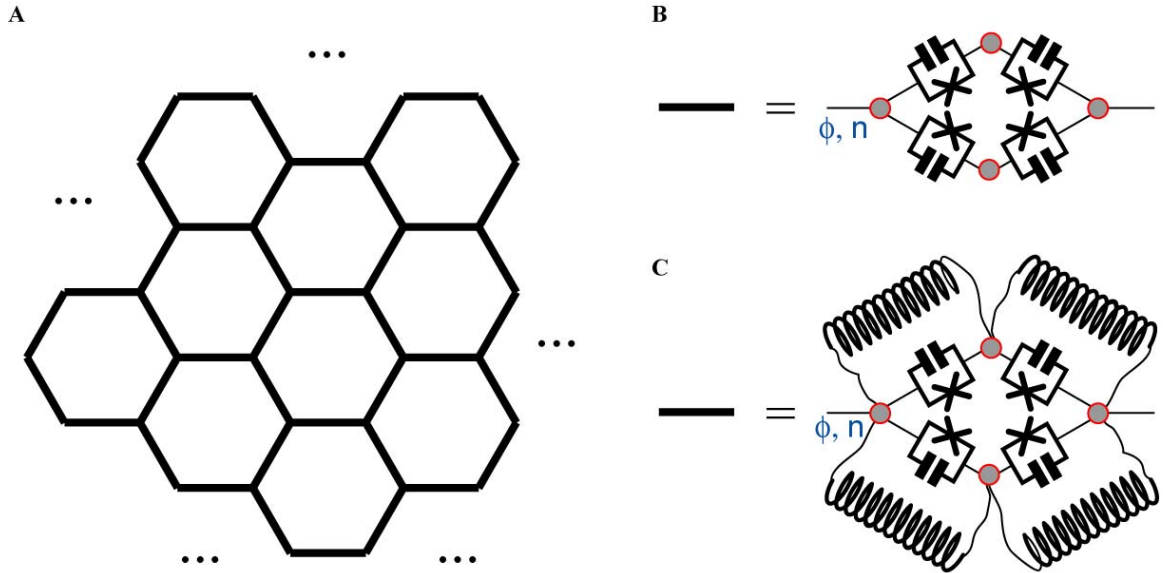


Figure 5-1: Example of a Josephson network whose ground state is protected by a topological degeneracy (A, B). The boundary of the network must be designed properly and is not shown on the figure. The topological ground state is protected by a gap associated with the strong quantum fluctuations of phase, and thus scales as $\exp(-\alpha\sqrt{E_J/E_C})$, where α is of order unity. Therefore, the circuit is sensitive to offset charges. An entirely new circuit (C) could be derived from this one by shunting every junction with a superinductance. Quantum fluctuations of phase in the new offset-free circuit are still as strong as in the previous one.

with such networks the ground states of certain many-body physics models, as well as quantum phase transitions between those ground states [87, 88]. Quite generally, if every Josephson junction in the network is shunted by a huge capacitance, the phase across the junction would not fluctuate quantum-mechanically, and the entire network will act as a superconducting chicken-wire. Quantum effects appear when one reduces the E_J/E_C ratio of the junctions to a number of order unity. However, for $E_J/E_C \sim 1$, every node in the circuit is an island susceptible to offset charges. Offset charges enter the hamiltonian of the circuit and alter its ground state. In fact, some very interesting effects have been proposed for charge-frustrated networks [89]. However, in an experiment, offset charges fluctuate by an amount of order unity (both in space and in time), mostly due to poor parity conservation of superconducting islands [47, 51, 86]. Therefore, we are facing a dilemma: either study networks of junctions with $E_J/E_C \gg 1$ with no offset charges but also with very weak quantum effects, or study a network of junctions with $E_J/E_C \sim 1$ and nominally strong quantum effects, however accompanied by a strong offset-charge disorder. It is hard to treat such charge disorder, and it is likely that it simply kills all the interesting properties of the circuits in the regime of large fluctuations of island phase, $\delta\phi \sim \delta n \sim 1$.

The availability of superinductance suggests to consider a new type of Josephson network of junctions with $E_J/E_C \sim 1$, but where every island is shunted to another one by a superinductance (Fig. 5-1). In such a network, we still expect strong quantum effects, since $\delta\phi \sim \delta n \sim 1$ for every island, but there will be zero effect of offset charge disorder, thanks to the superinductive shunt. In some sense, the fluxonium qubit is the most elemental example of the kind of network we describe. We expect that such networks, when cleverly chosen, would exhibit interesting quantum collective order.

5.3 Processing quantum information with fluxonium qubits

Here we speculate on the use of the fluxonium circuit as a qubit. With its combination of fluxon and plasmon transitions, the fluxonium is probably the first artificial atom which resembles a Λ -atom (in very broad sense), the 3-level workhorse of modern atomic physics (see Ref. [90] and references therein).

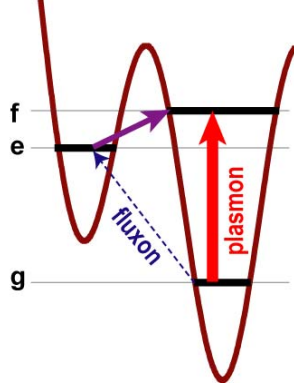


Figure 5-2: First three states and transitions of a fluxonium qubit with typical parameters.

In a Λ -atom, there are at least three levels, g , e , and f , with special transition structure. The long-lived qubit transition $g \leftrightarrow e$ is coupled poorly to electromagnetic fields because of some conservation law, usually either a magneto-dipole selection rule or a quadrupole selection rule. The weakly coupled transition is nevertheless accessed for both readout and qubit-qubit coupling with the help of an auxiliary transition involving the third level, either $g \leftrightarrow f$ or $e \leftrightarrow f$, which carries large transition dipole moment (usually a regular orbital motion transition). Similarly, in fluxonium circuit, the fluxon transition is suppressed by flux quantization, as long as the flux bias is away from the $\varphi_{\text{ext}} = \pi$, and therefore takes the role of the qubit transition. The plasmon transition has a large transition dipole moment, and therefore takes the role of the coupling transition.

We believe that the Λ -spectrum of fluxonium artificial atom is potentially a very useful resource for quantum information processing with quantum superconducting circuits. We illustrate some possible options below.

5.3.1 QND state monitoring

We have established experimentally that the readout of the present fluxonium circuit causes essentially no Purcell effect (see Fig. 4-15 and discussion around it), because the dispersive shift χ_{eg} (see Eq. 3.16) could be large for arbitrary large detuning between the qubit and the cavity transitions, as long as the cavity transition is close to the plasmon transition. One can adjust the parameters of the fluxonium and its readout to fully make use of this wonderful effect to enhance considerably the SNR of the state readout. We propose the

following recipe. First, suppress the fluxon transition relaxation times, by reducing the parameter E_{SB} from about 350 MHz in the present device to about $E_{SB} = 100$ MHz. Since $T_1 \propto E_{SB}^{-2}$ (Eq. 3.31 and 3.7), the T_1 would rise by a factor of 10. Second, choose the readout frequency to be about few hundred MHz above the plasmon frequency. This would ensure the values of χ_{eg} to be in the several 10's of MHz (Eq. 3.25). Furthermore, at flux bias close to the various readout resonances (poles in the χ_{eg}), the value of χ_{eg} can be as high as 100 MHz (see Fig. 3-7). For the device parameters of Fig. (3-7), we need the resonator frequency of about $\nu_0 = 16$ GHz, which is not limited by the presently available components. In principle, one can also scale down the plasma frequency. Finally, let us tune the linewidth of the readout resonance to the value above the maximum value of χ_{eg} , to work with phase shift of about 1 rad. This would correspond to reducing the quality factor from the present $Q = 400$ to the 5 times smaller value of $Q = 80$. This way, the total power P_R emitted by the cavity populated with only one photon, and given by $P_R = h\nu_0 \times \nu_0/Q$, grows by a factor of 20 compared to the present setup. Combined with an increased life-time, we expect an increase in a signal-to-noise by a factor of 100 with a properly designed fluxonium and readout parameters.

A 100-fold enhancement of SNR may facilitate observation of quantum jumps with a single readout photon and possibly other interesting experiments with QND measurement. Incorporation of the recently developed JPC amplifier should further increase the SNR by another factor of 10 with the corresponding exciting consequences. Recent advances in the observation of quantum jumps with the transmon qubit and a parametric amplifier [91] greatly encourage us to explore quantum measurement physics with fluxonium qubits.

Finally, let us remark that χ_{eg} not only has poles, but also zeros (see Eq. 3.16, Fig. 3-7, and Fig. 4-7-B). Tuning the flux to a zero of χ_{eg} provides an efficient way to decouple the qubit completely from the measurement action of the readout.

5.3.2 Controlled qubit-qubit interaction schemes

A satisfactory solution of the qubit-qubit coupling for fluxonium circuits goes beyond the scope of the present thesis work. However, to encourage future efforts in this direction, we share here some ideas on how this coupling can be implemented in practice and how the

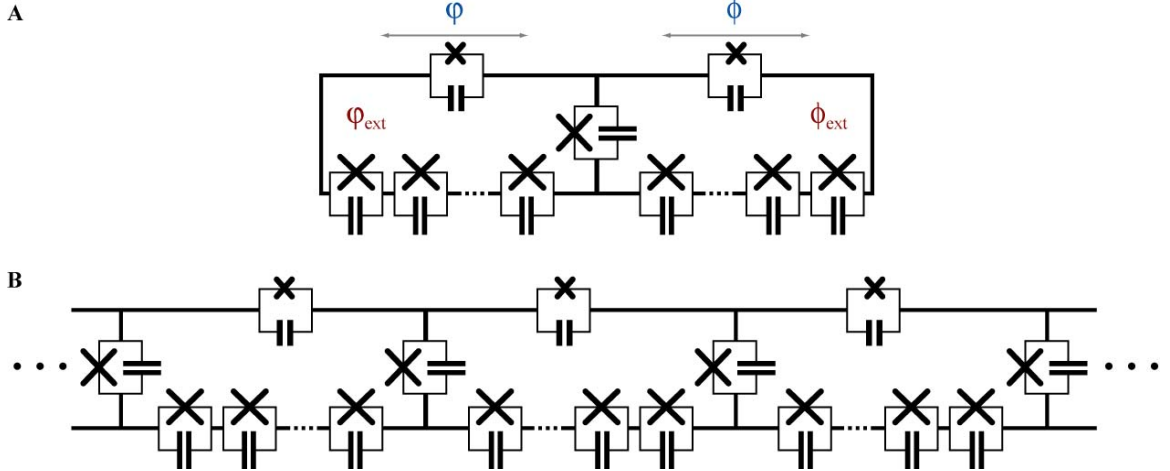


Figure 5-3: Inductive coupling of fluxonium qubits by a common array junction (A). Qubits interact when the two bias fluxes are tuned according to $\phi_{\text{ext}} = \varphi_{\text{ext}} = \pi$, and are practically decoupled for $\phi_{\text{ext}} = \varphi_{\text{ext}} \simeq \pi/2$. Qubits can be arranged into a chain for nearest-neighbor exchange (B). Magnetic coupling via vacuum is suppressed by at least 10^4 due to the huge difference between kinetic and geometric inductances.

features of the fluxonium circuit may be helpful with inventing new coupling tricks.

First of all, let us remark that one can at first forget about the Λ -spectrum and use only the two lowest fluxon states of fluxonium circuit. In view of formulas (3.7) and (3.9), by choosing the value E_S to be not too small (say $E_S/h = 2 - 4$ GHz), one can couple fluxoniums either capacitively or inductively via a cavity bus, in the same manner it was done with the transmons [92, 93, 94] and with similar coupling rates. However, making E_S large kills the Λ -ness of the fluxonium spectrum, because the lifetime of the fluxon transition would decrease, for the same material quality. We are then back to the same types of energy relaxation problems as transmon qubits experience [62]. In this situation, fluxonium with a large E_S may still be advantageous for multiple qubit circuits, because of its very small size (Fig. 2-1) compared to the transmon and phase qubits.

It is much more interesting and, hopefully, useful, to devise a qubit-qubit interaction scheme for fluxoniums with a small E_S , say keeping $E_S \simeq 100$ MHz. For such small E_S the charge matrix element, n_{eg} is very small, $n_{eg} < 10^{-2}$ ($n_{eg} \approx 1$ for the transmon or phase qubit), irrespective of the flux bias (Eq. 3.9), which means that such transitions would interact very weakly with a cavity, and even weaker with another qubit.

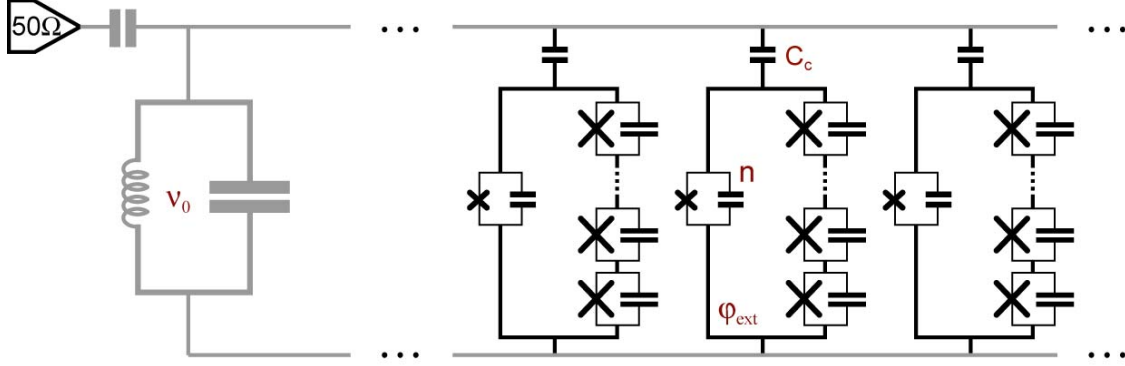


Figure 5-4: A cluster of fluxonium qubits is connected capacitively to a readout resonator. Cavity frequency ν_0 must be chosen slightly above the plasmon transition frequency. Qubits interact strongly via the plasmon transitions through the cavity. The coupling of plasmon transition to the cavity vanishes for $\varphi_{\text{ext}} = \pi$.

One simple coupling scheme appears to be readily available for the fluxoniums coupled via a mutual inductance, with the coupling energy operator $V = E_{L_c} \phi \phi$, where $E_{L_c} = (\Phi_0/2\pi)^2/2L_c$, L_c is the effective coupling inductance, ϕ and φ are the phase variables of the two circuits. The coupling inductance must be provided with, say a common single array junction, so that $E_{L_c} \simeq E_L/N \simeq 10$ MHz. When both qubits are tuned to their degeneracy point at $\varphi_{\text{ext}}, \phi_{\text{ext}} = \pi$, they will swap at the rate $\nu_{\text{swap}} \simeq E_{L_c} \varphi_{eg}(\varphi_{\text{ext}} = \pi) \phi_{eg}(\phi_{\text{ext}} = \pi) = \pi^2 E_{L_c} \simeq 100$ MHz. This rate could be suppressed to below 1 kHz level by simply tuning the flux away to, say, $\varphi_{\text{ext}} \approx \pi/2$, and making sure that the qubit transition frequencies are differing by as little as 10 MHz. One can imagine connecting flux qubits in a chain and play some nearest-neighbor exchange games [95]. We emphasize that such a coupling scheme would not work with conventional flux qubits, because contrary to fluxoniums, flux qubits decohere rapidly away from the sweet spot [48].

More interesting and novel coupling schemes would likely include the plasmon transition. Interestingly, the plasmon transition by itself is a very interesting candidate for a qubit transition. First of all, the plasmon frequency does not depend on flux much, even for not so small E_S ($E_S = 370$ MHz, in present work). When the two fluxoniums are placed in a cavity, with a resonance frequency located slightly above the plasmon frequency, the plasmon transitions would be coupled strongly by a flip-flop interaction virtually via the cavity. The rate of flip-flops should reach as much as 100 MHz, given how strongly the

plasmons couple to the cavity in the present work (Fig. 4-9). Crucially, we can switch off completely this flip-flop interaction between two plasmon transitions, simply by tuning the flux bias to the degeneracy point, $\varphi_{\text{ext}} = \pi$. Indeed, both $\varphi_{ef} = 0$ and $n_{ef} = 0$ at $\varphi_{\text{ext}} = \pi$ due to parity conservation.

So, the $g \leftrightarrow f$ plasmon transitions of the two fluxoniums, connected to the same cavity either capacitively or inductively, could interact strongly and tunably. In principle, one can just employ such transition for a qubit. A neat feature of the plasmon transition is that although its frequency depends very weakly on the external flux, one can switch off this transition simply by tuning the circuit to the sweet-spot $\varphi_{\text{ext}} = \pi$. Although in the currently measured fluxonium devices the plasmon transition was not long-lived ($T_1 \simeq 100$ ns, data not shown here), it would likely improve to the level of the present Yale transmons (several μs), if we just move the readout frequency above the plasmon frequency (in this experiment $\nu_0 \approx 8$ GHz, while $\nu_p \approx 12$ GHz). Thus, fluxonium can act as a transmon, but with an important improvement: (i) the qubit transition is nearly flux-independent, therefore decoherence due to flux noise is virtually eliminated, (ii) despite the fixed frequency, the coupling of a qubit to a cavity bus could be flux-tuned down to zero, thanks to the parity selection rule.

Finally, the sweetest coupling scheme would probably take advantage of the long-lived fluxon transition for storing the qubit state and use the strongly coupled plasmon transition for implementing quantum gates with another fluxonium, perhaps in the spirit of the Cirac-Zoller gate for trapped ions [96].

5.4 Bloch oscillations and quantum metrology of electrical current

Our original motivation to implement a superinductance circuit element comes from the idea of quantum metrology of electrical current. One of the present goals of quantum metrologists is to construct an electrical circuit, in which a direct current I is linked to the frequency f of some electrical signal by a constant e^* , that is

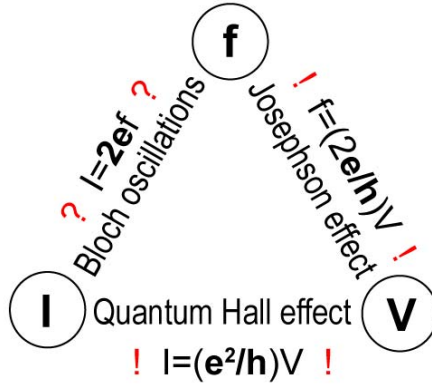


Figure 5-5: The quantum metrology triangle. Josephson effect and the quantum Hall effect link constant voltage (1 V scale) to frequency (1 GHz scale) and to current (1 nA scale), respectively. An effect linking directly current to frequency would close the metrology triangle and would eventually allow self-consistent definition of SI units in terms of fundamental constants of Nature only.

$$I = e^* \times f \tag{5.1}$$

where e^* is some well defined multiple or a fraction of the elementary charge e . Such an effect may serve to redefine the Ampere in a purely electrical experiment, since the unit of frequency is now defined much better than 10^{-16} owing to the atomic clock technology [97]. When combined with the Josephson [64, 98] and quantum Hall effects [99, 100], which link voltage to frequency and voltage to current, respectively, the “ $I = e^* \times f$ ” effect will close the so-called “quantum metrology triangle” [101]. This eventually will redefine all physical units of SI in terms of the unit of time and the fundamental constants of nature – e , h , and c (this one links time to distance via interferometry).

Here we discuss a particular case of the “ $I = e^* \times f$ ” metrological effect, known as Bloch oscillations in a single Josephson junction [4], with $e^* = 2e$. It has been proposed that biasing a small-capacitance Josephson tunnel junction with an ideal current source results in an oscillatory voltage across the junction. Oscillations are generated due to quantum-mechanical motion of the Josephson phase in a tilted periodic Josephson potential, in analogy with the Bloch oscillations of an electron moving in a crystal potential under application of a uniform electric field[102]. In its essence, Bloch oscillations is a coherent

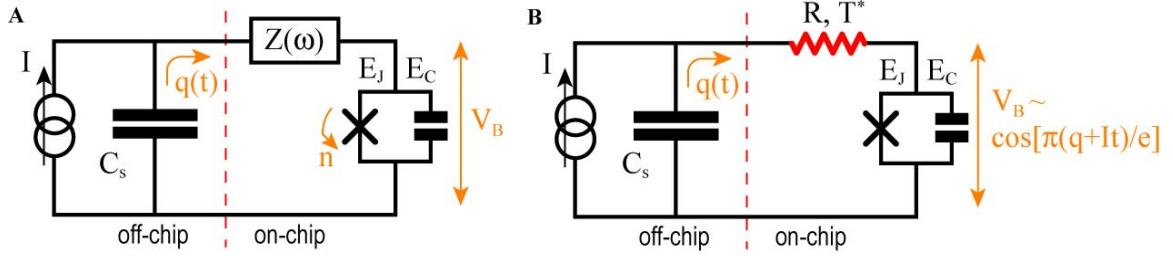


Figure 5-6: Traditional Bloch-oscillating circuits, (A) general, (B) with an on-chip resistor $R \gg R_Q$. Circuits generically have two variables: n , the number of Cooper pairs tunneled through the junction and q the charge flowing in the bias impedance Z in addition to the externally imposed It .

single-charging effect. It could be viewed as a dual to the Josephson oscillations. Indeed, Josephson oscillations correspond to oscillations with the frequency f of the current through the junction, which is biased with a perfect voltage source V , so that $V = \Phi_0 f$, a key effect to define the unit of voltage through the unit of frequency.

The purpose of this section is to describe a possible path to implement experimentally the “ideal” current bias for observing and utilizing Bloch oscillations. We argue that i) the superinductance in series with a small Josephson junction protects the junction from the high-frequency quantum noise of the necessarily low-impedance (see Eq. 1.2 and discussion around it) off-chip electromagnetic environment, and ii) the back-action of the readout circuit provides the necessary damping to stabilize Bloch oscillations against the low-frequency thermal noise of the same low-impedance environment.

5.4.1 “Orthodox” Bloch oscillations

Before describing our proposal of implementing Bloch oscillations, let us provide a summary of why this phenomenon is so hard to observe and utilize [5, 103, 104].

The minimal electrical circuit (Fig. 5-6) to model a realistic experimental situation contains a small Josephson junction defined by its Josephson energy E_J and charging energy E_C , such that $E_C \approx E_J \gg k_B T$; the frequency-dependent impedance $Z(\omega)$, modeling the on-chip electromagnetic environment of the junction; the stray capacitance C_s , modeling the low-impedance off-chip environment. In an ideal-world $C_s = 0$ and $Z = 0$, and the phenomenon of Bloch oscillations can be understood as a response of a Cooper pair box on

a uniformly ramped offset charge[7]. Indeed, the circuit would be described by the number n of Cooper pairs tunneled through the junction and the conjugate phase φ across the junction. The ground state energy E_0 of such Cooper pair box depends periodically on the offset charge n_{offset} . For $E_J \gtrsim E_C$ it is safe to approximate $E_0(n_{\text{offset}}) \simeq \epsilon \cos 2\pi n_{\text{offset}}$, where the parameter dependence of ϵ is given by¹ Eq. (1.16). In the ideal world, the offset charge is rigidly imposed, $n_{\text{offset}} = It/2e$, so the voltage across the current-biased junction (in its ground state) oscillates in time with a period $I/2e$:

$$V_B(t) = -dE_0/d(2en_{\text{offset}}) = (\pi\epsilon/e) \sin \pi It/e \quad (5.2)$$

The maximum frequency of oscillations is limited by the Landau-Zener transitions to the excited state of the Cooper pair box spectrum. Since in the limit $E_J \gtrsim E_C$ the quantity $E_1 - E_0 \gg E_J$, the system will remain in its ground state as long as $I/2e < E_J/h$. Since a realistic value for E_J of small junctions can reach 10 GHz we conclude that the much desired “ $I = e^* \times f$ ” effect is possible with the frequency f in the GHz range and, therefore, currents I in the nA range.

In the real world, however, the capacitance C_s is non-zero, so the current-bias is imperfect. The capacitance C_s is associated with the connection of the junction to the macroscopic current-sourcing instrument. The realistic value of the capacitance C_s is such that $C_s > 1$ pF and the associated charging energy $E_{C_s} = e^2/2C_s$ is very small, $E_{C_s} \ll E_C, k_B T$. Clearly, in order to protect charging effects in the small junction from being shunted by the capacitance C_s , we need to insert a finite impedance Z into the leads of the small junction. It turns out, the requirements on this impedance are very hard to meet in an experiment. Moreover, there are two types of challenges – the “quantum” one, and the “classical” one.

The “quantum” challenge could be illustrated in the following way, assuming $T = 0$. The presence of finite Z introduces a second circuit variable q , which is the charge on the capacitance C_s , and which we shall call an environmental charge². This charge is added to the total offset charge of the Cooper pair box, $n_{\text{offset}} = (It + q)/2e$, so that n_{offset} fluctuates,

¹Although ϵ is suppressed exponentially with the ratio $(E_J/E_C)^{1/2}$, one can still obtain sizable $\epsilon \approx \hbar\omega_p/5 \approx 2 - 4$ GHz.

²Usually the quantity $It + q$ is called a quasicharge, by an analogy with the quasi-momentum of an electron in crystal potential and in the presence of a constant electric field.

in general, quantum-mechanically. Bloch oscillations could only take place according to the scenario of the previous paragraph, if the quantum fluctuations of the environmental charge q are suppressed to the value much below $2e$. Most proposals consider using a resistance R for the decoupling impedance Z . As we hint in the introduction, this will require³ $R \gg R_Q$ for frequencies up to $E_C/h \simeq 10$ GHz. The requirement of high operating frequency and $R \gg R_Q$ is very hard to meet simultaneously, because vacuum, with its $Z_{\text{vac}} = 377 \Omega$ resistance, tends to shunt resistors at microwave frequencies (see Eq. 1.2, 1.3) just in the same way it tends to shunt inductances. The only option for a broad-band $R \gg R_Q$ on-chip resistance would be to reduce its physical dimensions, which unfortunately results in their overheating by the Joule dissipation. The overheating takes place because electron-phonon interaction gets extremely weak in small volume metal films at low temperatures[105]. This brings us directly the “classical challenge”.

The “classical” challenge turns out even more severe than the “quantum” one. Let us assume that the quantum fluctuations of the environmental charge are successfully suppressed by a large value of R so the dynamics of q can be treated classically. Then the Bloch oscillations can simply be described by Kirchoff’s laws, where the junction is treated as a non-linear circuit element with the following current (I)-voltage(V) relations: $V_B(t) = V_0 \cos \pi \int_{-\infty}^t I(t')dt/e$ [106]. The resulting circuit equations are mathematically similar to the Josephson oscillations equations, hence the duality of the Bloch and Josephson oscillations [35].

It is then crystal clear that to observe Bloch oscillations, the classical fluctuations of the environmental charge q must also be much smaller than $2e$. Two effects cause classical motion of q . First, since the circuit is non-linear, the energy provided by the DC source must dissipate somewhere, otherwise the charge q will oscillate with a diverging amplitude. In that case the circuit will probably undergo Landau-Zenner transitions to the junction excited states. Therefore, we believe that the classical motion of q must be overdamped. This fact is often ignored by other authors [107, 108]. Second, the presence of dissipation

³One can employ the following logic to estimate how large should R be. The time it takes for the charge on the black-sheep junction to equilibrate with the capacitance C_s through the resistance R is given by the time RC , while the time associated with the charge dynamics in the small junction is given by h/E_C . The decoupling of the small junction from C_s will thus take place if $RC \gg h/E_C$, which is equivalent to $R \gg R_Q$.

couples the circuit variable q to a heat bath (the setup is at a finite temperature), which therefore generates the diffusion of the value of q in time. The maximum value δq of the equilibrium thermal fluctuation of q can be estimated from the equipartition theorem, $\delta q^2/2C_s = k_B T/2$, so $\delta q/2e = \sqrt{k_B T/E_{C_s}}$. Even at the dilution refrigerator temperatures $\delta q/2e \gg 1$. Therefore, the spectrum of Bloch oscillation signal will acquire a finite linewidth Γ_B . It is given by the inverse time $1/\Gamma_B$ it takes for the value of $q/2e$ to diffuse from 0 to 1.

The diffusion of q can be estimated by assuming that the motion is overdamped and averaging to zero the voltage drop across the junction. Then, using the fluctuation-dissipation theorem, the theory of Nyquist-Johnson noise in resistors, and simple dimensional analysis, we find that the diffusion constant D_q for the coordinate q is given by $D_q \approx k_B T/R$, so that $\delta q(t) = (D_q t)^{1/2}$. The linewidth Γ_B of Bloch oscillations is then given by $\delta q(1/\Gamma_B) = 2e$, so that

$$\Gamma_B \approx k_B T/R(2e)^2 = k_B T[\text{Hz}] \times R_Q/R \quad (5.3)$$

The conclusion for formula (5.3) is in fact more disappointing than it appears. Of course, the larger the bias resistance R and the lower its electron temperature T , the narrower the Bloch oscillation resonance. However, we should not forget that the resistance R must be made physically very small, to satisfy the “quantum” requirement that $R > R_Q$ at frequencies up to 10 GHz. In that situation, the Joule power $I^2 R$ dissipating in this resistor has few options to escape the resistor, and therefore the electron temperature rises with the current. In a simple hot-electron picture, where the heat is drained from the ends of the resistor, the equilibrium temperature T^* of the resistor scales approximately as $k_B T^* = eIR$. Replacing T with T^* in the Eq. (5.3) we come to a catastrophic conclusion: $\Gamma_B \approx I/2e = f$, i. e. the Bloch linewidth is of the same order of magnitude as the Bloch oscillation frequency! We thus conclude that suppressing both quantum and classical fluctuations of the environmental charge q with an on-chip resistance require incompatible types of resistors, and the problem can be traced back again to the small value of the fine-structure constant.

It is worth making the following important remark. Although Bloch and Josephson

oscillations are dual in nature, in practice they are very different because of the way parasitic circuit elements affect the phenomena. In the case of Bloch oscillations, the parasitic element is the capacitance of the DC leads C_s , it generates equilibrium fluctuations of the environmental charge q with a magnitude $\delta q = \sqrt{k_B T C_s}$, such that $\delta q \gg 2e$. Therefore, Bloch oscillations are classically unstable in the absence of cold damping. On the contrary, in the Josephson effect circuit, the parasitic element is the inductance of the voltage source leads L_s , which could never exceed a nH, so the equilibrium fluctuation of phase $\delta\varphi$ across the junction, given by $\delta\varphi = \sqrt{k_B T L_s} / \Phi_0$ is such that $\delta\varphi \ll 2\pi$, so the Josephson oscillations are generically stable and do not require overdamping.

5.4.2 Dispersive Bloch oscillations

Addressing the issues of the orthodox Bloch oscillations, we propose below a fully dispersive version of this phenomenon. Let us replace the resistance R with an inductance L to get rid of Joule heating. Inductance L will still do a fine job suppressing quantum fluctuations of q , provided that $\sqrt{L/C_J} \gg R_Q$ (see Eq. 1.1). In other words, we replace resistance $R \gg R_Q$ with a superinductance. Estimation of the exact value of L , required to treat the environmental charge q as a classical variable goes beyond the scope of the present work. There probably will be corrections to the semi-classical picture, due to a finite small size of quantum fluctuations of q ; the quantity $R_Q / \sqrt{L/C_J}$ will probably play the role of a small parameter of some perturbation theory. To our knowledge such theory has not been worked out yet (see our first attempt in Ref. [45]). However, we shall still proceed treating the environmental charge q classically to address the more important issue of the stabilization of the classical motion.

The oscillations are read out in a dispersive manner with a microwave resonator, in the same manner we read the state of fluxonium (Fig. 5-7). We no longer care for the Bloch voltage across the junction (V_B is nearly zero), instead we measure the frequency shift χ_g of the readout resonator, by the ground state g of the Bloch circuit. This shift involves the detuning of the resonator frequency ν_0 from the junction ground g to first excited state e transition frequency ν_{ge} , and is given by Eq. (3.17). Since the frequency ν_{eg} is sensitive to the total offset charge $q + It$ flowing into the junction, the dispersive shift $\chi_g = \chi_g(q)$

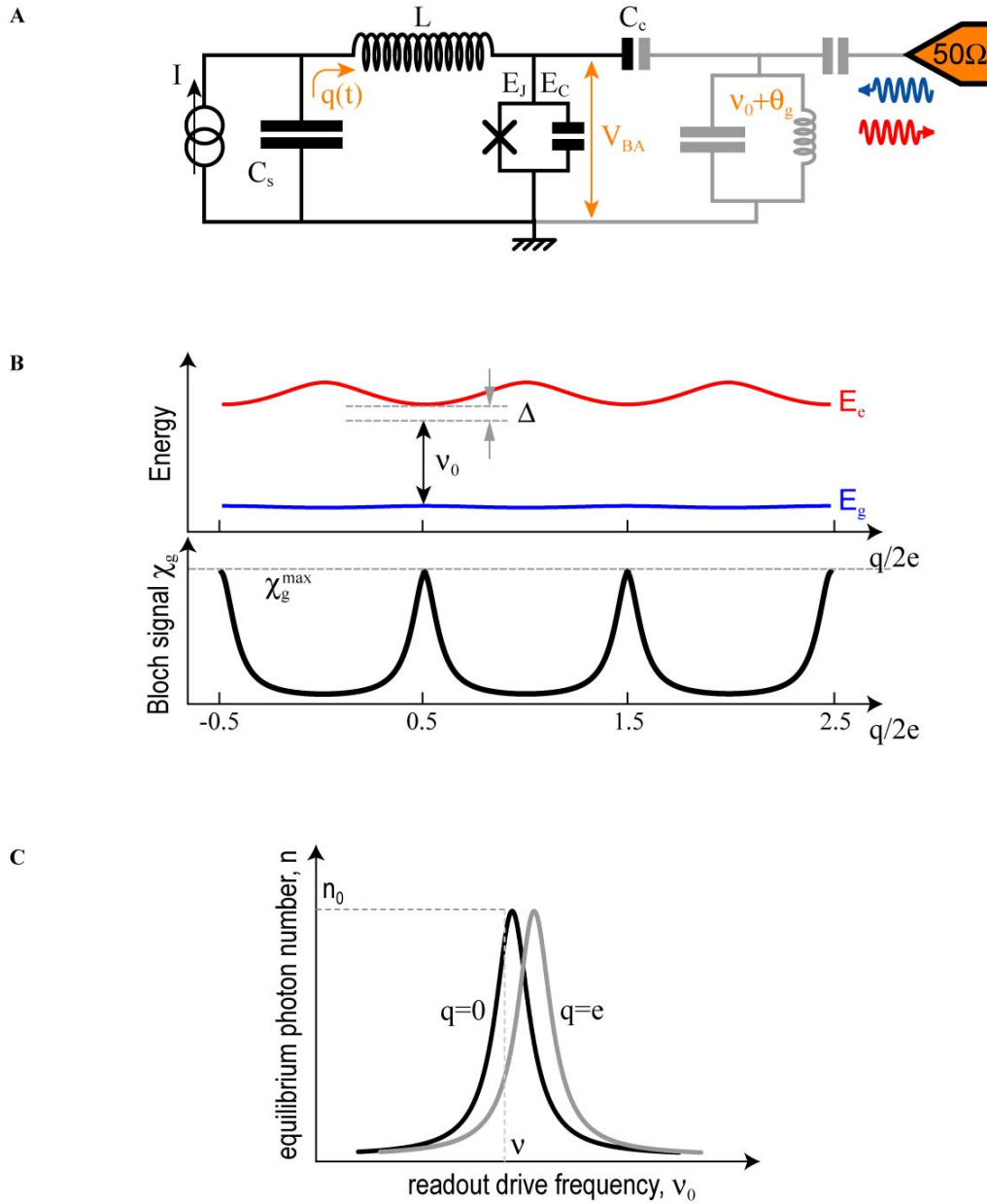


Figure 5-7: Dispersive Bloch oscillations. (A) Setup for detecting dispersive Bloch oscillations. Assuming that the charge $q + It$ flowing through the inductance L is a classical variable, the junction is expected to shift dispersively the resonance frequency of the readout resonator (in grey). (B-top) Energy levels of the junction, the ground (blue) and the first excited (red). The ground state is chosen with a vanishing charge dispersion, in sharp contrast to the orthodox Bloch oscillations. (B-bottom) Modulation of the dispersive shift by the circuit ground state for a resonator frequency choice indicated. (C) Stationary population of photons in the readout resonator. Driving the resonator on the positive slope of the lorentzian result in damping of the environmental charge q .

depends on q . Moreover, in the case of suppressed classical fluctuations of q , the dispersive shift χ_g is a periodic function of time, $\chi_g(t) = \chi_g(t + 2e/I)$, with the period given by the Bloch frequency $f_B = I/2e$.

Now let us describe the two extremely advantageous properties of our Bloch oscillating circuit. First, let us choose parameter $E_J/E_C \in [5, 10]$, such that the ground state charge dispersion is small (compared to, say, temperature $k_B T$) while the first excited state has still a considerable (over 1 GHz) dispersion [73]. At first, this choice of parameters does not seem right: the junction does not generate any Bloch oscillating voltage in its ground state. However, the uniform motion of charge through the junction does generate a periodic frequency shift χ_g of the readout resonator, with the correct period! Importantly, when the readout resonator is empty of photons, the junction appears as a short circuit to the charge q , so the Bloch oscillating circuit appears to be entirely linear to the charge q . This remarkable circumstance solves the problem of energy pumping from the DC source to the oscillations of q , so the motion of q is much more stable, and no longer needs to be overdamped.

The second key property of our Bloch oscillating circuit is that the back-action of the dispersive readout causes dissipation to the variable q , by a mechanism analogous to the Sysiphus cooling of atoms[109]. Indeed, let us populate the readout resonator with the average photon number n by driving it close to the resonance frequency ν_0 . Now resonator acts back onto the small junction and causes an AC-Stark shift of its ground state by an amount $\delta E_g = n \times h\chi_g(q + It)$, resulting in a small-amplitude oscillating voltage across the junction $V_{BA} = n \times h\partial\chi_g(q)/\partial q$ ⁴. The dissipation to q comes from the fact that n depends on the detuning from the resonance, and hence on χ_g . More precisely, the dissipation comes from the fact that n cannot respond instantaneously to a sharp detuning from the resonance [110, 111, ?]. The typical lag time of the resonator is given by its inverse linewidth $\tau = 1/\Gamma_R$. Mathematically, we can describe the effect of lagging readout by writing (let us switch off the DC source for a moment)

$$V_{BA}(q) = n(q(t - \tau)) \times h\partial\chi_g(q(t))/\partial q(t)] \quad (5.4)$$

⁴The subscript “BA” in V_{BA} stands for “Back-Action” voltage.

Assuming that the change of q in time by $2e$ is slower than the readout recovery, we can approximate $q(t - \tau) = q(t) - \dot{q}(t)/\Gamma_R$, and find that $V_{BA} = n(q) \times h\partial\chi_g(q)/\partial q + V_{BA}^R(q, \dot{q})$, where

$$V_{BA}^R(q) = -h\partial n/\partial\chi_g(\partial\chi_g/\partial q)^2\Gamma_R^{-1} \times \dot{q} \quad (5.5)$$

Circuit analogy immediately suggests that the voltage V_B^R corresponds to a voltage drop across a resistance, with a time-dependent value given by the prefactor in front of \dot{q} in the formula (5.5). Let us evaluate this resistance.

Given that $n = n_0 \frac{\Gamma_R^2}{(\nu_0 + \chi_g - \nu)^2 + \Gamma_R^2}$ takes the standard lorentzian shape, with n_0 being the population of the cavity on resonance, we write $\partial n/\partial\chi_g = -\partial n/\partial\nu$. This quantity takes the maximum absolute value for $|\nu_0 + \chi_g - \nu| \simeq \Gamma_R$, which defines the optimum driving frequency ν , so we can estimate $\partial n/\partial\chi_g \simeq -n_0/\Gamma_R$ for a red detuned drive and $\partial n/\partial\chi_g \simeq +n_0/\Gamma_R$ for a blue-detuned drive. Next factor, $(\partial\chi_g/\partial q)^2$ oscillates with q , but remains positive. Its average (over the Bloch period) value can be estimated as $\overline{(\partial\chi_g/\partial q)^2} = (\chi_g^{\max}/2e)^2$. Here, the quantity χ_g^{\max} is the maximum dispersive shift of the readout resonator by the ground state of the junction. The dispersive shift takes its maximum value, $\chi_q = \chi_g^{\max}$, for q being either even or odd number of e , so that the quantity $\Delta = |\nu_0 - \nu_{eg}(q)|$ is minimized. Summing up, we estimate the average electrical resistance R_B felt by the environmental charge q due to the back-action of the readout circuit:

$$R_B \approx R_Q \left(\frac{\chi_g^{\max}}{\Gamma_R} \right)^2 n_0 \quad (5.6)$$

Note that the actual energy is transferred from the variable q to the resonator, and then emitted into the well-thermalized to $T = 15$ mK off-chip resistance of 50Ω lines. Note also that when charge q changes by $2e$ faster than the time Γ_R^{-1} , our formalism breaks down. Therefore, our active resistance is effective only for frequencies up to Γ_R .

Speculating about the numbers, we can think of making $\Gamma_R \approx \chi_g^{\max} \approx 50 - 100$ MHz and increase n_0 to the maximum possible value, before we see any spurious effects. Dispersive readout of the transmon qubits works well for n_0 as large as 30 [91], so there is hope that the quantity R_B/R_Q could take the value of at least that much, resulting in the conservative estimate for the quality factor of the resonance in the Bloch signal spectrum to be at

least 10. In case the shape of this resonance agrees well with the detailed theory of this phenomenon, one could think of quantum metrology of electrical current. The choice of $\Gamma_R \approx 50 - 100$ MHz limits the detectable Bloch oscillating signal to the same frequencies and will result in the currents of $I = 2e \times 50 \text{ MHz} = 150 \text{ pA}$, which is too small for the present standards on quantum metrology. However, nothing prevents us from multiplexing the Bloch oscillating circuits to a number of 10, which would result in the current of 1.5 nA, sufficient for experiments on the closure of the metrology triangle⁵.

⁵Competing idea is to use single electron pumps[112] or hybrid turnstiles[113]. Those island-based devices, while promising for metrology, are hard to parallelize due to the inevitable presence of random offset charges on the islands.

Readout resonator strips width (measured)	15 μm
Readout resonator strips separation (measured)	4 μm
Readout resonator wave impedance Z_∞ (inferred)	80 Ω
Readout resonator resonance frequency ν_0 (fit)	8.175 GHz
Readout resonator external quality factor Q_{ext} (measured)	400
Readout resonator internal quality factor Q_{int} (measured)	2000 – 5000
Black-sheep junction dimensions (nominal)	0.35 μm \times 0.2 μm
Array junction dimensions (nominal)	2 μm \times 0.2 μm
Array inductive energy $E_L = (\hbar/2e)^2/L$ (fit)	0.525 GHz
Array inductance L (inferred)	300 nH
Black-sheep junction Josephson energy E_J (fit)	8.9 GHz
Black-sheep junction Coulomb energy $E_C = e^2/2C_J$ (fit)	2.5 GHz
Number of array junctions N (nominal)	43
Array junction Josephson energy $E_{j \neq 0} = NE_L$ (inferred)	22.5 GHz
Array junction Coulomb energy $E_{C_{j \neq 0}}$ (inferred)	0.85 – 1 GHz
Qubit-cavity coupling constant g (fit)	181 MHz
Qubit-cavity coupling capacitance C_c (inferred from g and Z_∞)	0.8 fF
Black-sheep junction PS energy $ E_{SB} $ (measured, inferred)	369 MHz
Array junction PS energy E_{SA} (inferred from $L, E_{J_{j \neq 0}}, E_{C_{j \neq 0}}$)	50 – 250 kHz
Array junction PS energy E_{SA} (inferred from $T_{2\text{RAMSEY}}(\varphi_{\text{ext}} = \pi)$)	130 kHz

Table 5.2: Device parameters

Bibliography

- [1] M. H. Devoret, *Les Houches, Session LXIII* (1995).
- [2] B. I. Halperin, G. Refael, E. Demler, *Resistance in Superconductors* (World Scientific, 2010).
- [3] V. E. Manucharyan, J. Koch, L. I. Glazman, M. H. Devoret, *Science* **326**, 113 (2009).
- [4] D. V. Averin, A. B. Zorin, K. K. Likharev, *Sov. Phys.-JETP (Engl. Transl.);(United States)* **61** (1985).
- [5] L. S. Kuzmin, D. B. Haviland, *Physical Review Letters* **67**, 2890 (1991).
- [6] M. Watanabe, D. B. Haviland, *Physical Review Letters* **86**, 5120 (2001).
- [7] F. Nguyen, *et al.*, *Physical Review Letters* **99**, 187005 (2007).
- [8] S. Gladchenko, *et al.*, *Nature Physics* **5**, 48 (2008).
- [9] D. B. Haviland, K. Andersson, P. Agren, *Journal of Low Temperature Physics*, **118** **5**, 733 (2000).
- [10] A. J. Leggett, *Prog. Theor. Phys. Suppl* **69**, 80 (1980).
- [11] A. J. Leggett, *Journal of Physics: Condensed Matter* **14**, R415 (2002).
- [12] A. O. Caldeira, A. J. Leggett, *Physical Review Letters* **46**, 211 (1981).
- [13] A. J. Leggett, *et al.*, *Reviews of Modern Physics* **59**, 1 (1987).
- [14] M. H. Devoret, J. M. Martinis, J. Clarke, *Physical Review Letters* **55**, 1908 (1985).

- [15] J. M. Martinis, M. H. Devoret, J. Clarke, *Physical Review Letters* **55**, 1543 (1985).
- [16] V. Bouchiat, D. Vion, P. Joyez, D. Esteve, M. H. Devoret, *Physica Scripta* **1998**, 165 (1998).
- [17] Y. Nakamura, Y. A. Pashkin, J. S. Tsai, *Nature* **398**, 786 (1999).
- [18] D. Vion, *et al.*, *Science* **296**, 886 (2002).
- [19] A. Wallraff, *et al.*, *Nature* **431**, 162 (2004).
- [20] P. Joyez, The single cooper pair transistor: a macroscopic quantum system, Ph.D. thesis, Universite Paris 6 (1995).
- [21] V. Bouchiat, Quantum fluctuations of the charge in single electron and single cooper pair devices, Ph.D. thesis, Universite Paris 6 (1997).
- [22] A. Cottet, Implementation of a quantum bit in a superconducting circuit, Ph.D. thesis, Universite Paris 6 (2002).
- [23] D. I. Schuster, Circuit quantum electrodynamics, Ph.D. thesis, Yale University (2007).
- [24] R. Vijayaraghavan, Josephson bifurcation amplifier: Amplifying quantum signals using a dynamical bifurcation, Ph.D. thesis, Yale University (2008).
- [25] M. Metcalfe, A new microwave readout for superconducting qubits, Ph.D. thesis, Yale University (2008).
- [26] D. M. Pozar, *Microwave engineering* (Wiley-India, 2009).
- [27] J. D. Jackson, *Wiley & Sons Inc., New York* (1962).
- [28] A. J. Annunziata, *et al.*, *Nanotechnology* **21**, 445202 (2010).
- [29] V. V. Shmidt, P. Muller, A. V. Ustinov, *The physics of superconductors: introduction to fundamentals and applications* (Springer Verlag, 1997).
- [30] P. K. Day, H. G. LeDuc, B. A. Mazin, A. Vayonakis, J. Zmuidzinas, *Nature* **425**, 817 (2003).

- [31] A. J. Annunziata, *et al.*, *Applied Superconductivity, IEEE Transactions on* **19**, 327 (2009).
- [32] A. M. Finkel'stein, *Physica B: Condensed Matter* **197**, 636 (1994).
- [33] R. P. Feynman, R. B. Leighton, M. Sands, *The Feynman Lectures on Physics including Feynmans Tips on Physics: The Definitive and Extended Edition* (Addison Wesley, Reading, 2005).
- [34] C. Hutter, K. Stannigel, E. A. Tholén, J. Lidmar, D. Haviland, *Arxiv preprint arXiv:0804.2099* (2008).
- [35] J. E. Mooij, Y. V. Nazarov, *Nature Physics* **2**, 169 (2006).
- [36] D. A. Ivanov, L. B. Ioffe, V. B. Geshkenbein, G. Blatter, *Physical Review B* **65**, 24509 (2001).
- [37] K. A. Matveev, A. I. Larkin, L. I. Glazman, *Physical Review Letters* **89**, 96802 (2002).
- [38] Y. Aharonov, A. Casher, *Physical Review Letters* **53**, 319 (1984).
- [39] L. D. Landau, E. M. Lifshitz, *Quantum mechanics: non-relativistic theory* (Butterworth-Heinemann, 1991).
- [40] V. A. Rubakov, S. S. Wilson, *Classical theory of gauge fields* (Princeton Univ Press, 2002).
- [41] R. P. Feynman, A. R. Hibbs, *Quantum mechanics and path integrals*, vol. 13 (McGraw-Hill New York, 1965).
- [42] W. J. Elion, J. J. Wachtters, L. L. Sohn, J. E. Mooij, *Physical Review Letters* **71**, 2311 (1993).
- [43] M. Sahu, *et al.*, *Nature Physics* **5**, 503 (2009).
- [44] A. A. Clerk, M. H. Devoret, S. M. Girvin, F. Marquardt, R. J. Schoelkopf, *Reviews of Modern Physics* **82**, 1155 (2010).

- [45] J. Koch, V. E. Manucharyan, M. H. Devoret, L. I. Glazman, *Physical Review Letters* **103**, 217004 (2009).
- [46] D. I. Schuster, *et al.*, *Physical Review Letters* **94**, 123602 (2005).
- [47] J. Aumentado, M. W. Keller, J. M. Martinis, M. H. Devoret, *Physical Review Letters* **92**, 66802 (2004).
- [48] F. Yoshihara, K. Harrabi, A. O. Niskanen, Y. Nakamura, J. S. Tsai, *Physical Review Letters* **97**, 167001 (2006).
- [49] I. Chiorescu, Y. Nakamura, C. Harmans, J. E. Mooij, *Science* **299**, 1869 (2003).
- [50] J. M. Martinis, S. Nam, J. Aumentado, C. Urbina, *Physical Review Letters* **89**, 117901 (2002).
- [51] J. A. Schreier, *et al.*, *Physical Review B* **77**, 180502 (2008).
- [52] I. M. Pop, *et al.*, *Nature Physics* **6**, 589 (2010).
- [53] A. Bezryadin, C. N. Lau, M. Tinkham, *Nature* **404**, 971 (2000).
- [54] C. N. Lau, N. Markovic, M. Bockrath, A. Bezryadin, M. Tinkham, *Physical Review Letters* **87**, 217003 (2001).
- [55] R. Vijay, M. H. Devoret, I. Siddiqi, *Review of Scientific Instruments* **80**, 111101 (2009).
- [56] L. Frunzio, A. Wallraff, D. Schuster, J. Majer, R. Schoelkopf, *Applied Superconductivity, IEEE Transactions on* **15**, 860 (2005).
- [57] K. C. Gupta, R. Garg, I. J. Bahl, P. Bhartia, *Microstrip lines and slotlines* (Artech House Norwood, MA, 1996).
- [58] C. T. Rigetti, Quantum gates for superconducting qubits, Ph.D. thesis, Yale University (2009).
- [59] G. J. Dolan, *Applied Physics Letters* **31**, 337 (1977).

- [60] B. A. Mazin, Microwave kinetic inductance detectors, Ph.D. thesis, California institute of technology (2005).
- [61] M. Morgan, S. Weinreb, *Microwave Symposium Digest, 2002 IEEE MTT-S International* **2**, 817 (2002).
- [62] A. A. Houck, *et al.*, *Physical Review Letters* **101**, 80502 (2008).
- [63] F. Mallet, *et al.*, *Nature Physics* **5**, 791 (2009).
- [64] A. Barone, G. Paterno, *Physics and Applications of the Josephson Effect*. (John Wiley & Sons inc., New York, 1982).
- [65] J. R. Friedman, V. Patel, W. Chen, S. K. Tolpygo, J. E. Lukens, *Nature* **406**, 43 (2000).
- [66] J. M. Raimond, M. Brune, S. Haroche, *Reviews of Modern Physics* **73**, 565 (2001).
- [67] M. H. Devoret, S. M. Girvin, R. J. Schoelkopf, *Annalen der Physik* **16**, 767 (2007).
- [68] A. Blais, R. S. Huang, A. Wallraff, S. M. Girvin, R. J. Schoelkopf, *Physical Review A* **69**, 062320 (2004).
- [69] L. S. Bishop, Circuit quantum electrodynamics 2, Ph.D. thesis, Yale University (2010).
- [70] E. M. Purcell, *Physical Review* **69**, 681 (1946).
- [71] I. Chiorescu, *et al.*, *Nature* **431**, 159 (2004).
- [72] A. Wallraff, *et al.*, *Physical Review Letters* **99**, 50501 (2007).
- [73] J. Koch, *et al.*, *Physical Review A* **76**, 042319 (2007).
- [74] G. Ithier, *et al.*, *Physical Review B* **72**, 134519 (2005).
- [75] D. J. Van Harlingen, *et al.*, *Physical Review B* **70**, 064517 (2004).
- [76] A. Hriscu, Y. Nazarov, *Physical Review Letters* **106**, 77004 (2011).
- [77] N. F. Ramsey, *Science* **248**, 1612 (1990).

- [78] L. S. Bishop, *et al.*, *Nature Physics* **5**, 105 (2008).
- [79] A. Abraham, *The principles of nuclear magnetism* (The Clarendon Press, Oxford, 1961).
- [80] L. Faoro, L. B. Ioffe, *Physical Review Letters* **96**, 47001 (2006).
- [81] W. Happer, *Reviews of Modern Physics* **44**, 169 (1972).
- [82] S. O. Valenzuela, *et al.*, *Science* **314**, 1589 (2006).
- [83] M. Fleischhauer, A. Imamoglu, J. P. Marangos, *Reviews of Modern Physics* **77**, 633 (2005).
- [84] M. Boissonneault, J. M. Gambetta, A. Blais, *Physical Review A* **79**, 013819 (2009).
- [85] H. Paik, *et al.*, *Arxiv preprint arXiv:1105.4652* (2011).
- [86] V. E. Manucharyan, *et al.*, *Arxiv preprint arXiv:1012.1928* (2010).
- [87] R. Fazio, H. Van Der Zant, *Physics Reports* **355**, 235 (2001).
- [88] L. B. Ioffe, M. V. Feigelman, *Physical Review B* **66**, 224503 (2002).
- [89] L. B. Ioffe, V. B. Geshkenbein, M. V. Feigel'Man, A. L. Fauchere, G. Blatter, *Nature* **398**, 679 (1999).
- [90] H. Haffner, C. F. Roos, R. Blatt, *Physics Reports* **469**, 155 (2008).
- [91] R. Vijay, D. H. Slichter, I. Siddiqi, *Physical Review Letters* **106**, 110502 (2011).
- [92] J. Majer, *et al.*, *Nature* **449**, 443 (2007).
- [93] M. A. Sillanpaa, J. I. Park, R. W. Simmonds, *Nature* **449**, 438 (2007).
- [94] L. DiCarlo, *et al.*, *Nature* **460**, 240 (2009).
- [95] M. Wallquist, J. Lantz, V. S. Shumeiko, G. Wendin, *New Journal of Physics* **7**, 178 (2005).
- [96] J. I. Cirac, P. Zoller, *Physical Review Letters* **74**, 4091 (1995).

- [97] T. Udem, R. Holzwarth, T. W. Hansch, *Nature* **416**, 233 (2002).
- [98] S. P. Benz, C. A. Hamilton, *Applied Physics Letters* **68**, 3171 (1996).
- [99] R. E. Prange, S. M. Girvin, P. Lee, *Physics Today* **40**, 93 (1987).
- [100] A. Tzalenchuk, *et al.*, *Nature Nanotechnology* **5**, 186 (2010).
- [101] F. Piquemal, *et al.*, *Comptes Rendus Physique* **5**, 857 (2004).
- [102] P. Cladé, *et al.*, *Physical Review Letters* **96**, 33001 (2006).
- [103] L. Kuzmin, Y. Pashkin, A. Zorin, T. Claeson, *Physica B: Condensed Matter* **203**, 376 (1994).
- [104] M. Watanabe, D. B. Haviland, *Physical Review B* **67**, 094505 (2003).
- [105] B. Huard, H. Pothier, D. Esteve, K. E. Nagaev, *Physical Review B* **76**, 165426 (2007).
- [106] G. Schon, A. D. Zaikin, *Physics Reports* **198**, 237 (1990).
- [107] B. Douçot, L. B. Ioffe, *Physical Review B* **76**, 214507 (2007).
- [108] W. Guichard, F. W. J. Hekking, *Physical Review B* **81**, 064508 (2010).
- [109] C. Cohen-Tannoudji, *Physica Scripta* **1998**, 33 (1998).
- [110] P. Horak, G. Hechenblaikner, K. Gheri, H. Stecher, H. Ritsch, *Physical Review Letters* **79**, 4974 (1997).
- [111] A. A. Clerk, *Physical Review B* **70**, 245306 (2004).
- [112] H. Pothier, P. Lafarge, C. Urbina, D. Esteve, M. H. Devoret, *Europhysics Letters* **17**, 249 (1992).
- [113] J. Pekola, *et al.*, *Nature Physics* **4**, 120 (2007).